Partial and Total Oxidation of Methane in Monolithic Catalysts at Short Contact Times

INAUGURAL - DISSERTATION

zur
Erlangung der Doktorwürde

der
Naturwissenschaftlichen-Mathematischen
Gesamtfakultät

der
Ruprecht-Karls-Universität
Heidelberg

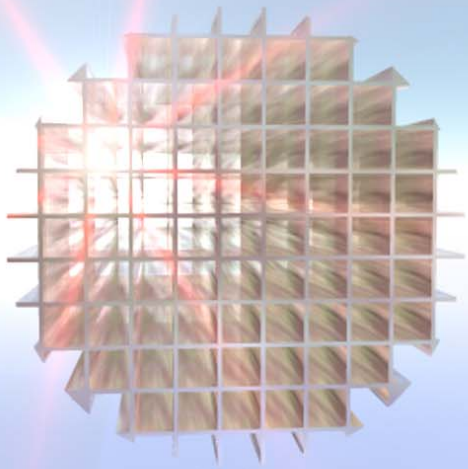

vorgelegt von
Dipl.-Chem. Renate Schwiedernoch
aus Mannheim

Tag der mündlichen Prüfung:
15.07.2005

Partial and Total Oxidation of Methane in Monolithic Catalysts at Short Contact Times

Gutachter:

Prof. Dr. Olaf Deutschmann

Prof. Dr. Jürgen Wolfrum

Meinen Eltern

Ὁ ἀνέξέταστος βίος οὐ βιωιὸς ἀνθρώπῳ

Das unerforschte Leben ist für einen Menschen nicht lebenswert.
(The unexamined life is not worth living).
(Platon, Apologie des Sokrates, 38a) Johannes Burnet

Zusammenfassung

Erdgas, dessen Hauptbestandteil Methan (CH_4) ist, wird neben der Verwendung als Energieträger durch Verbrennung auch zunehmend als Rohstoff für chemische Grundstoffe eingesetzt. Gerade in letzter Zeit ist das Interesse an der Entwicklung günstiger Technologien zur Herstellung von flüssigen Kohlenwasserstoffen (Fischer-Tropsch-Synthese) oder Synthesegas (CO und H_2) durch partielle katalytische Oxidation von CH_4 gestiegen. Allerdings sind die im Einzelnen ablaufenden Prozesse sowohl bei der partiellen als auch bei der totalen katalytischen Oxidation von CH_4 noch nicht vollständig geklärt und bergen Gefahren. Dazu gehört auch das unkontrollierte Ablaufen der Reaktion, da es sich um explosive Gemische handelt. Genau so wichtig ist das Verständnis des instationären Reaktorbetriebs, wie z.B. das An- und Abfahren des Prozesses und das Altern des Katalysatormaterials. Einen wesentlichen Fortschritt hinsichtlich der technischen Anwendung dieser Prozesse erwartet man von der Entwicklung detaillierter Reaktionsmechanismen und deren Einbindung in Computerprogrammen zur Simulation des Gesamtverhaltens des Reaktors. Dazu ist es allerdings notwendig, die Reaktionsmechanismen und deren Wechselwirkung mit Transportprozessen durch wohl definierte Experimente, insbesondere bei instationären Vorgängen, zu evaluieren.

Deshalb beschäftigt sich diese Arbeit mit der vollständigen und partiellen Oxidation von Methan (CH_4). Hierbei werden nicht nur unterschiedliche Katalysatoren, die mit Platin, Rhodium und Palladium beschichtet sind, eingesetzt, sondern vor allem ein weiter Bereich von experimentellen Rahmenbedingungen abgedeckt. Allerdings müssen folgende Probleme gelöst werden: Ein Experiment muss entwickelt werden, das leicht für die Modellierung und numerische Simulationen zugänglich ist. Dabei ist es besonders wichtig, dass das analytische System die Untersuchung von instationärem Reaktorbetrieb wie der Zündung zulässt. Mit den experimentell ermittelten Umsätzen und Selektivitäten sollen die in der Literatur vorhandenen Oberflächenreaktionsmechanismen evaluiert und im Bedarfsfall weiterentwickelt werden. Dabei werden Computerprogramme eingesetzt, um die Vorgänge im Reaktor zu berechnen und mit den experimentellen Beobachtungen zu vergleichen. Ebenso sollen kritische Bedingungen gefunden werden, bei denen die Modelle noch versagen und Vorschläge gemacht werden, diese zu verbessern.

Ein Strömungsreaktor mit möglichst einfacher geometrischer Struktur und entsprechender Analytik wurde konstruiert, der diesen Anforderungen genügt. Das Kernstück ist ein 40 cm langes Quartzrohr mit unterschiedlichen Durchmessern, das einen mit Rh, Pt oder Pd beschichteten wabenförmigen Monolithen beinhaltet. Die Temperaturmessung erfolgt mittels Thermoelementen direkt hinter dem katalytischen Monolithen und außen an der Oberfläche des Reaktors. Zur Zündung des bei Normaldruck strömenden Gasgemisches wird ein Ofen benutzt, der bei autothermen Betrieb nach der Zündung abgeschaltet werden kann. Die Gase werden in einer Kammer vorgemischt und die Produktzusammensetzung mittels Quadrupolmassenspektrometrie (QMS) analysiert. Mit einer Zeitauflösung von etwa 5 s erlaubt dieser Aufbau die Untersuchung instationärer Probleme.

Um die Reaktionsmechanismen zu evaluieren, wurden detaillierte numerische Simulationen der im Reaktor ablaufenden physikalischen und chemischen Prozesse mit dem kürzlich entwickelten Computercode DETCHEM und dem kommerziell erhältlichen CFD-Programm FLUENT simuliert. Dabei werden nicht nur die detaillierten Gasphasen- und Oberflächen-Reaktionsmechanismen berücksichtigt, sondern auch der Massen- und Wärmetransport in den Kanälen. Die Berücksichtigung der Wärmebilanz im Feststoff ermöglicht eine

Simulation instationärer Reaktorvorgänge. Die Katalysatorkanäle werden dabei unter stationären Bedingungen entweder dreidimensional (3D) mittels eines elliptischen Ansatzes mit FLUENT oder im zweidimensionalen (2D) Fall mit einer parabolischen Näherung mit DETCHEM^{MONOLITH} simuliert.

Zuerst wird das Zündverhalten der katalytischen Verbrennung von CH_4 an einem mit Pt beschichteten Monolithen untersucht. Im Experiment werden 1 Vol.-% bis 4 Vol.-% CH_4 zu einem Gemisch aus 20 Vol.-% O_2 und 80 Vol.-% Ar zugesetzt und die Reaktion mit Hilfe eines Ofens gezündet. Die Umsätze von CH_4 und O_2 sowie die Selektivitäten der Bildung von H_2 und CO werden experimentell bestimmt und numerisch simuliert. Es ist zum ersten Mal gelungen, durch Kopplung der Prozesse in den einzelnen Kanälen und dem Wärmetransport in der festen Phase des Monolithen, das Gesamtverhalten des katalytischen Reaktors zu modellieren und durch Experimente zu evaluieren. Ebenfalls neu ist die detaillierte Betrachtung des instationären Vorgangs der katalytischen Zündung im Monolith. Hier ist es gelungen, diese sowohl experimentell zu erfassen, als auch mit sehr guter Übereinstimmung zu simulieren. Lediglich beim Auftreten von Flammen im Reaktor ist eine Berechnung des Reaktorverhaltens noch nicht möglich. Anschließend wird der Einfluss von Wasserstoff auf die Zündung untersucht. Hierzu wurden Experimente durchgeführt, bei denen die für das Erreichen der Zündtemperatur benötigte Energie durch Oxidation von H_2 bereitgestellt wird. Es zeigt sich, dass durch die Zugabe von H_2 nicht nur die notwendige Wärme für die Zündung bereitgestellt wird, sondern zusätzliche chemische Vorgänge die Zündtemperatur erniedrigen. Der verwendete Reaktionsmechanismus ist zwar in der Lage, den kinetischen Einfluss durch die H_2–Zugabe aufzuzeigen, er muss allerdings noch weiter entwickelt werden, um die experimentell ermittelten Umsätze wiedergeben zu können. Bei diesen hohen Temperaturen treten oberhalb einer kritischen Temperatur oszillierende homogene Reaktionen in der Gasphase auf, die noch nicht verstanden sind. Um die Studie der Oxidation von CH_4 bei hohem Sauerstoff-Überschuss abzuschließen, wurden nach der Betrachtung stationärer, instationärer Vorgänge und Wechselwirkungen von heterogenen mit homogenen Phänomenen auch Oszillationen untersucht, die auf Oberflächenrekonstruktionen des Palladiumkatalysators beruhen. Ein in internationaler Kooperation generierter, in Entwicklung befindender, detaillierter Reaktionsmechanismus vermag bereits die oszillierenden Umsätze gut widerzuspiegeln, allerdings ist die dabei auftretende Oszillationsfrequenz noch zu hoch.

Der zweite Teil der experimentellen Studie beschäftigt sich mit der katalytischen Partialoxidation (CPO) von CH_4 auf Rh beschichteten Monolithen. Es zeigt sich, dass nicht nur, wie erwartet, die vollständige Oxidation von CH_4 zu CO_2 und Wasser mit der partiellen Oxidation zu CO und H_2 konkurriert, sondern auch die Wasserdampf-Reformierung einen wesentlichen Beitrag zur H_2-Bildung im Katalysator leistet. Nach jahrelanger Diskussion des Reaktionsablaufs in der Fachliteratur trägt diese Arbeit einen entscheidenden Beitrag zum Verständnis dieser technisch hochinteressanten Prozesse bei. Das Verhältnis CH_4/O_2 wurde zwischen 1.4 und 2.4 bei 75 Vol.-% Ar-Verdünnung unter Verwendung eines mit Rh beladenen Katalysators variiert. Mit Hilfe der gemessenen Daten wird ein detaillierter Reaktionsmechanismus durch Hinzufügen von oberflächenabhängigen Aktivierungsenergien einiger Spezies weiterentwickelt und im stationären Zustand evaluiert. Danach wurde der Einfluss des Trägermaterials, hier α-Aluminiumoxid (Korund) und Cordierit, auf das Zündverhalten experimentell und numerisch untersucht. Die Modelle sind in der Lage, das unterschiedliche Zündverhalten von Cordierit (Zündung am Katalysatoreintritt) und Korund (Zündung am Katalysatoraustritt), widerzuspiegeln. Die Modelle werden anschließend für

Katalysatorentwicklung verwendet. Dazu wird das Zündverhalten virtueller Katalysatoren mit verschiedenen physikalischen Eigenschaften simuliert und verglichen. Der letzte Abschnitt beschäftigt sich mit einem Vergleich konventionell hergestellter Katalysatoren mit *Rh-Nanopulver* beschichteten. Letztere zeigen keine Verbesserung der katalytischen Aktivität unter den hier verwendeten Bedingungen.

Zum Abschluss dieser Arbeit wird die CPO von CH_4 in einem geraden, 37 mm langen Pt-Röhrchen mit einem Durchmesser von 1 mm durchgeführt. Dieses Röhrchen zeichnet sich durch ein noch besser beschreibbares Strömungsfeld aus. Bei Raumtemperatur werden bei einer Verdünnung mit 75 Vol.-% Ar im Mischungsverhältnis von 1.4 bis 3.0 CH_4 und O_2 durchgeleitet. Wenn das CH_4/O_2 Verhältnis einen Wert von 1.9 übersteigt, treten komplexe Oszillationen der Umsätze und Selektivitäten auf. Um dieses Verhalten, das noch nicht modelliert werden kann, zu verstehen, müssen weitere elementare Prozesse wie Kohlenstoffabscheidung bzw. Kohlenstoffoxidation bei der der katalytischen Partialoxidation von CH_4 auf Pt dem detaillierten Mechanismus zugefügt werden.

Abstract:

The readily available feedstocks of natural gas exceed the resources of crude oil by far. Therefore, there is an increasing strong interest in the utilisation of natural gas with its main component methane for the production of more useful chemicals. This leads to a strong demand for compact and low-capital-cost reactors for the conversion of natural gas to methanol and liquid hydrocarbons and the production of hydrogen. The combustion of natural gas is also considered for power generation in catalytic devices, because the flameless catalytic process results in lower emissions of nitrogen oxides. Noble metals such as platinum, palladium, and rhodium are seen as very active catalysts for the conversion of methane. However, the processes occurring during the partial and complete oxidation of CH_4 on these noble metal catalysts are not completely understood. A detailed understanding of the reactor behaviour at all possible conditions is crucial for the technical realization of these catalytic processes, because explosive mixtures are handled. For safety reasons, it is in particular necessary to control the operation of the reactors at transient conditions such as light-off and shut-down. In this respect, potential hazards due to homogeneous ignition and aging of the catalysts also need to be controlled.

The objective of this work is to study total and partial oxidation of methane over platinum, palladium, and rhodium catalysts for a wide range of operating conditions. Therefore, the following problems have to be solved: An experimental set-up, which is easily applicable for modelling and numerical simulation, has to be developed. The experiment and analysis has to be arranged in a way that allows studies of transient processes such as light-off. Based on the experimentally derived conversion and selectivity surface-reaction schemes, available in literature, have to be evaluated. Therefore, computational tools available have to be used to numerically predicted reactor performance and compare these results with the experimental data. Crucial conditions, at which the reaction models need improvement, have to be found, and if necessary and possible improved.

A flow reactor with associated analysis is designed to meet these requirements. In order to facilitate the simulation of the system catalysts exhibiting a simple geometry such as monolithic structures are used. The reactor consists of a 40 cm long quartz tube with varying inner diameters. Honeycomb catalysts coated with Rh, Pd, or Pt are placed inside. The gas temperature at the exit of the catalytic monolith and outside the quartz tube is monitored using thermocouples. The reaction is ignited by heating up the reactor by a furnace, in which the flow system is integrated. After ignition, in the case of autothermal operation, the furnace can be switched off and used for thermal insulation of the flow reactor. The gases are premixed at room temperature and flow into the quartz tube at atmospheric pressure. The product composition is quantitatively analysed by a quadrupole mass spectrometer (QMS) in order to study transient phenomena. The time resolution of the QMS is approximately 5 s.

For the evaluation of reaction mechanisms, detailed numerical simulations of the physical and chemical processes using the recently developed computer program package DETCHEM and the commercially available CFD code FLUENT are applied. The numerical codes take into account detailed mechanisms of surface and gas phase reactions as well as mass and heat transport processes in the channels and heat transport in the solid monolithic structure. The channels are simulated under steady-state conditions in three-dimensions by an elliptic approach using FLUENT and in two dimensions by a parabolic approach using $DETCHEM^{CHANNEL}$. Transient phenomena are simulated by $DETCHEM^{MONOLITH}$, which

includes transient heat balances of the monolithic structure and two-dimensional, parabolic flow field simulations of a representative number of single channels.

First, the ignition of catalytic combustion of CH_4 on a Pt loaded monolith is investigated. Mixtures of 20 vol.-% O_2 and 80 vol.-% Ar are flown through the reactor and 1 vol.-% to 4 vol.-% CH_4 is added. The reactor is heated by a furnace until ignition occurs and the conversions of CH_4 and O_2 as well as the product selectivities are experimentally determined and the results numerically simulated. Then, the influence of H_2 addition on the combustion is investigated. In these experiments, the ignition temperature is reached by the addition of a certain amount of H_2 to the mixture. Exothermic oxidation of H_2 occurs already at room temperature providing the heat for the reaction. The detailed reaction mechanism for CH_4 combustion on Pt is able to describe the different kinetic behaviours qualitatively well. Oscillating homogeneous gas-phase reactions were experimentally observed in certain high temperature regions. Simulation of flame formation has not been pursued with the parabolic code available. Reaction rate oscillations of the catalytic combustion of methane on a palladium based catalyst are eventually found experimentally at lean conditions in palladium coated monoliths. The oscillations can be understood by surface and bulk oxidation/reduction cycles (Pd $\rightleftharpoons$ PdO). A surface-reaction mechanism based on those cycles is able to describe the oscillation behaviour in general but producing too high frequencies.

The second set of experimental studies is devoted to partial oxidation of CH_4 over Rh coated monolithic structures. In this fuel-rich region, complete oxidation of methane to CO_2 and H_2O, however, still competes with the partial oxidation to CO and H_2. In the study presented, the CH_4/O_2-ratio is varied between 1.4 and 2.4 with a constant argon dilution of 75 vol.-%. The experimentally derived conversion and selectivities are used to improve a detailed reaction mechanism. In particular, the model extension includes coverage dependent activation energies for some species. Next, the influence of the support material on the ignition process is investigated. In the experiment, either α-alumina or cordierite as support material is applied and coated with 3 wt.-% Rh. The models are able to describe the light-off behaviour: The reaction starts from the front for cordierite and from the back for alumina monoliths. Now the reaction mechanism and the transport models are applied for catalyst design: The ignition behaviour of a set of virtual catalytic monoliths exhibiting varying physical properties is modelled. In addition to those wet coated catalysts, finally, a catalysts coated with Rh-nanopowder produced by laser ablation is experimentally examined. The *nanopowder* catalyst does not show any improvement concerning synthesis gas yield.

At the end of this thesis, partial oxidation of methane is carried in a straight platinum tube, which is 1 mm in diameter and 37 mm in length. This catalytic tube represents an even more well-defined configuration for modelling. Room-temperature methane/oxygen mixtures in 75% argon dilution are fed at CH_4/O_2 volumetric ratios between 1.4 and 3.0, and the temperature is increased up to 1375 K. At CH_4/O_2 ratios above 1.9 complex patterns of oscillation in conversion and selectivity occur. The understanding of this reactor behaviour, which cannot be modelled yet, needs to include the carbon deposition and removal on the platinum surface during reaction.

TABLE OF CONTENTS

CHAPTER I

1 Motivation

Even in ancient times, catalysts played an important role. For instance, the Greek and the Romans used biocatalysts for the production of wine and acetic acid as well as to convert sugar into starch. Inorganic catalysts were introduced to the soap production from oils and fat. Nowadays catalysis (Greek: καταλυειν - katalýein: unclamp, dissolve, destroy) has a great impact on all physical, chemical, and biological sciences. As well as catalysis is a mainstay of the chemical industry, it finds a place in laboratory synthesis and is common for all enzymatic processes. It also plays a role in the air pollution control, the research of new technologies for power generation or for formation of basic materials from chemical feedstock like natural gas. More than 90% of all chemical products are in contact with a catalyst during manufacturing processes. A big amount of food, medicinal drugs, materials for construction, and most of the fuels are produced by heterogeneous catalysis.[1]

In the last few years, there is an increasing strong interest in the catalytic partial oxidation, especially of methane, the main component of natural gas.[2-8] This interest is actuated by a strong demand for compact and low-capital-cost reactors for the conversion of natural gas to liquids and the production of hydrogen. A large variety of methods has been studied to identify an efficient route for the direct conversion of CH_4 to higher hydrocarbons.[9-13] However, no process has yet been identified as a better candidate that could potentially replace the formation of synthesis gas (a mixture of H_2 and CO) as a first step on the way from methane to higher hydrocarbons. Thus, CH_4 conversion via synthesis gas is still the route of choice. The production of synthesis gas, or shorter syngas, accounts for about 60% of the costs of the whole conversion process of a gas-to-liquid plant.[14]

Presently, the most important industrial route to syngas is steam reforming of CH_4 performed in large-sized reactors with high demand for energy.

Catalytic partial oxidation (CPO) of CH_4 over noble metals, in particular rhodium, offers a promising alternative. The overall reaction is slightly exothermic:

$$CH_4 + ½\ O_2 \rightleftharpoons CO + 2\ H_2 \qquad \Delta H_R = -36\ kJ\ mol^{-1}\ , \qquad (1.1)$$

Since oxygen is easily available, the highly exothermic total oxidation of CH_4,

$$CH_4 + 2\ O_2 \rightleftharpoons CO_2 + 2\ H_2O \qquad \Delta H_R = -802\ kJ\ mol^{-1}\ , \qquad (1.2)$$

competes with the syngas production route. Syngas is formed as combination of the direct route and steam reforming after complete oxidation of some CH_4. In this study, both pathways are combined.[15] The H_2 over CO ratio of about 2 in the product gas of the partial oxidation route is very favourable for subsequent methanol production or the Fischer-Tropsch process for synthetic liquid fuels.[16]

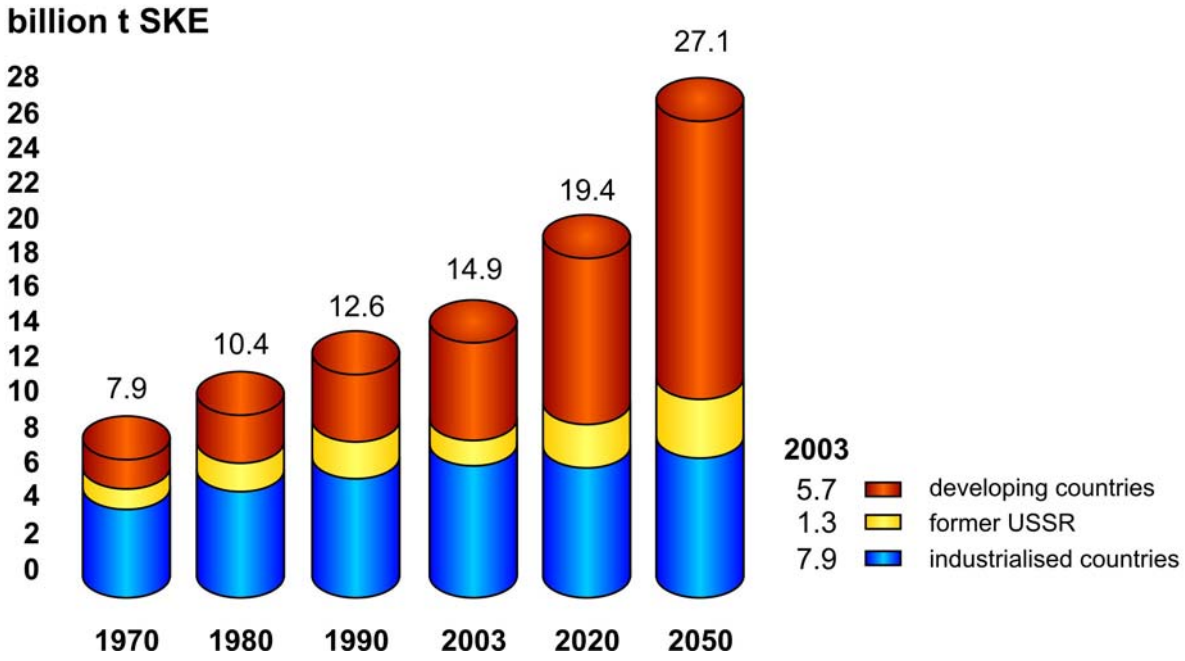

Figure 1.1: Worldwide energy consumption.[17]; 1 t SKE = 8140 kWh

A further driving force for the utilisation of CH_4 is the high demand for H_2. Only an efficient production of hydrogen (from Greek υδωρ = *hydor*, "water" and γενναν = *gennan*, "generate") attracts attention these days. H_2 itself is nature's most abundant element, accounting for more than 90% of the observable universe; it was discovered by Henry Cavendish in 1766.[18] In fact, atomic hydrogen accounts for more than 30% of the mass of the sun. It is present in water and in all organic compounds and living organisms. Large quantities of H_2 are needed industrially, notably in the *Haber process* for the production of

ammonia, the hydrogenation of fats and oils, and the production of methanol. A modern aspect of H_2 use is its application in power generation by fuel cells. Though the fuel cell was already invented by William Robert Grove in 1839, the demand for H_2 as a potential fuel for fuel cells will increase since it provides an environment-friendly and low-emission carrier of energy.[19] Some applications in automobile industry may form a small fraction of the fuel to produce H_2 and CO. This hydrogen is fed to the engine to reduce pollutant during start-up. It can also be used in SOFCs (solid oxide fuel cells) or PEM (proton exchange membrane) fuel cells for power generators used, e.g., for air conditioning.

Not only CPO of CH_4 is of interest in terms of providing precursors as chemical feedstock but also the complete combustion of natural gas for power generation. The worldwide demand for energy has doubled since the 1970's. In 2003 around 14.9 billion t SKE (1 t SKE = 8140 kWh) were consumed worldwide.[17] Although the energy consumption stagnated in the industrialised countries the overall consumption may again double till the year 2050 (Figure 1.1) due to the expected industrial growth in newly industrialising countries. Nowadays the energy requirement is covered to 33% by oil, 22% by natural gas, and 25% by coal, which calls for new and more efficient technologies for power generation.

Ever since the discovery of flameless combustion of flammable fuel-air mixtures on a platinum wire and the consecutive invention of the miners' safety lamp by Davy in 1817 [20] and the construction of the pneumatic gas lighter by Döbereiner in 1823,[21] catalysis and combustion have been linked. Catalytic combustion can be defined as the complete oxidation of a combustible compound on the surface of a catalyst. While conventional combustion occurs in the presence of a flame, catalytic combustion is a flameless process, taking place at lower temperatures and, therefore, resulting in lower emissions of nitrogen oxides. Furthermore, catalytic combustion offers fewer constraints concerning flammability limits and reactor design. These advantages of catalytic combustion determine its potential applications as discussed in [22, 23].

Because of the low NO_x emissions, there is a wide interest in applying catalytic combustion to power generation by gas turbines,[24, 25] despite recent advances in non-catalytic gas turbine technology. Today, natural-gas-fired turbines operated with a catalytic combustion stage are proceeding from laboratory-scale to commercial-scale testing and have shown the ability of reducing the NO_x emission level to 3 ppm. The development of this technology requires an integrated approach, based on advanced combustor design and the development of highly active and stable catalysts. Present combustor configurations are based on multiple-stage combustion, mostly including a homogeneous combustion stage. The design of the catalytic combustion stage typically calls for monolith systems that offer high surface area but low-pressure drop. The monolith honeycombs are predominantly made of cordierite coated with the catalyst material, where the surface area is frequently enlarged by a wash-coat, mostly alumina.[22]

A wide variety of materials has been investigated for catalytic combustion, mainly for catalytic oxidation of CH_4 in the presence of excess O_2. All precious metals, especially platinum and palladium, and numerous oxides have been studied. Most of the studies have been focused on finding proper catalytic materials.[24] However, little is known about the physical and chemical elementary processes occurring on the catalyst, e.g., the complex behaviour of the Pd/PdO catalyst is not really understood yet. Metal substituted hexaluminates have also been extensively investigated due to their thermal stability and good activity for methane oxidation.[22, 26]

Catalytic combustion is also used to burn volatile organic compounds (VOC) present in low concentrations in air streams; e.g., filters using platinum catalyst have been applied for the abatement of VOC.[27] Catalytic radiant burners have found use throughout industry in various applications, such as drying of paints, paper and pulp, and the thermoforming of plastics.[28] Further current applications of catalytic combustion include catalytic igniters, portable heaters, and home heating appliances. Use of biomass-derived fuels, fuel-cell technology, chemical synthesis, and micro-burners and reactors are becoming further driving forces for catalytic-combustion research and development. A more thorough introduction into catalytic combustion was published by Hayes and Kolaczkowski.[22, 28]

A catalyst may also be applied for ignition and stabilisation of homogeneous gaseous combustion via thermal and chemical interactions with the exothermic heterogeneous oxidation reaction.[29] This so-called *catalytically stabilised thermal combustion* has the potential to expand flammability limits and reduce pollutant emissions.

Catalytic combustion research currently focuses on reactor design, increase in efficiency, and the search for more suitable catalysts. Thus, there is an urgent need for a better understanding of the physical and chemical processes occurring on the catalytic surface and their coupling with the surrounding flow field. In particular, it is important to understand the ignition and extinction behaviour of the oxidation of hydrocarbons. During the last decade, detailed catalytic combustion models have been designed [30-33] including multi-step heterogeneous surface-reaction mechanisms possibly providing guidelines for a better understanding and for the optimisation of catalytic combustion. For the optimisation of reactors and safety control (explosive mixtures), not only the understanding of the reaction pathways is necessary but also that of the role of the physical and chemical properties of the catalyst support. Applications reach from gas-to-liquid plants to the on-board production of hydrogen for fuel cells or reformats for the reduction of combustion pollutants in automobiles.

This work focuses on combining experimental results with detailed numerical simulations of the physical and chemical processes using DETCHEM.[34-38] For this purpose, detailed surface and gas-phase reaction mechanisms are used and modified. In chapter 5 the catalytic combustion of CH_4 is investigated in detail. First the transient behaviour is experimentally and numerically examined,[39] followed by a study of the

effect of H_2 addition to the combustion mixture on ignition of the CH_4 oxidation. Moreover, the impact of homogeneous reactions in this system is investigated, as well. Since surface reconstructions as known from temperature self-control by a reversible transformation of PdO to Pd and vice versa can occur,[25, 40] the last part of this chapter focuses on this oscillatory behaviour during CH_4 combustion on Pd coated monoliths. In the scope of this work, not only the lean mixture of CH_4 and oxygen is investigated but also the fuel-rich region, where CPO leads to the formation of H_2. Chapter 6 focuses first on a evaluation and modification of detailed reaction mechanisms for the CPO of CH_4 on monoliths coated with Rh by analyses under steady-state [15] and transient conditions,[41] followed by a study of the impact of different support materials on the reaction pathways.[42] To complete this work a model system is described in Chapter 7. Here the oxidation of CO and the CPO of CH_4 are performed using a single Pt-tube in order to understand the competition between different reaction pathways at high temperatures.

CHAPTER II

2 Kinetic Concepts of Heterogeneous Reactions

Berzelius introduced the term “catalysis” as early as in 1836 in order to explain various decomposition and transformation reactions. He assumed that catalysts possess special powers influencing the affinity of chemical substances. Ostwald (1895) gave a definition that is still valid today: “a catalyst accelerates a chemical reaction without effecting the position of the equilibrium”. This means that the pathway of a reaction is changed to another one exhibiting a lower activation energy compared to the uncatalysed reaction.

In heterogeneous catalysis, the active catalytic surface is of major importance, since at least one of the reactants must be attached to the surface for a significant period of time. Therefore chapter 2.1 focuses on adsorption, desorption and surface diffusion. As soon as the reactants reach the catalyst surface, chemical reactions occur as discussed in section 2.2.

Only a brief overview of the fundamentals of heterogeneous catalysis is summarised in this chapter, detailed descriptions can be found in literature.[1, 43-47]

2.1 Adsorption, Desorption and Diffusion

Adsorption steps that precede and follow the chemical reaction are part of the microkinetics and draw special attention. There are two different kinds of adsorption: physical adsorption (physisorption) and chemical adsorption (chemisorption).

Physisorption is the result of *van der Waals* forces, and the heat of adsorption is comparable to the heat of evaporation of the adsorbate. In chemisorption, chemical bonds are formed between the catalyst and the adsorbed material. The resulting surface molecules are much more reactive than free adsorbate molecules. The heats of chemisorption are comparable to the heat of chemical reactions. Figure 2.1 shows a typical potential diagram of a molecule as a function of the distance to the surface.

Physisorption is fast, and equilibrium is rapidly reached, even at low temperatures. With further approach, chemisorption can occur leading to a lower potential energy. However, chemisorption generally requires high activation energies because of the high energy required to break the chemical bonds. The rate of adsorption is low at low temperatures, but the process can be rapid at high temperatures. The breaking of chemical bonds on the surface and removal of molecules from the surface is called desorption.

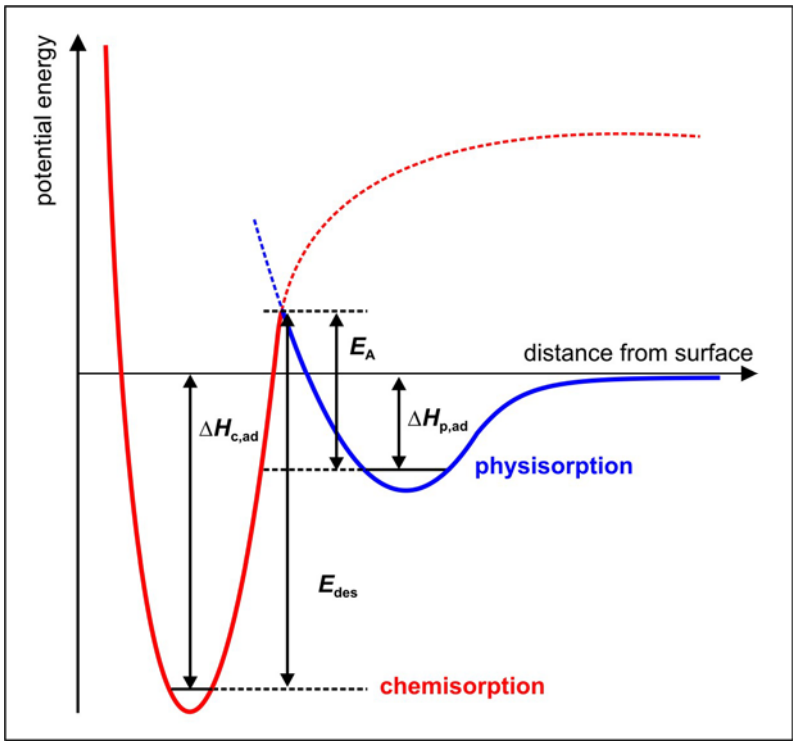

Figure 2.1: Adsorption / desorption energy potential as function of the surface distance r (dissociative chemisorption of O_2 on Pt) at constant pressure. $\Delta H_{c,ad}$: enthalpy of chemisorption, $\Delta H_{p,ad}$: enthalpy of physisorption, E_A: potential barrier between the chemisorbed and physisorped state.

Not only the chemisorption and physisorption have an impact on the reaction kinetics but they also influence the movement of the adsorbed molecule on the surface (surface diffusion). There are two types of surface diffusion, which can play important roles in coverage and deposition layers. The first type is called bulk diffusion, which describes the global macro-motion of the material within the deposited layer; the second type is surface diffusion, related to the motion of metal boundaries. If the molecules are bound so strong at the surface that no diffusion can occur, the catalyst looses its effect. Figure 2.2 shows the periodic potential of a crystal surface resulting from the interaction between the support atoms. The ratio between the height of the potential barrier and the thermal energy kT of the molecule specifies the mobility of the adsorbed molecules. If the diffusion energy E_{Diff} is distinctly smaller than the thermal energy, the adsorbed molecules move around the surface without any restriction. This behaviour changes in case of an E_{Diff}, which is much higher than kT. The surface movement of a molecule is then comparable to a jump from one surface atom to the next.

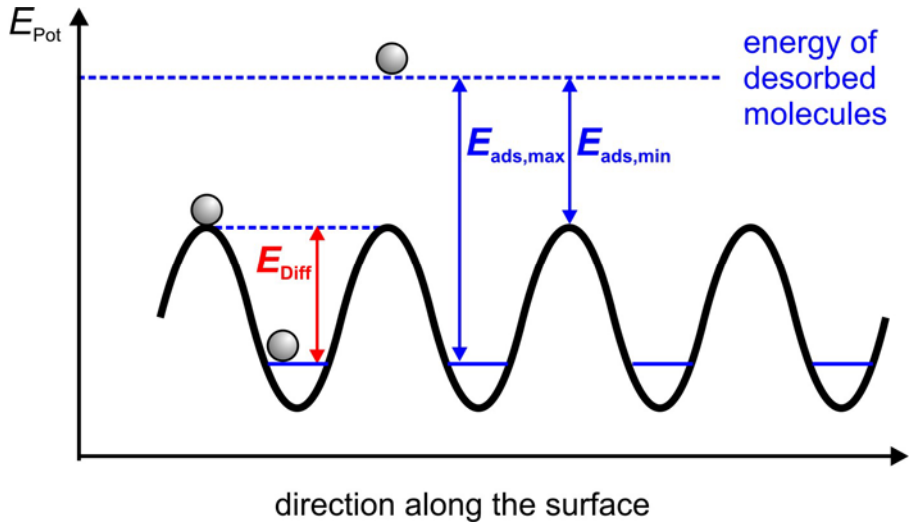

Figure 2.2: Periodic potential of a crystal surface

2.2 Surface-Reaction Mechanism: A Mean-Field Approach

There are two global mechanistic pictures describing the processes taking place at the surface of a catalyst, the *Langmuir-Hinshelwood* mechanism and *Eley-Rideal* mechanism. In the former, the gas-phase molecules *A* and *B* adsorb on the surface forming *A(s)* and *B(s)*, which then react with each other forming the product. The product-formation reaction is assumed to be slow compared to the establishment of an adsorption / desorption equilibrium. In the *Langmuir-Hinschelwood* mechanism, an adsorbed molecule *A(s)* reacts directly with gas-phase molecule *B*.

As mentioned previously, the rate of the catalytic reaction is strongly influenced by the physical properties of the catalyst. This means that every catalyst will have a unique rate expression depending on not only the type of catalytic material but also on the catalyst support, the type and structure of washcoat, and the method of manufacture. Different surface structures of the catalyst can lead to different reaction pathways and kinetic data. Furthermore, time dependent features of the reaction, such as recrystallisation due to variations in species concentration and temperature, and diffusion of adsorbed species into the catalyst bulk may modify the reaction rate.

There are several approaches to model catalytic reactions (Figure 2.3). Due to their complexity, global rate expressions and reaction rates are often used to be the model of choice for many years.[28, 48] The reaction rate has often been based on catalyst mass, catalyst volume, reactor volume, or catalyst-external-surface area and depends on temperature and gas-phase concentrations. The fitted kinetics are specific to the applied reactor geometry and chosen external condition. Prediction is very limited.

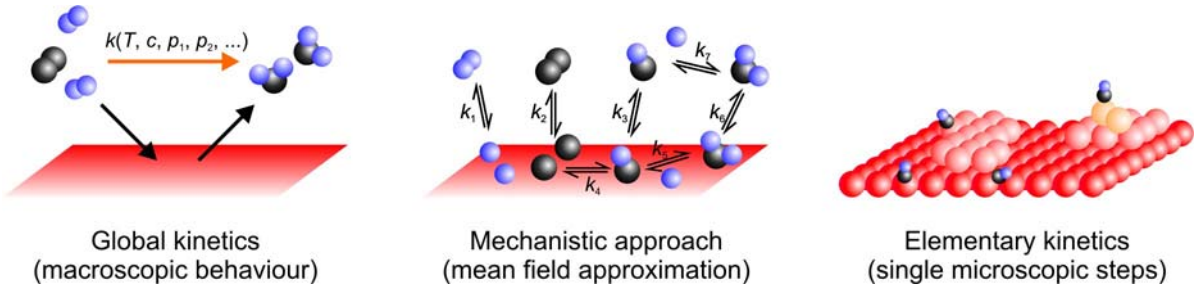

Figure 2.3: Scheme of three approaches to model catalytic reactions: a macroscopic, a mechanistic and a microscopic procedure.

The most detailed and exact way to calculate heterogeneous reactions would be an elementary-kinetic approach. Such an approach presupposes detailed knowledge of all reaction sites, surface structures as well as of the adsorption and desorption behaviour of all molecules at the solid catalyst. This information is difficult to gather. Only simple systems have been investigated by Monte Carlo simulations, e.g. CO oxidation on a Pt(111) single crystal.[49]

Nowadays, the so-called mean-field approximation is frequently used.[50] This approximation assumes that the adsorbates are randomly distributed on the surface, which is assumed to be uniform. This mechanistic approach is based on the molecular processes but does not take into account all single elementary events. In this model, heterogeneous reactions on solid surfaces can principally be treated by formalism very similar to that applied for gas-phase reactions. The ultimate goal of kinetic research therefore is the development of detailed reaction mechanisms based on the elementary steps occurring on the catalyst surface. All the simulations in this work are based on detailed reaction mechanism and the mean-field approximation.

CHAPTER III

3 Experimental Setup and Catalyst Preparation

The first part of this chapter will describe the setup used for the catalytic oxidation experiments and the analytical tools for the characterisation of the reactants and products.

Since it is very important to know in detail the properties of the catalyst for heterogeneous reaction kinetics, the second and third part focuses on catalyst preparation and characterisation, e.g. determination of catalytic surface area, distribution of catalytic material and pore-size distribution.

The fourth part summarises the results of the catalyst properties. These data will be the basis for the later simulations.

Finally, the evaluation of the experimental data and an estimation of the experimental error close this chapter.

3.1 The Flow Reactor

For an experimental and numerical kinetic study of reactive systems, it is very important to have a well-defined experimental setup, which can be described by the numerical model. Especially simple reactor models, such as tubular ones would ease the incorporation of detailed kinetic models, which can be simulated without much computational cost. This is important, where the focus is on chemical kinetics rather than on the flow field. Nevertheless, the reactor geometry can affect the product distribution due to the interaction of transport and chemistry. Therefore, a reactor, which was built in 1999,[51] is designed to meet this requirement and was also used

in this work.

Figure 3.1 briefly displays the setup. The most important part of the entire reactor is the 45 cm long chemically inert quartz tube where the catalyst is placed inside. Different span diameters of 1 cm, 1.5 cm, and 2.6 cm allow the investigation of chemical reactions on different catalyst sizes. Additionally, for several experiments a reactor was designed in which a platinum tube (MaTecK Material-Technologie & Kristalle GmbH) with an inner diameter of 1 mm and a length of 3.7 cm was fixed (Figure 3.2).

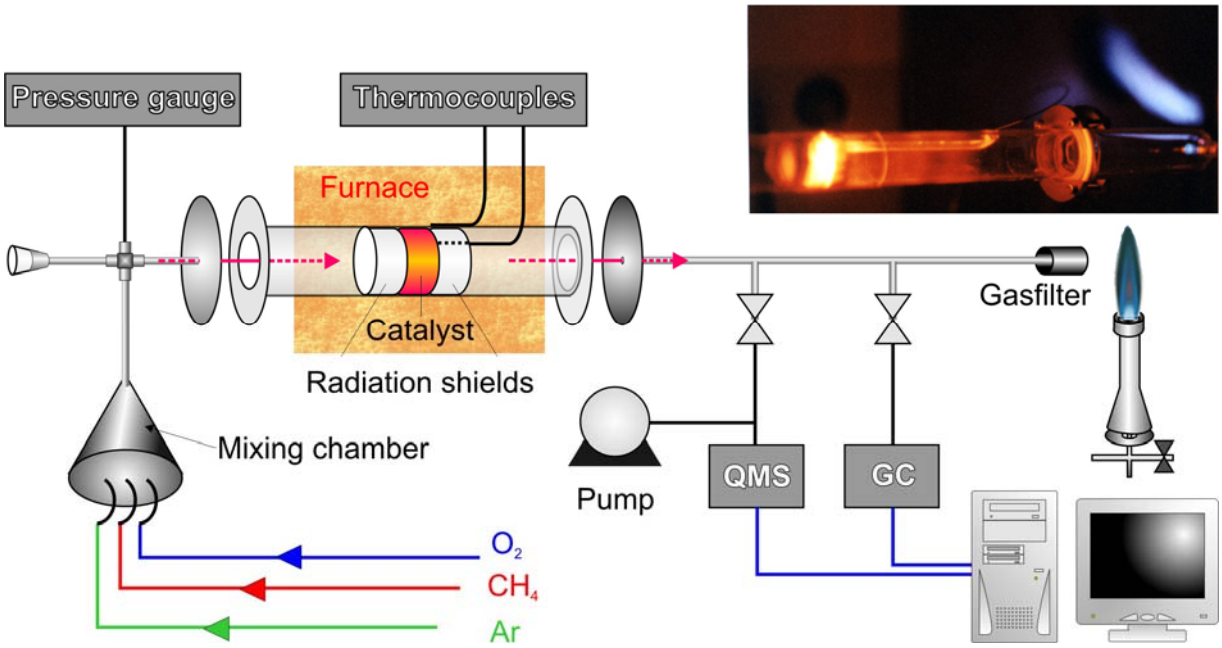

Figure 3.1 Simplified scheme of the experimental setup. Gases are mixed in a chamber and flow into the reactor placed in a furnace in which the catalyst is centred. The main stream of the product gas flow is burned at the exit and the product composition is determined by a QMS.

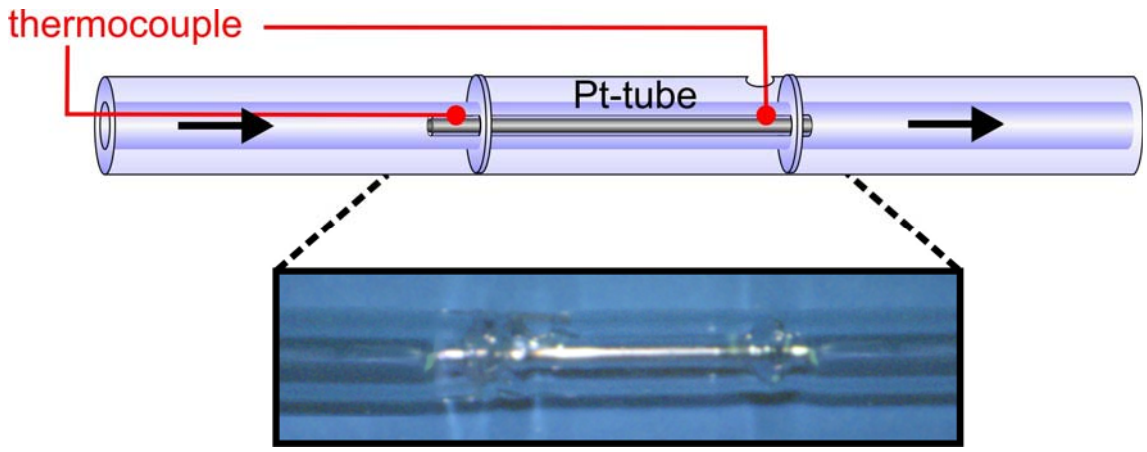

Figure 3.2: Quartz reactor designed for the 37 mm long Pt-tube with an inner diameter of 1 mm. A smaller quartz tube is mounted inside, just wide enough to hold the Pt-tube.

Two unloaded monoliths placed in front and rear of the catalyst reduce heat loss by radiation. A ceramic cloth wrapped around the catalyst, 1 mm thick, prevents any gas bypass. The gas temperature at the exit of the catalytic monolith is monitored using a nickel/ chromium/silicon-nickel/silicon (type N) thermocouple, which is placed inside a thin quartz sheath to prevent catalytic reactions. A second thermocouple is used to measure the temperature of the outer glass wall. A ceramic insulation placed around the quartz tube reduces the heat loss of the entire reactor.

The other parts of the reactor are made of stainless steal for safety reasons. The gases premixed in a mixing chamber, which is filled with glass rings, are fed into the reactor at defined flow rates. After passing the catalyst the main gas stream exits the reactor through a gas filter with a pore diameter of 7 µm and is burned by a bunsenburner. The small pores of the filter prevent a flashback of the flame. A cork at the entrance of the flow is used as high pressure safety valve. The product composition is determined by gas chromatography (GC, Varian GC-Workstation 3380) and quadrupole mass spectroscopy (QMS, Balzers QMG 311), permitting to study ignition and extinction phenomena. However, in the scope of this work the GC served only to verify the QMS data and will not be described in detail.

The entire reactor can be operated either autothermally or temperature-controlled by a furnace (Buddeberg, CARBOLITE HST 12/--/200). The reactor is operated at atmospheric pressure in all cases and the product lines are heated to 150 °C to prevent H_2O condensation.

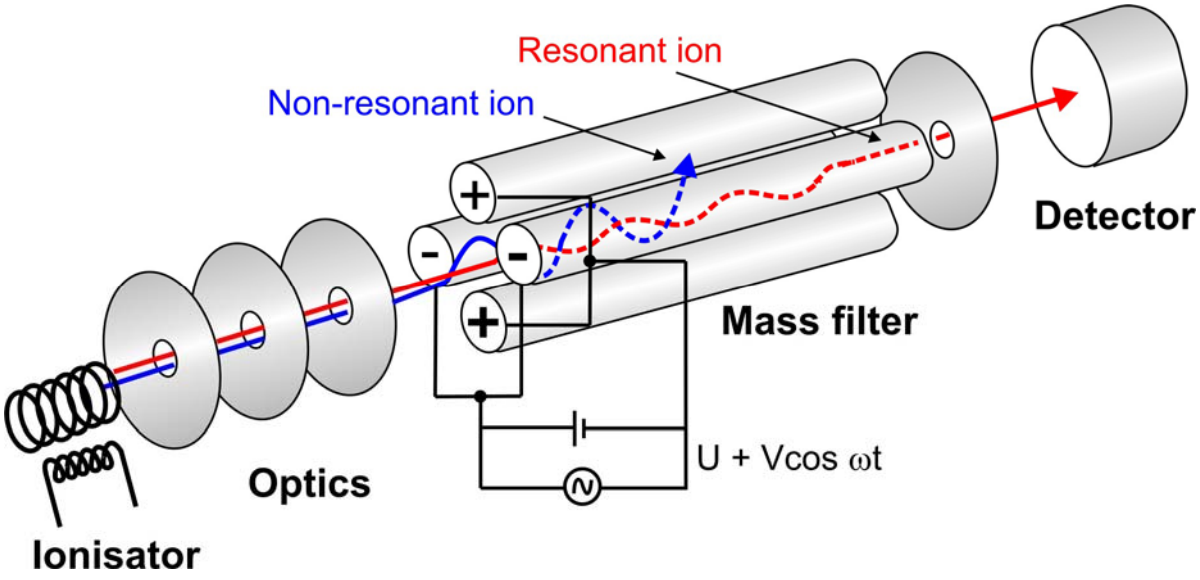

Figure 3.3: Scheme of a QMS. The red line symbolizes a resonant ion reaching the detector; the blue line displays a non-resonant ion.

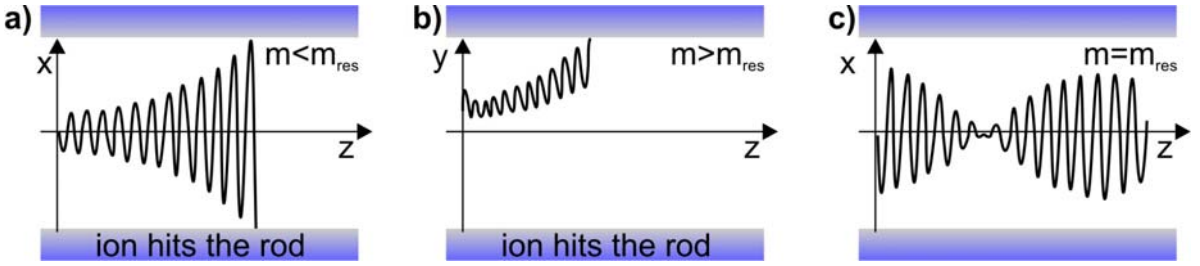

Figure 3.4: a) Unstable trajectory of an ion with a mass smaller compared to the resonant mass; b) unstable trajectory of an ion with a higher mass; c) stable trajectory of the resonant ion in all three coordinates.[52]

3.1.1 Analytical System

a) Principles of Quadrupole Mass Spectrometry

A Mass spectrometer is a standard device for many analytical systems. It is an indispensable tool e.g. in chemistry, biochemistry, pharmacy, and medicine. However, since the 1950s to the present mass spectrometry (MS) has changed a lot and is still changing.[53]

While the first machine consisting of a magnetic sector with electron ionisation delivered only a few mass spectra per day, modern highly automated systems achieve thousands. The basic principle of MS is to generate ions from the compound, to separate these ions by their mass-to-charge ratio (m/z) and to detect them by their m/z and abundance qualitatively and quantitatively. Since one scope of this work is to investigate transient

phenomena during reactions, a quadrupole mass spectrometer (QMS) was used and will be described briefly. The main advantage of a QMS is the high scan speed, which is realised by sweeping electric potentials. Also worth mentioning is the high transmission, light weight and compactness of the system, and the low ion acceleration voltage. For more details of MS in general the reader may be referred to [54].

The principle of a quadrupole mass analyser is depicted in Figure 3.3. It consists of four hyperbolically or cylindrically-shaped rod electrodes extending in the *z*-direction and mounted in a square configuration. The pairs of opposite rods are held at the same potential composed of a DC voltage U and AC component V with the frequency ω. The potential φ of a hyperbolic quadrupole field is described by

$$\begin{aligned} \varphi &= \varphi_0 \cdot \left(\alpha^2 + \beta y^2 \cdot \gamma z^2\right) \\ \varphi_0 &= U + V \cdot \cos\left(\omega t\right) \end{aligned} \tag{3.1}$$

In case of two dimensions the following is valid: $\alpha = -\beta = 1/r_0^2$ and $\gamma = 0$, where $2 \cdot r_0$ is the distance between two electrodes.

As an ion enters the quadrupole assembly in *z*-direction the rod with the opposite charge attracts the ion. Since the voltage applied to the rods is periodic, attraction and repulsion in both the *x*- and *y*-direction are altering in time. Ions with a certain mass can pass the mass analyser without hitting the rods, presupposed their motion around the *z*-axis is stable and amplitudes in the *xy*-plane are limited. Ions with a lower mass than that of the resonant ion are affected more strongly by AC causing an energy transfer. The amplitude increases until the ions hit the rod (Figure 3.4a). Ions with higher masses are less influenced by AC. On the other hand, the DC deflects their trajectory as shown in Figure 3.4b.

This motion of an ion in *x*-, *y*- and *z*- direction can be described by a set of differential equations, called *Mathieu equations*.[55, 56]

$$\begin{aligned} &\frac{d^2x}{dt^2} - \frac{\omega^2}{4}\left(a + 2q \cdot \cos\left(\omega t\right)\right) \cdot x = 0, \\ &\frac{d^2y}{dt^2} - \frac{\omega^2}{4}\left(a + 2q \cdot \cos\left(\omega t\right)\right) \cdot y = 0, \\ &\frac{d^2z}{dt^2} = 0 \end{aligned} \tag{3.2}$$

The parameters a and q are described by

$$a = \frac{4eU}{m r_0^2 \omega^2} \quad \text{and} \quad q = \frac{2eV}{m r_0^2 \omega^2} \tag{3.3}$$

and lead to the stability diagram of a 2D quadrupole field depicted in Figure 3.5 by plotting a versus q.[56, 57] Depending of a and q the motion of the ion is either stable or unstable. This reveals the existence of four regions where x- and y-trajectories are stable (area marked yellow), either x- or y-trajectories are stable and no stable ion motion occurs. Since all masses remain on the straight line (blue) with a slope of $a/q = 2\ U/V$ leading through the origin, the cut of this line with the stable x/y-area leads to the q-interval $[q_1, q_2]$ in which the ions with the corresponding mass reach the detector.

Ions with higher mass become unstable in y-direction, ions with lower mass in x-direction. If the ratio a/q is chosen that way, that the scan line hits the area with stable x- and y-trajectories in its apex ($U/V = 0.167$), the maximum resolution is obtained. By varying the magnitude of U and V at constant U/V ratio a $U/V =$ constant linked scan is obtained allowing ions of increasingly higher m/z values to travel through the quadrupole.

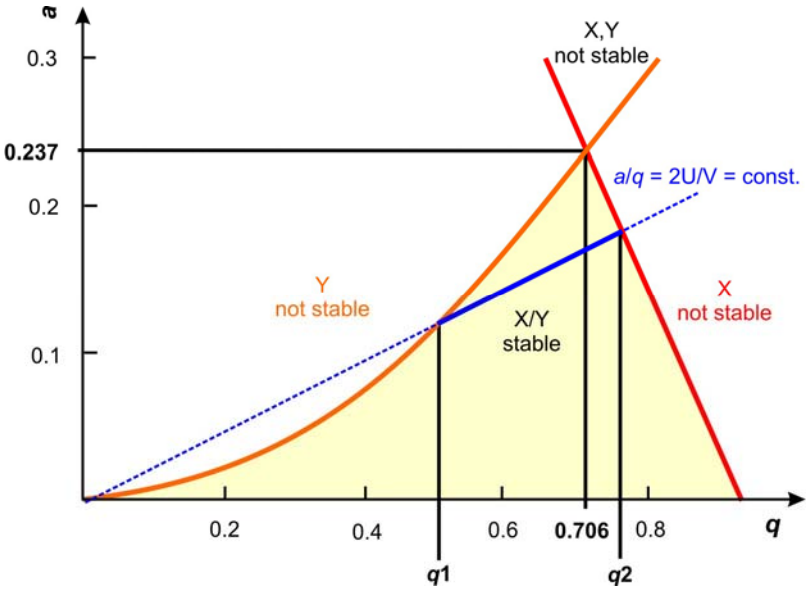

Figure 3.5: Stability diagram of the quadrupole mass filter. Only ions on the straight line (blue) and in the yellow area reach the detector.

b) Materials and Methods

Thermocouples

Type N thermocouples were procured from Thermocoax. A Nicrosil/Nisil thermocouple (DIN IEC 58i4) can measure temperatures up to 1300 °C. The thermometer is a Fluke 53-II and 54-II.

Mass-Flow Controllers (MFC)

In order to regulate different feed-gas flows as exact as possible, Tylan MFCs in a range between 10 ml min^{-1} and 8 slpm are used. (Type FC-2900 and FC-260)

Furnace

The CARBOLITE furnace was provided by Buddeberg GmbH.

- Model: HST 12/--/200
- Controller (Eurotherm): 2416CC
- Maximum temperature: 1200 °C

Chemicals

- Rhodium: Rhodium(III)sulphate Premium, 99.99%, Alfa Aesar
- Palladium: Palladium(II)chloride, 99.9%, Alfa Aesar
- Platinum: Dihydrogen-hexachlorplatinate(IV), 99.90%, Alfa Aesar
- Washcoat: DISPERSAL (alumina), CONDEA Chemie GmbH
- Platinum tube: Material-Technologie & Kristalle GmbH
- Hydrochloric acid, aluminium nitrate, VWR

Mass Spectrometer

The used mass spectrometer is a BALZERS QMG 311. It consists of a control unit QMS 311, an analyser QMA 140 with SEM (secondary electron multiplier), and a detector unit composed by an amplifier QME 301 and an ion counter QRV 101. Following parameters were applied:

- Ionisation energy: 40 eV
- Maximum/used pressure in QMS: $1 \cdot 10^{-5}$ Torr / $1 \cdot 10^{-6}$ Torr
- Detection limit for the partial pressure: $\leq 10^{-14}$ Torr
- Software: QUADSTAR 421, Version 2.14

For the quantitative evaluation of the measurements, it is necessary to calibrate the mass spectrometer in order to find a correlation between the observed signal and the concentration of the species. Since the measured current is directly proportional to the number of molecules hitting the detector in the entire range of concentrations, one

calibration gas can be used. The calibration gas consisting of 40.00 vol.-% H_2, 1.99 vol.-% CH_4, 48.89 vol.-%. CO, 1.02 vol.-% O_2, and 08.10 vol.-% CO_2 was procured by MESSER Griesheim GmbH; the concentrations are given as molar fractions. Since water is difficult to calibrate, its value is calculated by closing the H/O balance. However, the amount of water was measured in each experiment in case some unexpected phenomena should occur but it was not calibrated.

3.2 Catalyst Preparation

Cordierite and alumina honeycomb monoliths served as support material. The large, open frontal area, giving access to straight channels results in an extremely low pressure drop and prevents the accumulation of dust. Out of the numerous methods to prepare heterogeneous catalysts [45, 58] only those, which are applied for the investigations described in this thesis, are mentioned below.

3.2.1 Wet Impregnation Method

The monoliths were coated with rhodium, palladium, or platinum. For the impregnation method a 0.05 molar aqueous solution of the particular noble metal salt was prepared. In case of Rh an acidic aqueous solution of $Rh_2(SO_4)_3 \cdot 4\ H_2O$ was used, for Pd an aqueous solution of $PdCl_4$, for Pt an aqueous solution of H_2PtCl_6.

The impregnation with the metal was achieved by saturating the monolith with the solution, followed by 24 hours drying at 400 K, calcination in air at 775 K for 18 hours, and finally reduction in H_2 at 775 K. This procedure stabilises the catalyst and removes all unwanted molecules or ions, e.g. sulphate, nitrate, chloride and leads to metal loadings of about 3 wt.-%. Energy dispersive X-ray spectroscopy (EDX) measurements showed that no chlorine or sulphur compounds were left on the catalyst surface after impregnation. Alumina, cordierite, or cordierite treated with an alumina washcoat served as catalyst support.

3.2.2 Use of Washcoat for Higher Surface Area

In principle, washcoating means depositing a layer of high surface area oxide(s) onto the surface of a low surface area monolithic support. Active elements can be incorporated into the layer either during the washcoating step or after the washcoat has been deposited, using any appropriate technique.

To achieve a washcoat loading of 3 wt.-%, 12.6 g of γ-alumina (DISPERSAL, CONDEA Chemie GmbH) was suspended in saturated $Al(NO_3)_3$ solution. By stirring the

solution for 30 minutes, a highly viscous liquid was obtained. The monoliths were covered completely with the suspension, first under reduced pressure (100 mbar for 15 min) and afterwards for 12 h at atmospheric pressure. The liquid was removed and the monolith was purged from excess solution by blowing air through the channels. Finally, the honeycombs were dried for 1 h at 60 °C, 1 h at 100 °C and 1 h at 150 °C. To form the stable α-alumina the monolith was calcined in air by heating up the furnace to 600°C within 6 h and keeping the temperature for 4 h.

3.2.3 Production of Rh-Nano-Powder by Laser Ablation

a) Production of Rhodium Nano-Powder

The rhodium nano-powder used in this work was produced by Laser ablation by N. Savastenko[1] as depicted in Figure 3.6. Here the accrued particles collide with the flowing gas, leading to the formation of the nano-powder. The rhodium nano-powder entrained by the carrier gas was collected in a glass cylinder placed inside the chamber with an ablation rate of 0.3-0.4 mg min^{-1}. The average diameter of one particle was found to be 2 nm.[59]

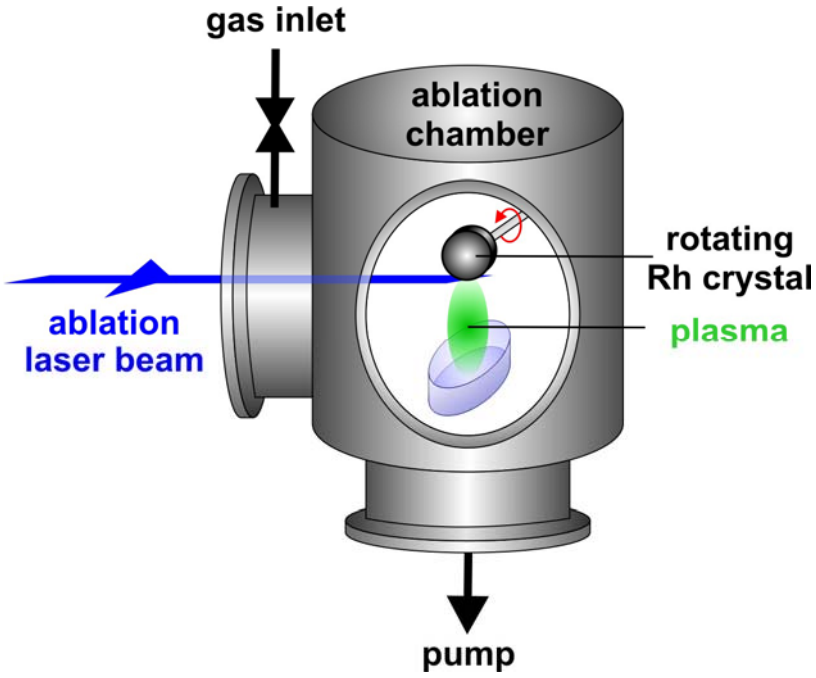

Figure 3.6: Scheme of the experimental setup of Laser ablation. The setup consists of a vacuum chamber with associated systems for laser beam focusing and gas handling.

[1] Dr. Natalie Savastenko, University of Heidelberg, Institute of Physical Chemistry

The Laser ablation was carried out with a KrF excimer laser (Lambda Physik, EMG-201, wavelength: 248 nm, repetition rate: 10 Hz, fluency 22 J cm^{-2}). A Rh bulk disc from Mateck Gmbh (purity 99.9 vol.-%), placed on a rotating target holder in order to prevent hole drilling, served as the target. One chamber port contains a stepper motor, which allows a target holder rotation rate of 5 rps. The ablation was performed under constant gas flow conditions. After evacuating the chamber to 10^{-7} kPa high-purity helium gas (Messer Griesheim; purity: He 99.996 vol.-%) was introduced into the chamber at a pressure of 1 kPa with a flow rate of 12 ml min^{-1}. The gas-entrance valve was placed near the laser-beam entrance window in order to protect the windows from the ablation plume. The gas was pumped out of the chamber through cellulose membrane filters (Schleicher & Schuell GmbH, pore size 25 nm).

b) Preparation of the Nanoparticle Catalysts

The reactions are carried out in a flow reactor where monoliths are used as catalyst support. Therefore, it is necessary to deposit the Rh nanoparticles on the support. For that purpose, it is necessary to fix the Rh nanoparticles on a monolithic support. Since the material is very expensive and the preparation of nanoparticles is time consuming, each support was weighed and the amount of Rh used for one impregnation was exactly 3.5 wt.-% of the plain catalyst. Two different methods were tried: Firstly, the powder was slurred in 1 ml distilled water, secondly it was suspended in a mixture of 0.1 ml DISPERSAL suspension (see Chapter 3.2.2) and 0.9 ml water.

In case of the aqueous slurry the powder sedimented after some time and therefore the liquid was stirred well before impregnating the catalyst. In the slurry as well as in the suspension the nanoparticles formed μm size clusters. In order to minimise losses of the catalytic material, only a few drops of the liquid were filled into the channels of the monoliths. After drying at room temperature the monoliths were turned upside-down and filled again. This was repeated until no liquid was left over. For better comparison with conventionally prepared catalysts, these monoliths were calcined the same way by heating up to 600°C in 6 h and keeping the temperature for 4 h in air.

3.3 Characterisation of the Catalysts

The exact characterisation of the catalyst is important for simulating heterogeneous reactions, because surface area, porosity, pore size and structure, and the catalytically active surface area influence reaction kinetics. The obtained data will be applied in simulations as described in Chapter 4.

3.3.1 CO Chemisorption

Chemisorption is defined as a very strong adsorption due to chemical bonding of the adsorbate with the adsorbent. In common, H_2 or CO is used as adsorbent. Since in case of CO as adsorbate one CO molecule bonds to exactly one catalyst centre (metal atom), the dispersion of the active catalyst on a catalytically inactive support can be derived.

The number of active metal centres can be determined by chemisorption of CO or H_2.[1, 45] According to (3.4) hydrogen adsorbs on metals dissociatively, CO as a molecule resulting in a stoichiometry of one CO molecule or H atom per surface metal atom.

$$\begin{aligned} H_2 + 2\,M(s) &\rightleftharpoons 2\,M(s)\text{-}H \\ CO + M(s) &\rightleftharpoons M(s)\text{-}CO \end{aligned} \qquad (3.4)$$

First, the sample is reduced at atmospheric pressure in pure H_2 at 300 °C for 2 h, and then the H_2 is removed by a He flow for 10 min. The system is evacuated at 300 °C to remove water for 22 h until a pressure of 10^{-6} mbar is reached. After cooling to room temperature (RT) the sample is weighed. After heating the sample to 40 °C at a pressure of 53 mbar, pure CO is fed into the reactor until 133 mbar are reached. To determine the CO coverage the uptake of CO is measured after an equilibrium delay of 30-60 min. The system is evacuated again to 10^{-6} mbar in ½ h and the measurement is repeated. After evacuating for another ½ h the empty volume is determined by running the measurement in 100% He.

To evaluate the adsorbed CO amount the *Langmuir*-isotherm is back extrapolated to $1/p = 0$. The CO volume results from the *y*-intercept. From the chemisorbed volume v_{mono} required to form the monolayer, the specific metal surface area A is given by

$$A = \frac{v_{mono}}{22414} \cdot N_A \cdot n \cdot \frac{1}{m} \cdot a_m \cdot \frac{100}{wt} \quad [m^2 \cdot g^{-1}\ \text{metal}] \qquad (3.5)$$

A = specific metal surface area
v_{mono} = chemisorbed volume
N_A = Avogadro's constant ($6.022 \cdot 10^{23}$ mol^{-1})
n = chemisorption stoichiometry
m = mass of the sample [g]
a_m = surface area occupied by metal atom [N_2:16.2 Å]
wt = metal loading

The metal dispersion D is directly obtained by

$$D = \frac{v_{\text{mono}} \cdot n}{22414} \Big/ \frac{wt}{100 \cdot M} \tag{3.6}$$

D = metal dispersion
M = atomic mass of metal

The measurements of the CO chemisorption of Pt, Rh, and Pd loaded catalysts were done with a setup from Type Sorptomatic 1990, Porotec/Frankfurt incorporation by Ochs[2].

Basic information can be found for example in the monograph of Anderson. [60]

3.3.2 Nitrogen Sorptometry, BET

Physisorption is a general phenomenon and, unlike chemisorption, occurs whenever a gas is brought into contact with a solid surface. Nitrogen at 77 K (boiling temperature) is generally considered to be the most suitable adsorptive for the determination of specific surface area of nonporous, macroporous, or mesoporous solids.

Therefore, the isotherm of N_2 at the catalyst surface is measured to determine the specific surface and pore radii distribution of the monoliths.[61, 62] The *Brunauer-Emmett-Teller* (BET) method [63] is used to evaluate the physisorption isotherm data. The so-called BET-equation

$$n_{\text{ads}} = n_{\text{m}} \frac{C\left(p/p_0\right)}{\left(1-\left(p/p_0\right)\right)\left(1+\left(C-1\right)\left(p/p_0\right)\right)} \tag{3.7}$$

leads to the amount n_{m} of N_2 of one monolayer and equation (3.8) to the specific surface area a_{s}(BET).

$$\frac{p/p_0}{n_{\text{ads}}\left(1-p/p_0\right)} = \frac{1}{n_{\text{m}} \cdot C} + \frac{C-1}{n_{\text{m}} \cdot C} \cdot \frac{p}{p_0} \tag{3.8}$$

$$a_{\text{s}}\left(\text{BET}\right) = n_{\text{m}} \times \text{N}_{\text{A}} \times a_{\text{m}} \tag{3.9}$$

p = equilibrium pressure of the adsorptive
p_0 = saturation pressure of the adsorptive
n_{ads} = amount of adsorbed gas
n_{m} = amount of adsorbed gas at one monolayer

[2] Andrea Ochs, University of Karlsruhe, Institute for Chemical Technology and Polymer Chemistry

C = constant
a_s(BET) = specific surface area
a_m = average area occupied by the adsorbate molecule

The pore radius r_p of micro- and mesopores can also be derived by the adsorption isotherm. The estimation of the pore volume is based on the fact that gas condenses to liquid in narrow pores at pressures less than the saturated vapour pressure of the adsorbate. This results in a hysteresis loop in the isotherm.[64, 65] The model description assumes that pores are capillaries with an inner diameter of r_k (*Kelvin radius*) and the pressure drop is due to the curved liquid-like meniscus of the condensed gas.[61] The Kelvin radius r_k is given by:

$$r_k = \frac{-2\gamma V_m}{RT \cdot \ln(p/p_0)} \tag{3.10}$$

γ = surface tension of liquid nitrogen
V_m = molar volume of liquid nitrogen

The radius of a model pore r_p is given by:

$$r_p = r_k + t_{ads} \tag{3.11}$$

$$t_{ads} = \frac{C}{\log(p/p_0) + 0.034}$$

t_{ads} = thickness of the multilayer
C = constant

The isotherms were measured using a sorptiometer “Sorptomatic 1990”, Porotec / Frankfurt by Ochs[2]. Before the measurement started the catalysts were treated at a pressure of $3 \cdot 10^{-4}$ mbar and 400 °C for 12 h to remove adsorbed molecules. For more details see references [1, 45, 61, 64].

3.4 Summarising the Properties of Applied Catalysts

As mentioned previously the properties of the catalytically active surface area need to be taken into account for the simulation of the experiments. Therefore, BET and catalytically active surface-area measurements were carried out for each catalyst used to estimate the surface-scaling factor $F_{cat/geo}$ for the simulations. Since for such measurements around 2 g of sample are required, and the mass of most of the used catalysts was about 0.5 g or less, the results compiled in Table 1 are average values obtained from several unused catalysts. Since used monoliths lost too much of surface area due to sintering of the catalytic material, measurements of the BET-surface did not yield any reasonable results. The catalytically active surface area is about two orders of magnitude smaller than the BET surface (Table 1). Most of the used catalysts obtain such a low BET area, that the measurement of the catalytically active surface area was not possible. From previous work it is known, however, that under conditions applied during the work reported here, significant loss of surface due to sintering takes a long enough time that it can be neglected.[51]

Table 1: Summary of measured BET and catalytic surface area of a monolith

Catalyst	Amount of channels	Total lateral face [m^2]	Mass [g]	BET [$m^2\ g^{-1}$]	Cat. surface area [$m^2\ g^{-1}$]	Tot. surface area [m^2]	Exp. $F_{cat/geo}$	Applied $F_{cat/geo}$
3% Rh, alumina	*24 triangular*[c]	*$3.6\cdot10^{-4}$*	*0.0855*[a] --[b]	*205.4*[a] --[b]	*2.63* --[b]	*0.22* --[b]	*625* --[b]	*45*
3% Rh, cordierite	*234 square*[c]	*$9.36\cdot10^{-3}$*	*1.7869*[a] *1.6148*[b]	*20.9*[a] *4.7*[b]	*0.45*[a] --[b]	*0.81*[a] --[b]	*87*[a] --[b]	*12*
3% Pt, washcoat cordierite	*234 square*[c]	*$9.36\cdot10^{-3}$*	*2.0850*[a] *1.8483*[b]	*29.3*[a] *19.4*[b]	*0.88*[a] --[b]	*1.84*[a] --[b]	*197*[a] --[b]	*20*
3% Pd, washcoat cordierite	*234* *54*[b] *square*[c]	*$9.36\cdot10^{-3}$*[a] *$2.16\cdot10^{-3}$*[b]	*1.8808*[a] *0.4682*[b]	*24.0*[a] *20.1*[b]	*0.22*[a] *0.17*[b]	*0.33*[a] *0.10*[b]	*47*[a] *35*[b]	*1.5*

[a]: values of new catalyst, [b]: values of a used catalyst, [c]: shape of a singular channel

A comparison of measured and applied geometry factors clearly shows that the measured and applied factors differ considerably. Nevertheless, it needs to be considered that a catalyst looses the highest amount of its activity between the first and second measurement. Its catalytic activity remains more or less constant after the first use for the period of its use here. Therefore, the experimental achieved $F_{cat/geo}$ is higher compared to the expected one. The difference of the BET surface area of a used and unused catalyst gives a hint on the change. Even while taking this into account the $F_{cat/geo}$ of the simulation is too low. This is due to the fact, that the detailed reaction mechanism does not consider real surface-area measurements. It needs to be fine-tuned by changing the Arrhenius coefficients.

3.5 Evaluation and Error Estimation

3.5.1 Calculating Selectivities and Conversions

As mentioned in chapter 3.1.1, the mass spectrometer counts the ions hitting the detector as an ion current. Therefore, the intensity I_i is proportional to the number of ions n_i and the mole fractions X_i. The mole fraction of a species i is given by:

$$X_i = \frac{I_i}{\sum_i I_i} = \frac{n_i}{\sum_i n_i} \tag{3.12}$$

The mass fractions can be calculated from the mole fractions and the average molar mass $\overline{M} = \sum X_i \cdot M_i$:

$$Y_i = \frac{X_i \cdot M_i}{\overline{M}} \tag{3.13}$$

Before the mole and mass fractions are calculated, it is necessary to calibrate the measured current using a calibration gas with an exactly known composition leading to a calibration factor for each species. The selectivities S_i for the formation of H_2 and CO are calculated using the mole fractions, the conversions U_i of O_2- and CH_4 are determined from the mass fractions. An additional component c_x stands for the sum of other products containing carbon such as C_2H_2. However, in the experiments where the selectivities are calculated, no such products were examined. Therefore $X_{C_xH_y} = 0$.

H_2- and H_2O-selectivity:
$$S_{H_2} = \frac{X_{H_2}}{X_{H_2} + X_{H_2O} + yX_{C_xH_y}} \quad \text{and} \quad S_{H_2O} = \frac{X_{H_2O}}{X_{H_2} + X_{H_2O} + yX_{C_xH_y}} \tag{3.14}$$

CO- and CO_2-selectivity:
$$S_{CO} = \frac{X_{CO}}{X_{CO} + X_{CO_2} + xX_{C_xH_y}} \quad \text{and} \quad S_{CO_2} = \frac{X_{CO_2}}{X_{CO} + X_{CO_2} + xX_{C_xH_y}} \tag{3.15}$$

CH_4-conversion:
$$U_{CH_4} = \frac{Y(CH_4)_{in} - Y(CH_4)_{out}}{Y(CH_4)_{in}} \tag{3.16}$$

O_2-conversion:
$$U_{O_2} = \frac{Y(O_2)_{in} - Y(O_2)_{out}}{Y(O_2)_{in}} \tag{3.17}$$

In the combustion study, the CO_2-yield is calculated by $yield(CO_2) = U_{CH_4} \cdot S_{CO}$.

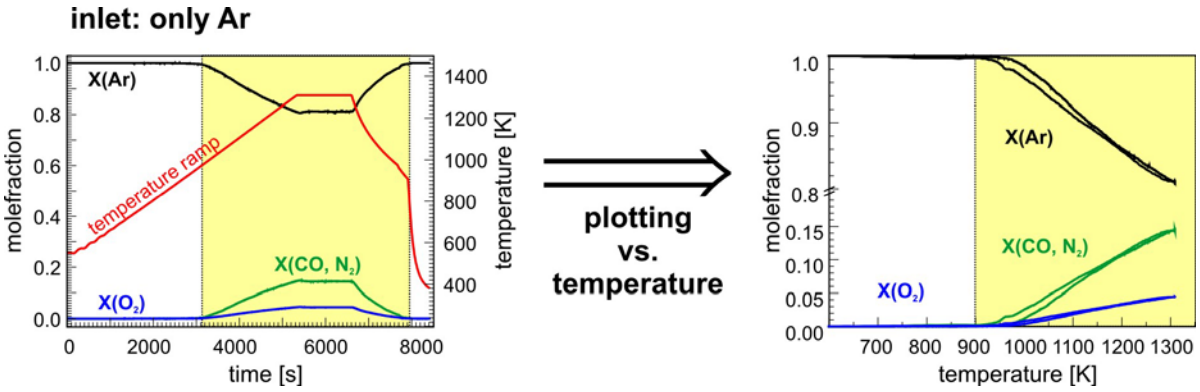

Figure 3.7: Mass spectrum of pure Ar (471.2 ml min^{-1}) at a temperature increase up to 1300 K. The yellow area highlights the temperature range when air is coming in to the mass spectrometer. The molar fractions of Ar, O_2, and CO are plotted versus temperature and the functions fitted. (using the ideal gas law at RT and normal pressure a volume of 471.2 ml leads to n_{total} = 0.019518 mole)

3.5.2 Evaluation of the Pt-Tube Experiments

Some difficulties occurred during the measurements with the Pt-tube. For reasons the author does not fully understand, air invaded into the measuring system at the exit of the reactor. Figure 3.7 shows the corresponding mass spectrum and the plot of the mole fractions versus time. The access of the additional air to the catalyst can be excluded by the observation that even in case of approximately stoichiometric compositions of the feed gas, the temperature increase during ignition was limited.

From this observation follows that it is necessary to calculate the amounts of extra O_2 and N_2. Since the mass of N_2 is the same as CO the N_2 molecules seem to enhance the signal for CO. These incoming molecules $n_{CO}(T)$ and $n_{O2}(T)$ need to be subtracted from the measured values. Then the dilution needs to be taken out of the system by multiplying each species with a dilution factor $D_{Ar}(T)$ given by:

$$D_{Ar}(T) = \frac{1}{X_{Ar}(T)} \tag{3.18}$$

The measured intensity for each species is multiplied with the calibration factor and finally the mole fraction is calculated.

$n_{CO}(T)$ and $n_{O2}(T)$ can be obtained by plotting the corresponding mole fractions versus temperature (Figure 3.7, right). Following equations can be set:

$$
\begin{aligned}
1 - X_{\mathrm{Ar}}(T) &= X_{\mathrm{CO}}(T) + X_{\mathrm{O_2}}(T) \\
n_{\mathrm{Ar}}(T) &= n_{\mathrm{total}} \cdot X_{\mathrm{Ar}}(T) \\
n_{\mathrm{total}} - n_{\mathrm{Ar}}(T) &= n_{\mathrm{CO}}(T) + n_{\mathrm{O_2}}(T)
\end{aligned}
\tag{3.19}
$$

$X_i(T)$ are the functions of mole fractions versus temperature, n_{total} the total amount of molecules (using the ideal gas law at room temperature and atmospheric pressure, a volume flow of 471.2 ml min^{-1} leads to a n_{total} = 0.019518 mole min^{-1}).

Equation (3.19) and the factor $f(T) = \dfrac{X_{\mathrm{CO}}(T)}{X_{\mathrm{O_2}}(T)} = \dfrac{n_{\mathrm{CO}}(T)}{n_{\mathrm{O_2}}(T)}$ lead to:

$$
n_{\mathrm{CO}}(T) = \frac{f(T)}{f(T)+1}\left(n_{\mathrm{total}} - n_{\mathrm{Ar}}(T)\right) \quad \text{and} \quad n_{\mathrm{O_2}}(T) = \frac{1}{f(T)+1}\left(n_{\mathrm{total}} - n_{\mathrm{Ar}}(T)\right) \tag{3.20}
$$

For the correction of the spectrum we only need to fit two functions, the dependency of the signal for Ar on the temperature $X_{\mathrm{Ar}}(T)$ and the proportion $f(T)$ between $X_{\mathrm{CO}}(T)$ and $X_{\mathrm{O2}}(T)$.

Figure 3.8 shows the raw mass spectrum during a measurement in the Pt-tube and the corrected and calibrated spectrum. It can clearly be seen that air is coming in (left). This results in a O_2 and CO increase before ignition, which is indicated by a sudden temperature rise together with CO_2 production.

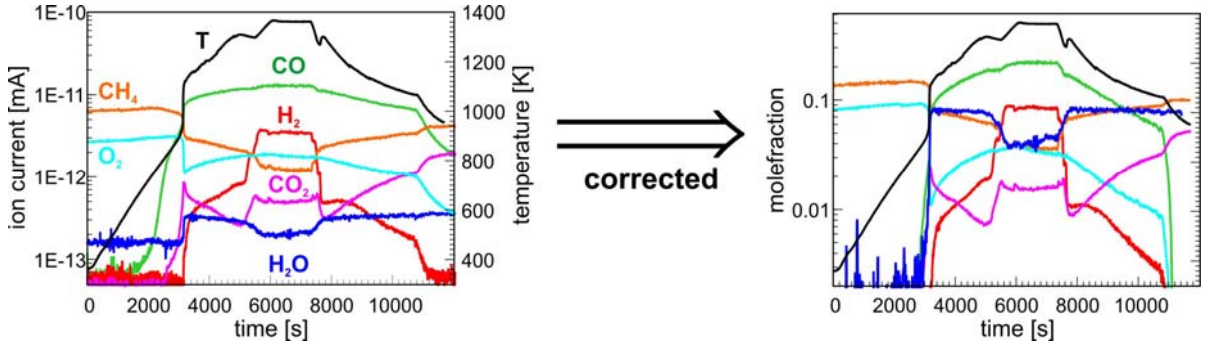

Figure 3.8: Original mass spectrum before correction. An increase in the signals for oxygen and CO together with a decrease of the signal for methane before ignition indicates that air is coming into the system. The right hand side shows the spectrum after correction. (Example: CPO of methane, 75% Ar, CH_4/O_2 = 1.47, v = 10 m s^{-1})

3.5.3 Error Estimation

Since the system is calibrated prior to each series of measurements, the error differs a little from one series to the other and is depicted by error bars in the diagrams.

The error in the temperature measurement is in the order of 10 K, although the thermocouple can measure the temperature as accurate as ± 0.1 K. This is due to a certain delay of the temperature measurement during fast increases of the temperature by the furnace or the reaction start-up and the influence of radiation of the furnace.

The gas flow was regulated by mass-flow controllers (MFCs) manufactured by the company Tylan, the error of which is ± 1% of the maximum value. Since the flow controllers were calibrated using a bubble expansion column, the error is estimated using the deviation of calibration curves. In all cases, the error is around 2%.

The errors of the single flows of CH_4 and O_2 lead to an error of around 2.8% for the CH_4/O_2 ratio.

Since the flow velocity and the concentration of argon are proportional to the total gas flow, their error is composed by the errors of all flow controllers used during the measurement. In most cases, only three flow controllers were in use at the same time leading to an error of 3.5%.

Not only the errors of the gas flows contribute to the total error of the detection of the gases, the variance of the mass spectrometer needs to be taken into account, too. Its error depends on one hand on the deviation of the calibration curves and on the other hand on the fluctuation of the intensity. For molecules present in very low concentrations (up to a signal of 10^{-13}) the error is around 15%, for signals up to 10^{-12} about 7%, and for signals up to 10^{-11} about 5%. This corresponds to a total relative error of the gases Ar, CH_4, O_2, H_2, CO_2, CO between 6% and 15%.

Since the selectivities and conversions are calculated using values for several species, their errors can be estimated to be in a range between 15% and 20%.

CHAPTER IV

4 Modelling and Simulation of High-Temperature Catalysis

The details of simulations of reaction kinetics depend on many physical and chemical processes depicted in Figure 4.2. On the catalytic active surface, for example, the local reaction rate depends on local gas-phase concentrations, temperature, surface coverage, and catalyst material. The global kinetics is in addition influenced by size and structure of the catalytic surface, the type of support or washcoat and the resulting heat conductivity, reaction mechanism, and ratio between the rates of elementary reaction steps (like adsorption, desorption, reaction steps, and surface diffusion). Not only the sequence of elementary steps on the surface plays an important role in this kinetic study, but also processes in the gas phase, e.g. transport of momentum, species, and energy, convection, gas phase reactions, and thermal radiation.

Therefore, the first part of this chapter will comment on the reaction kinetics of a reactive-flow system in general, followed by a description of the kinetics implemented in a recently developed computer program by Deutschmann, Tischer and Fechtenkötter applied in the work presented here.[34, 35]

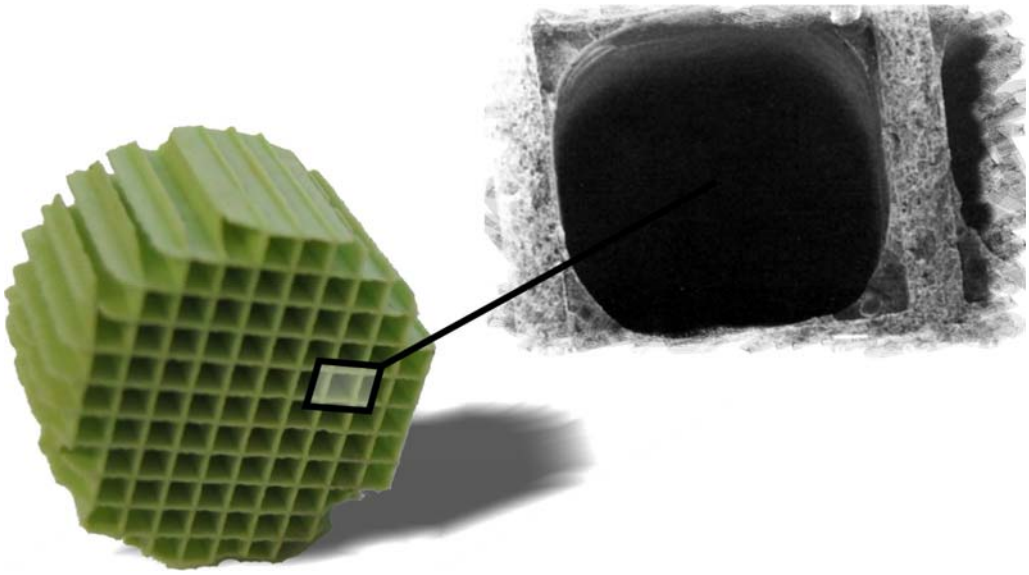

Figure 4.1: Monolithic structure coated with Ni before calcination and reduction. A closer look into the edges of one channel shows the washcoat. (Right picture taken from [28]).

4.1 Modelling Approach of Reactive Flows in Heterogeneous Systems

There is a wide variety of flow reactors, in which the reactive mixture passes trough tube-like devices. One class of those reactors are pipes with a diameter typically in the order of few centimetres up to metres. The flow field is turbulent in most cases, which also guarantees good mixing of the reactants. A fine resolution of the flow field details is rarely of interest, and, aside from that, computationally very expensive. Therefore, either averaged equations and turbulence models or the very simple plug flow models are used. Another class of tube-like reactors are monoliths or honeycombs, consisting of numerous passage-ways with diameters reaching from a tenth of a millimetre to a few millimetres. The flow field in these thin channels usually is laminar.

Monoliths are often used for catalytic reactions in technical systems and as well in this work. The catalytically active material is located either directly on the inner channel wall or dispersed in a washcoat. The monolith configuration, as shown in Figure 4.1, offers a number of advantageous features such as high surface-to-volume ratio combined with small pressure drop, support of even flow distribution, and easy passage of particulates in the gas stream as long as the diameter of the channel is greater than that of the particles.

A variety of physical and chemical processes occurs in a single channel of a monolith (Figure 4.2) and needs to be considered in the simulation. The transport of momentum, energy, and chemical species have to be considered not only in axial but also in radial direction. The chemical species can react either in the gas phase or on the inner channel

surface, which is coated with the catalyst. Diffusive processes, such as molecular diffusion in the gas-phase, product diffusion from the catalyst surface to the bulk of the gas, pore diffusion within the washcoat are important and can significantly affect the overall processes. The temperature distribution in the channel depends on convection, heat conduction in the gas phase and the solid channel wall, heat release by gas phase and surface reactions and thermal radiation. A detailed description of all transport processes would lead too far and only the processes and equations relevant for this work are explained. The interested reader may be referred to [38, 43, 66-68].

In our approach, we try to base the models of all these processes on the molecular level. Therefore, the 2- and 3- dimensional *Navier-Stokes* equations coupled with detailed transport and chemistry models are solved. Furthermore, the reactive flow in a single channel needs to be coupled with the overall heat transport in the solid structure.

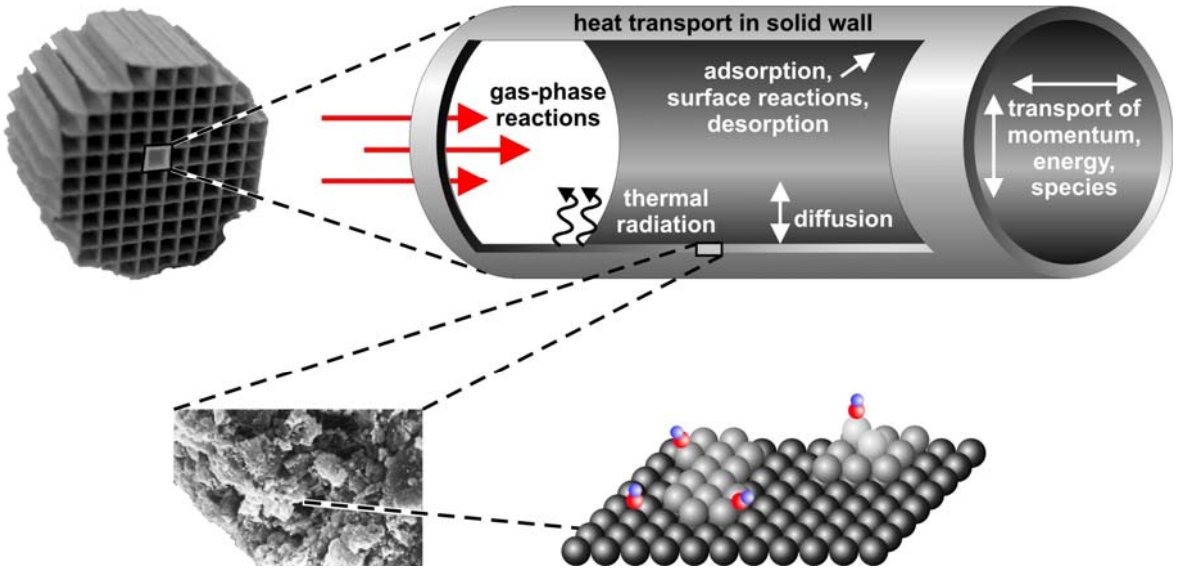

Figure 4.2: Scheme of processes, which can occur inside a single channel of a monolithic catalyst. The channel walls are covered with noble metal, e.g. Rh, Pt, and Pd. Here, surface reactions take place. Furthermore, gas-phase reactions and physical processes like diffusion, radiation, heat transport, and transport of momentum, energy, and species need to be considered.

4.2 Numerical Tool: DETCHEM Computer-Package

The mathematical models, which describe all these physical and chemical processes in a monolith are combined in a recently developed software-package DETCHEM by Deutschmann et al.[38] This program lined out in Figure 4.3 is built in a modular way providing interfaces for detailed transport and reaction models. The routines for calculating reaction rates and transport coefficients such as binary diffusion coefficients, thermal

conductivity, viscosity etc. forms the fundamental module of DETCHEM (library module). The library module interprets the chemical information conveyed by the detailed elementary reaction mechanisms, which are again the source of chemistry information for DETCHEM reactive flow models. The entire DETCHEM package is encompassed of a number of flow reactor models, such as CHANNEL, PLUG, and MONOLITH etc. These models are built on top of the library modules. The DETCHEM^{CHANNEL} solves the 2D *boundary-layer* equations, whereas the PLUG program incorporates a simpler one-dimensional transport model. These flow models are computationally inexpensive and can usually be solved within few seconds on a personal computer. These simpler models are frequently used.[69, 70] However when the solution of computationally expensive *Navier Stokes* equations for the description of chemically reacting laminar flow is necessary, DETCHEM can be coupled with the commercial CFD software FLUENT.

DETCHEM^{MONOLITH} can be used to simulate a complete monolithic structure. For systems, considered in this thesis, the reactants' residence time in the monolith is shorter than 100 ms. Therefore, it can be assumed that the time scales of the reactive flow and the solids' thermal response are decoupled. Thus, time variations in the local monolith temperature can be neglected when calculating the fluid flow through single channels at a given time. Therefore, a time-independent formulation is used to describe the gaseous flow, while a transient heat conduction equation for the solid is solved.[71]

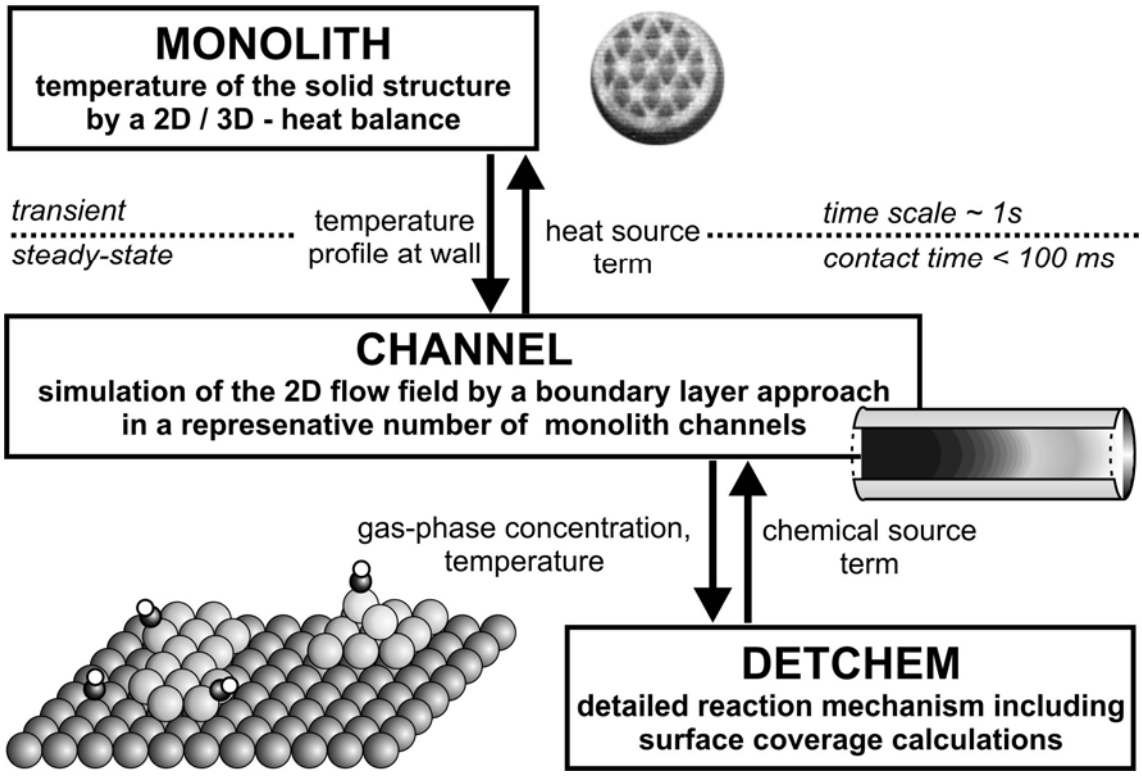

Figure 4.3: Structure of the applied models in the computer-package DETCHEM

4.2.1 Reaction Mechanism on the Surface (DETCHEM)

Surface and gas-phase reaction source terms ($j_{i,\mathrm{surf}}$, $\dot{\omega}_i$) are modelled by elementary-step based reaction mechanisms using the corresponding module of the DETCHEM program package.[34, 72] Heterogeneous reaction mechanisms include adsorption, desorption of molecules, dissociation and formation of reactants and products. In the model approach, it is assumed that the adsorbed species are randomly distributed on the surface and that one can average over local inhomogenities. Then a rate law of the heterogeneous reactions can be written similar to the usual gas phase kinetics. The reaction rate $\dot{s}_i$ is described by

$$\dot{s}_i = \sum_{k=1}^{K_\mathrm{s}} \nu_{ik} k_{\mathrm{f}k} \prod_{j=1}^{N_\mathrm{g}+N_\mathrm{s}} c_j^{\nu'_{jk}} \quad , \tag{4.1}$$

with K_s = number of heterogeneous reactions, $N_\mathrm{g}/N_\mathrm{s}$ = number of gas-phase/surface species, ν = stoichiometric coefficients, and the rate coefficient

$$k_{\mathrm{f}k} = A_k T^{\beta_k} \exp\left[\frac{-E_{ak}}{RT}\right] f_k(\Theta_1,...,\Theta_{N_\mathrm{s}}) \quad . \tag{4.2}$$

Since all the binding states of adsorption vary with the surface coverage of all species, the rate expression becomes rather complex. This coverage dependence of the rate coefficient is taken into account by an additional factor f_k to the *Arrhenius* like expression:

$$f_k(\Theta_1,...,\Theta_{N_\mathrm{s}}) = \prod_{i=1}^{N_\mathrm{s}} \Theta_i^{\mu_{ik}} \exp\left[\frac{\varepsilon_{ik}\Theta_i}{RT}\right] \quad . \tag{4.3}$$

The model of the catalytic reactions on the inner channel wall accounts for a varying surface coverage of adsorbed species along the channel, which is given by

$$\Theta_i = \frac{c_i \sigma_i}{\Gamma} \quad , \tag{4.4}$$

with Θ_i = coverage of species i, c_i = concentration of species i on the surface, in, e.g., mol m^{-2}, σ_i = number of occupied adsorption sites by species i, and Γ = surface site density, i.e., the number of adsorption sites per catalytically active surface area, given in, e.g., mol m^{-2}.

The challenge for the development of multi-step surface and reaction mechanisms is not only the elucidation of the reaction pathways but also the estimation of kinetic parameters. The gas-phase and surface-reaction mechanisms applied in this work are listed in Appendix A.

4.2.2 Simulation of the 2D-Flow Field (DETCHEM^{CHANNEL})

The gas phase concentrations and the temperature at the catalyst walls of the monolith channels are simulated by the program DETCHEM^{CHANNEL} using the source terms provided by DETCHEM library module. It calculates the 2D flow field by a boundary layer approach for a representative number of monolith channels.

Despite the actual 3D triangular or square shape of the used monolith channels, a 2D cylindrical channel model was applied. Given the inlet (velocity, temperature, species mass fractions) and boundary conditions (axial profile of the wall temperature), the two-dimensional flow field of the fluid can be calculated. Furthermore, the short contact time of the experiments also correspond in a high axial flow velocity. The diffusive transport in the same direction diminishes in comparison with the one perpendicular to the surface. This effect becomes more significant as the axial gas velocity is increased, i.e. for higher Reynolds numbers as long as the flow is laminar. The results achieved by the boundary-layer model can be as accurate as the results from the full *Navier-Stokes* model at high but laminar flow rates.[69] Mathematically, the character of the equations is simplified from elliptical to parabolic with a time-like coordinate along the channel axis. The set of equations in DETCHEM^{CHANNEL} consists of conservation equations for:

total mass

$$\frac{\partial(r\rho u)}{\partial z}+\frac{\partial(r\rho v)}{\partial r}=0 \tag{4.5}$$

with density ρ, radius r, channel length z, and velocities u and v,

mass of species i

$$\frac{\partial(r\rho u Y_i)}{\partial z}+\frac{\partial(r\rho v Y_i)}{\partial r}=-\frac{\partial}{\partial r}(rj_i)+rM_i\dot{\omega}_i \tag{4.6}$$

Y_i is the mass fraction of species i,

axial momentum

$$\frac{\partial(r\rho u u)}{\partial z}+\frac{\partial(r\rho v u)}{\partial r}=-r\frac{\partial p}{\partial z}+\frac{\partial}{\partial r}\left(\mu r\frac{\partial u}{\partial r}\right), \tag{4.7}$$

and enthalpy

$$\frac{\partial(r\rho u h)}{\partial z}+\frac{\partial(r\rho v h)}{\partial r}=r u\frac{\partial p}{\partial z}+\frac{\partial}{\partial r}\left(\lambda r\frac{\partial T}{\partial r}\right)-\frac{\partial}{\partial r}\left(\sum_i r j_i h_i\right) . \qquad (4.8)$$

The transport coefficients for radial diffusion (μ, λ) and the species diffusion fluxes j_i depend on temperature T and species composition, h is the enthalpy, and h_i the specific enthalpy.

Catalytic reactions at the surface are taken into account in terms of a diffusive surface flux $j_{i,\mathrm{surf}}$ in Eq. (4.8) at the boundary by

$$j_{i,\mathrm{surf}}=F_{\mathrm{cat/geo}}\cdot M_i\dot{s}_i \qquad (4.9)$$

Here, M_i = molar mass of species i, $F_{\mathrm{cat/geo}}$ is the ratio of catalytically active surface area to geometrical surface area of the channel.

With the given inlet conditions, the boundary-layer equations are solved in a single sweep of integration along the axial direction by a method-of-lines procedure in DETCHEM$^{\mathrm{CHANNEL}}$. The radial derivatives are discretized by a finite-volume method. The resulting differential-algebraic equation system is integrated using the semi-implicit extrapolation solver LIMEX.[73]

4.2.3 Temperature Distribution of the Catalyst (DETCHEM$^{\mathrm{MONOLITH}}$)

DETCHEM$^{\mathrm{CHANNEL}}$ can be coupled to the simulation of the temperature distribution in the solid structure of the monolith. This is achieved by solving a transient 2D or 3D heat balance depending on the shape of the monolith. Since the time-scale of the temperature variation of the monolith is much larger, in the order of seconds, than the short contact time of the reactive mixture, which is in the order of milliseconds, these time scales can be decoupled.

At each time step, a representative number of channels is simulated under quasi-steady-state conditions. These simulations provide the heat source term for the heat balance of the solid structure. For the calculation of the temperature of the solid structure, the catalytic monolith is treated as continuum and discretized as depicted in Figure 4.4.

The thermal behaviour of the monolithic structure is simulated by the computer code DETCHEM$^{\mathrm{MONOLITH}}$,[34, 72] applying the model of a two- or three-dimensional temperature equation:

$$\rho c_p \frac{\partial T}{\partial t} = \nabla(\lambda \nabla T) + q \quad . \tag{4.10}$$

The material properties (density ρ, heat capacity c_p and thermal conductivity λ) are functions of the material (monolith support or insulation). Heat losses due to conduction, convection, and thermal radiation at the exterior walls of the monolith can also be included.

The monolith and the channel calculations are coupled by the heat source term q in the temperature equation.

$$q = -\sigma \cdot 2\pi r \, \lambda \left. \frac{\partial T_{\text{gas}}}{\partial r} \right|_{\text{surf}} \quad . \tag{4.11}$$

σ = channel density

Therefore, each axial temperature profile is applied as a boundary condition for a channel calculation describing the heat flux from the gas phase into the monolith due to convection and chemical heat release. Since the channel calculation is the most time consuming step, only a representative number of channels is calculated explicitly.

For the spatial discretisation of the transient temperature equation, a finite volume approach is used. Either the LIMEX [73] or LSODE [74] solver can be chosen for the integration of the resulting ordinary differential equation system. Based on these models, the computational tool predicts the transient, two-dimensional distributions of temperature and species concentrations.

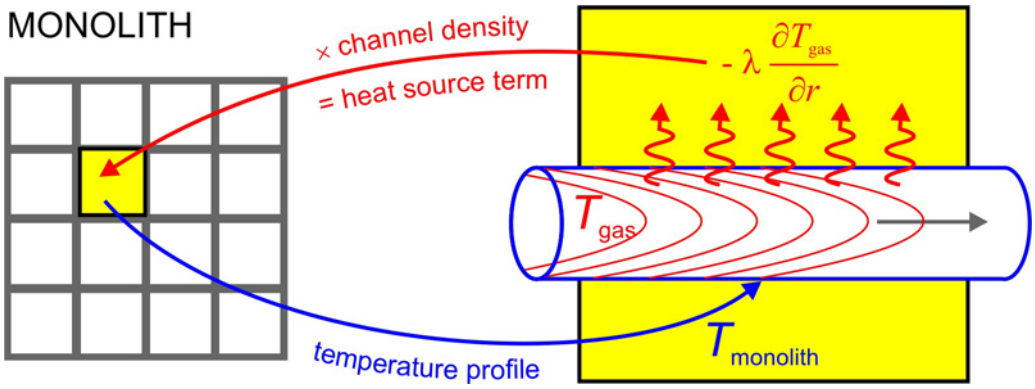

Figure 4.4: Schematic of coupling between the modules CHANNEL and MONOLITH.

CHAPTER V

5 Catalytic Combustion of Methane

Catalytic combustion research currently focuses on reactor design, increase in efficiency, and the search for more suitable catalysts. Thus, there is an urgent need for a better understanding of the physical and chemical processes occurring on the catalytic surface and their coupling with the surrounding flow field. In particular, it is important to understand the ignition and extinction behaviour of the oxidation of hydrocarbons. During the last decade, detailed catalytic combustion models have been designed [30-33] including multi-step heterogeneous surface-reaction mechanisms which may provide guidelines for a better understanding and for the optimisation of catalytic combustion.

In the first part of this chapter, the transient behaviour of the ignition process of the catalysed oxidation of methane is studied experimentally and numerically in a catalytically active honeycomb monolith. The experimentally determined and numerically predicted ignition temperatures as well as time-varying monolith exit temperatures, and fuel conversion during ignition are compared for varying CH_4/O_2-ratios.

The second part focuses on hydrogen-assisted ignition of the catalytic combustion of methane followed by an experimental study of the interaction between homogeneous and heterogeneous combustion.

The last section elaborates on a different transient phenomenon: Oscillatory PdO and Pd formation during methane combustion.

5.1 Light-off of Catalytic Combustion of Methane

Catalysed combustion can be defined as the complete oxidation of a combustible compound on the surface of a catalyst. While conventional combustion occurs in the presence of a flame, whereas catalysed combustion is a flameless process occurring at lower temperatures and, therefore, emitting less nitrogen oxides.[28] Furthermore, catalysed combustion offers fewer constraints concerning flammability limits and reactor design. These advantages of catalysed combustion determine its potential applications.[75]

Present combustor configurations are based on multiple-stage combustion, mostly including a homogeneous combustion stage. The design of the catalytic combustion stage typically calls for monolith systems that offer high surface area but low-pressure drop. The monolith honeycombs are often made of cordierite coated with catalytically active material, whereby a washcoat, mostly alumina, is frequently used to enlarge the surface area.

5.1.1 Experimental Conditions

The catalysed combustion experiments are carried out in the flow reactor depicted in Figure 3.1. In this case, a tubular quartz reactor with a span diameter of 2.6 cm is used. A 10 mm long honeycomb cordierite monolith with a diameter of 24 mm is employed as catalyst. The monolith is composed of about 230 rectangular channels with a cross-section of 1 mm^2 (the wall is not considered).

The monolith is coated with a 3%-wt. washcoat consisting of alumina (DISPERSAL, CONDEA Chemie GmbH) and the noble metal platinum as described in chapter 3.2. Energy dispersive X-ray spectroscopy (EDX) measurements showed that no chlorine compounds were left on the catalyst surface after the impregnation process.

The reactor is operated at atmospheric pressure. Ar and O_2 are fed into the reactor with constant flow rates of 5.43 standard litre per minute (slpm) and 1.36 slpm respectively, resulting in a flow velocity of 0.25 m s^{-1}. Due to the reduced cross-section in the catalytic monolith, the velocity at the channel entrance was 0.416 m s^{-1}, corresponding to a residence time of about 15 ms. To this flowing mixture CH_4 was added in a range between 1 vol.-% and 4 vol.-%. The exit temperature is monitored as a function of time, and a QMS is used to investigate the variation of the product composition. Argon is used instead of nitrogen to allow the determination of CO.

5.1.2 Numerical Model

Table 2: Material properties of the catalytic monolith and the insulation used in simulation

Physical properties	Catalytic monolith	Insulation
axial heat conduction λ_{ax}	2.5 W (m K)$^{-1}$	1.36 W (m K)$^{-1}$
radial heat conduction λ_{rad}	1.5 W (m K)$^{-1}$	1.36 W (m K)$^{-1}$
density ρ	2100 kg m^{-3}	2202 kg m^{-3}
heat capacity c_p	850 J (kg K)$^{-1}$	730 J (kg K)$^{-1}$
surface scaling factor $F_{cat/geo}$	20	
catalyst length [mm]	10	
catalyst diameter [mm]	25	
number of channels / shape	230 / square	
channel cross-section [mm^2]	1.13	
Corresponding radius [m]	5.641 10^{-4}	
radiation shield	uncoated cordierite	

Despite the actual square shape of the monolith channels, a cylindrical channel model is applied, due to the presence of washcoat with varying thickness. A mean channel diameter (0.564 mm) is assumed guaranteeing a uniform total mass flow through each channel. Table 2 displays the material properties of the catalyst and insulation.

Since the channel calculation is the most time consuming step, which, only a certain number of representative channels is calculated explicitly by choosing their radial positions or by grouping together channels with similar wall temperature profiles and inlet conditions. In the presented simulation three channels have been chosen at fixed positions (centre, wall, and at a position of 60% of the monolith's radius) using the same inlet conditions for all channels. The heat source terms are interpolated linearly with respect to the spatial coordinate.

The chemical reactions on the platinum surface are modelled using 27 irreversible elementary chemical reactions among 9 gas phase species and 11 surface species (see Table 10, Appendix A).[33, 39] The increase in the catalytically active surface area by the washcoat is taken into account by an estimated surface-enlargement factor of $F_{cat/geo} = 20$.

In order to estimate the potential influence of gas-phase reactions on the methane oxidation, single channel calculations using additional 14 gas-phase species and 168 gas-phase reactions were performed. The homogeneous reaction scheme is based on a reduction of a large set of hydrocarbon oxidation reactions to C_1 species.[76] However, for temperatures below 1200 K no significant influence on the conversion is observed. Hence,

the presented simulations are performed using only surface reactions. The simulations of this chapter were carried out by S. Tischer[3] with DETCHEM version 1.4.2.[35, 39]

5.1.3 Results and Discussion

a) Temperature Dependency on the CH_4/O_2 Ratio in a Honeycomb Monolith

In order to determine the ignition temperature of the catalysed oxidation of methane, a mixture of methane and oxygen diluted with argon flew through a platinum-coated honeycomb monolith at atmospheric pressure. The gas mixture entered the reactor at room temperature and a furnace heated the catalyst (5 K min^{-1}) until ignition. Then, the furnace was turned off. At the ignition temperature, $T_{ignition}$, the catalyst temperature rose rapidly caused by exothermic surface reactions. After about two minutes, a new steady state controlled by mass transport of reactants towards and products away from the catalyst was reached.

Figure 5.1a) depicts the ignition temperature, the maximum temperature inside and outside the reactor reached during the reaction, and the adiabatic temperature. In agreement with previous stagnation-flow experiments and simulations [32, 33] the ignition temperature decreases with increasing CH_4/O_2-ratio in the monolith. Before ignition, the surface is primarily covered with oxygen, because the sticking probability of oxygen is higher than that of methane. With increasing surface temperature a point will be reached where the adsorption/desorption equilibrium of oxygen shifts to desorption. This results in bare surface sites where CH_4 can be adsorbed, followed by H abstraction, which leads to adsorbed C(s) and H(s) atoms reacting with the surrounding O atoms to CO(s) and OH(s) immediately.

Both molecules quickly form CO_2 and H_2O, which desorb leaving more free surface sites for CH_4-adsorption. For CH_4/O_2-ratios below 0.1 (2 vol.-% CH_4) the reaction is extinguished in a couple of minutes if the external heating is turned off. In these cases, the ignition temperature was above the calculated adiabatic temperature.

Using the difference between the wall temperature outside the quartz tube and the gas temperature at the exit of the catalytic monolith, the exterior heat loss coefficient for the subsequent simulation was estimated to be 40 W (m^2 K)$^{-1}$.

[3] Dr. Steffen Tischer, University of Karlsruhe, Institute for Chemical Technology and Polymer Chemistry

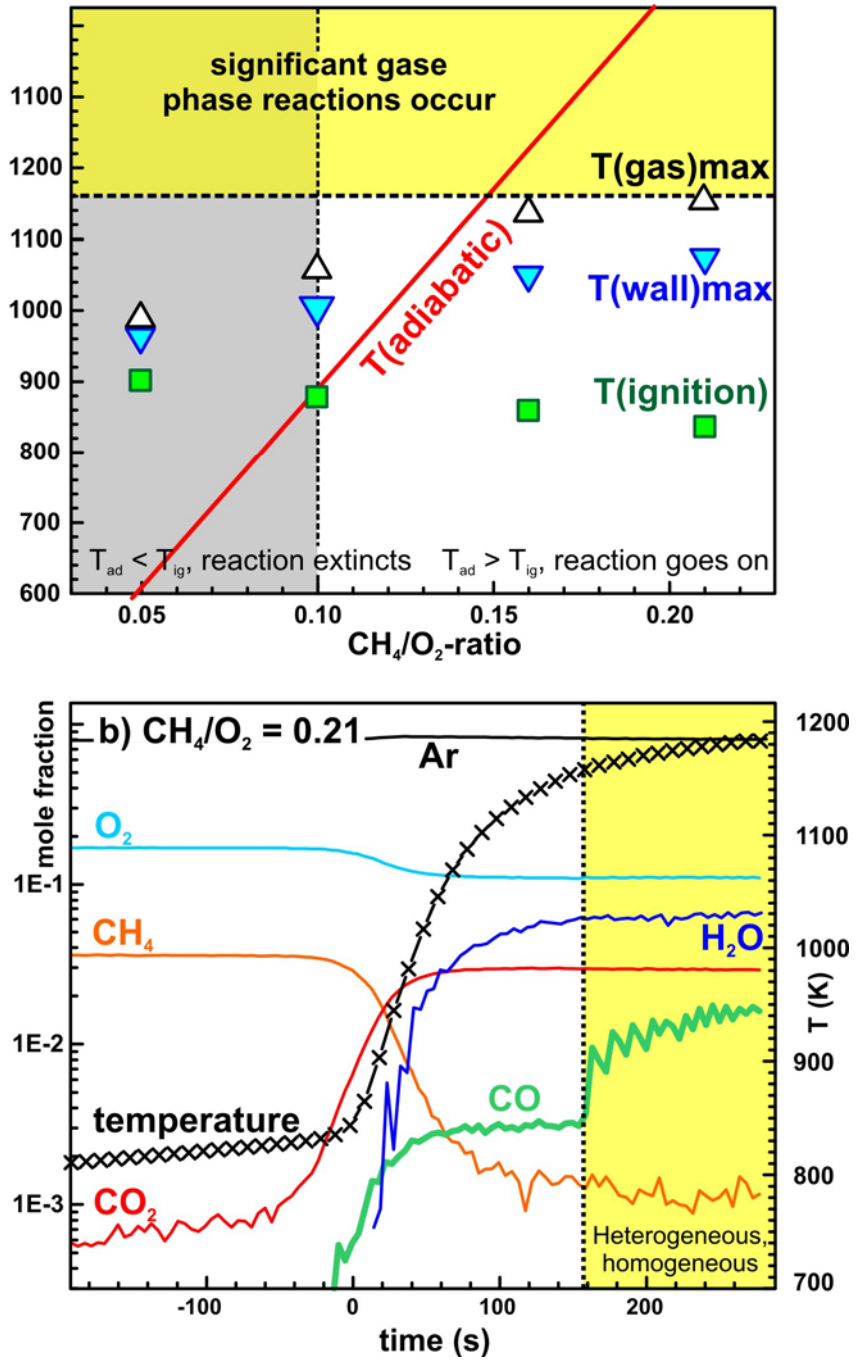

Figure 5.1: a) Temperature diagram of ignition processes for CH_4/O_2-ratios: 0.05 (1.0 vol.-% CH_4), 0.10 (2.0 vol.-% CH_4), 0.16 (3.1 vol.-% CH_4), and 0.21 (4 vol.-% CH_4). With a methane feed exceeding 4 vol.-% gas-phase reactions of CH_4 occur immediately. The solid line represents the adiabatic temperature, squares stand for the ignition temperature, up triangles for the maximum temperature in the gas phase at the exit of the catalytic monolith and the down triangles for the temperature outside the quartz tube. b) Mass spectrum of CH_4/O_2 ratio of 0.21 and exit gas-phase temperature during ignition. At a temperature around 1150 K gas-phase reaction indicated by CO formation become significant (not shown).

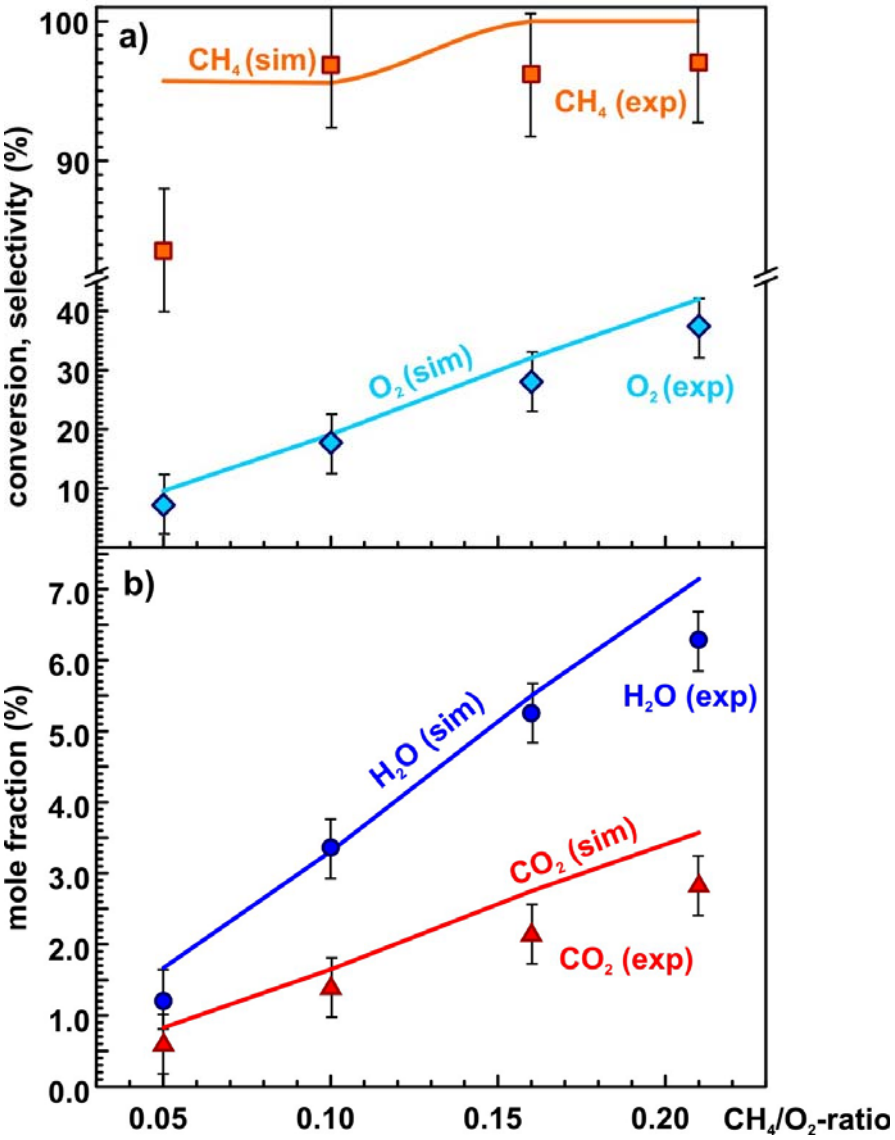

Figure 5.2: Steady-state conditions. Symbols represent experimental data, lines the simulation. a) The conversion of CH_4-, O_2 as a function of the CH_4/O_2-ratio. b) Molar fraction of CO_2, and H_2O at the catalyst exit.

b) Steady-State Simulations of the Catalytic Combustion Monolith

Using the numerical tool DETCHEM^{MONOLITH}, steady-state simulations of the ignited monolith were performed. In order to start the simulation, an arbitrary monolith temperature of 1050 K was chosen. This temperature guarantees ignition of the entering gas mixture. The inlet conditions (gas temperature, species composition, and velocity) were chosen according to the experiment. Taking heat release by chemical reactions and heat loss at the exterior wall into account, a steady-state temperature profile of the catalytic monolith is established.

Figure 5.2 shows a comparison between experiment and simulation of the CH_4 and O_2 conversions, CO_2 selectivity, and outlet mole fraction of H_2O, CO_2 and CO. However, for CH_4/O_2-ratios below 0.10 (2 vol.-% CH_4) the reaction extinguished in both the experiment and in the simulation. Simulation and experiment agree well in the case of steady state for CH_4/O_2-ratios between 0.10 and 0.21. With the assumption of absence of gas-phase reactions, no CO was formed in the simulation. In contrast to this, a very small amount of CO was detected in the experiment. This value for CO with a maximum of 0.35% corresponds to the fragmentation pattern of CO_2 in a QMS working with a ionisation energy of 40 eV and therefore cannot be attributed to CO formed in the reactor. For CH_4 feeds exceeding 4 vol.-% (CH_4/O_2-ratio greater than 0.21), gas-phase reactions become significant due to the high reaction temperature above 1200 K. Thus, simulations for CH_4/O_2-ratios exceeding 0.21 need to include gas-phase reactions. An experimental investigation of the interaction between homogeneous and catalytic combustion is discussed in chapter 5.3.

c) The Ignition Process

The results of numerical simulations of the ignition process for a CH_4/O_2-ratio of 0.16 are shown in Figure 5.3. Before ignition, the cold gas entering the catalyst cools the heated monolith. First, reactions commences in the outermost channels near the hot wall. The release of heat of reaction leads to an increase in the temperature further inside. Since a positive temperature-gradient is established along the channel walls, the reaction lights off at the exit of the catalytic channels. After 75 s, reactions also occur at the centre of the monolith, as can be seen by the exothermic production of CO_2 and H_2O (Figure 5.3b). This leads to a further temperature increase in the monolith. Hence, the point of ignition moves towards the inlet. Finally, the reaction starts immediately upon entering the catalytic monolith. At steady state, most heat is released within the first few millimetres. After 200 s, the conversion reaches steady state with complete consumption of CH_4.

d) Comparison of Transient Simulations and Experiment

The simulation of the exit gas-phase temperature is in good agreement with the experimental results (Figure 5.4a). The higher ignition temperature in the experiment (858 K) compared to the result of the simulation (769 K) is due to the temperature profile of the furnace. In contrast to the simulation, there is no sharp temperature step at the entrance of the catalytically active monolith, but a continuous increase in temperature leading to a pre-heating of the gas phase. To simulate the start-up of the reaction, a heating rate of 5 K min^{-1} was assumed, which was kept constant for the whole calculation, while in the experiment the furnace was turned off at the ignition point.

Figure 5.4b) displays the change of the mole fractions of the educts as a function of time. The simulation shows the expected dependence of the mole fraction of O_2 and CH_4. The small amount of CH_4 (0.1%) observed by the mass spectrometer after ignition may be due to a bypass in the sealing around the catalyst. Before ignition, the amount of both species is slightly lower in the simulation than in the experiment. This is due to some formation of CO_2 and H_2O predicted by the simulation (Figure 5.4) before ignition temperature is reached. In all experiments, the ignition was actually indicated by a slow rise of CO_2 about 30 s before light-off (Figure 5.1b).

Figure 5.4c) depicts the mole fractions of the products. In the experiment, there were no products observed before ignition at about 800 K. The numerically predicted quite high mole fractions of CO_2 and H_2O are the result of interpolation between the three simulated channels. The influence of the outmost channel, where the reactions start, is over-predicted. However, the more interesting part is the well-predicted ignition process. With proceeding ignition, the influence of the wall decreases and the choice of three channels is sufficient. As explained before, gas-phase reactions that were not predicted by the simulation led to minor concentrations of CO (ca. 0.2%).

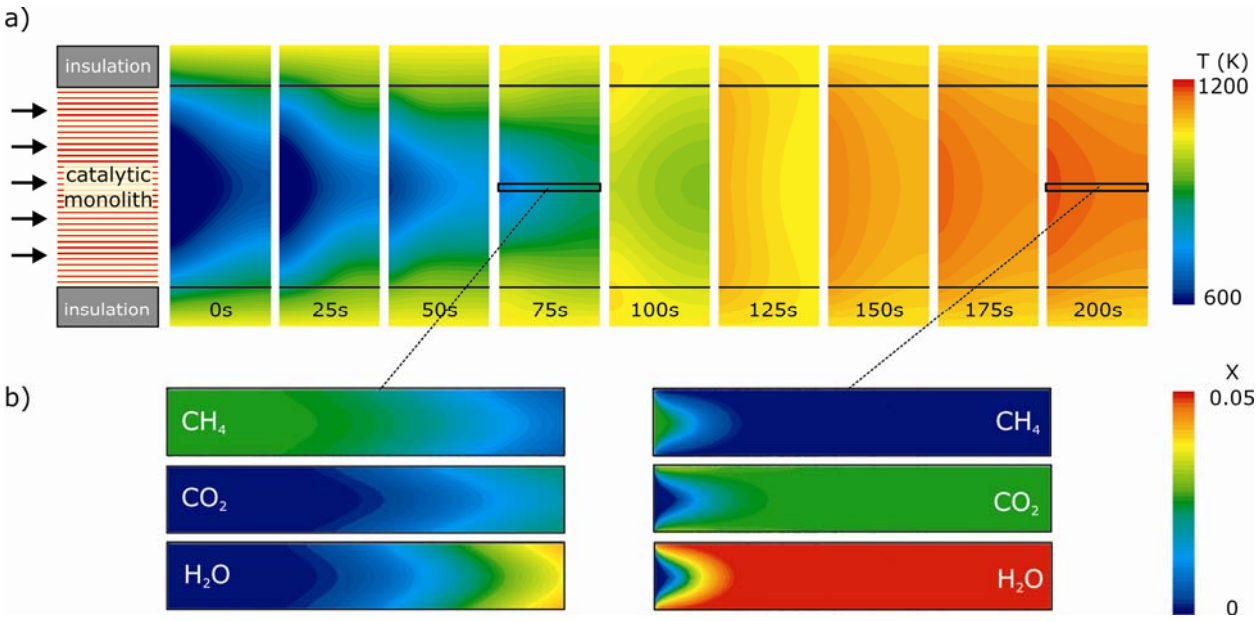

Figure 5.3: a) Time-dependent 2D temperature distribution in the catalytic monolith. The wall temperature increases by 5 K min^{-1}, while cold gas (17.14% O_2, 2.75% CH_4, 80.11% Ar, 298 K) enters the monolith. Ignition starts at 0 s. After 200 s, full conversion is reached. b) CH_4, CO_2, H_2O mole fractions inside a channel at the centre of the catalytic monolith at 75 s and at 200 s after ignition

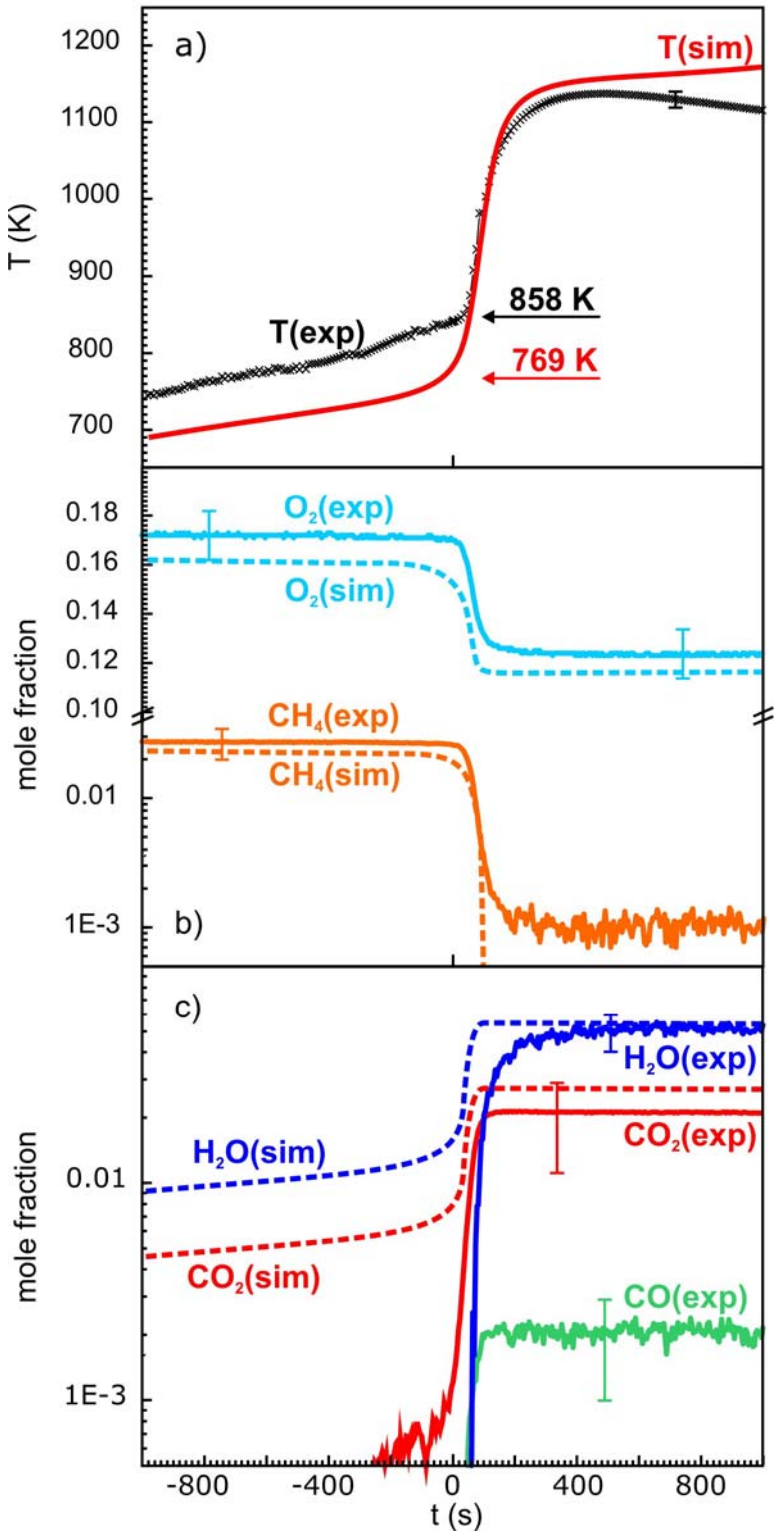

Figure 5.4: a) Transient temperature profiles during ignition for a CH_4/O_2-ratio of 0.16. Crosses represent the measured temperature at the exit of the catalytic monolith. The simulated gas-phase temperature is depicted by a solid line. b) O_2 and CH_4-conversion during the ignition process. Dashed lines depict the simulation, solid lines the experimental data. c) Mole fractions of H_2O, CO_2 and CO during ignition.

5.2 Hydrogen-Assisted Ignition on Platinum

Since the ignition of methane on Pt occurs at relatively high temperatures at lean conditions [33, 77], there is a major interest to find a way to reduce the light-off temperature, in particular for gas turbine applications where the catalytic combustion critically depends on the feasibility of a convenient light-off mechanism of the catalytic combustor. The addition of hydrogen to the initial mixture for example may help to reduce the ignition temperature, because the ignition of hydrogen on platinum occurs at room temperature. Deutschmann et al. [32] investigated the dependence of the hydrogen-assisted light-off of methane on platinum and on methane concentrations. They suggested that the light-off was primarily determined by the catalyst temperature that is a result of the heat release due to catalytic oxidation of hydrogen. Since the pathways of methane dissociation on platinum in presence of oxygen are rather complex hydrogen can have a major impact on the reaction kinetics, as well. To study the impact of H_2 addition on the kinetics of methane combustion an experimental numerical study was conducted.

5.2.1 Experimental Conditions

Two different kinds of experiments concerning the catalytic combustion of methane on platinum were carried out. In the first set of experiments, a furnace provided the heat needed for light-off, and in the second set, the combustion of hydrogen provided the required temperature.

In both cases, the reactor described in chapter 3.1 was used. A 3 wt.-% Pt coated cordierite monolith served as catalyst with a total diameter of 24 mm and 10 mm length. The monolith consisted of about 230 rectangular channels with 1 mm^2 cross-section. For increasing the catalytically active surface area, the honeycomb monolith was impregnated with 3 wt.-% alumina washcoat. To simulate the catalysed combustion of methane, a mixture of 20 vol.-% O_2 and 80 vol.-% Ar with a total flow rate of 6.785 slpm (0.25 m s^{-1}) was fed as basic flow in all cases. Ar was used instead of N_2 since a QMS was applied to determine the gas-phase composition and the signals for CO and N_2 cannot be separated due to identical molecular masses. CH_4 was added to this Ar/O_2 mixture yielding CH_4/O_2 ratios of 0.05, 0.10, 0.15 and 0.20 corresponding to 0.9 vol.-%, 1.9 vol.-%, 2.8 vol.-% and 3.7 vol.-% CH_4. The furnace was heated up slowly until ignition occurred and held on this temperature value.

In case of hydrogen-assisted ignition, no furnace heating was used and the light-off temperature was reached by H_2 combustion. 4.5 vol.-% (0.325 slpm), 4.7 vol.-% (0.436 slpm), 5 vol.-% (0.364 slpm), 5.2 vol.-% (0.379 slpm), or 6 vol.-% (0.436 slpm)H_2 was added to the basic mixture of O_2 and Ar. All the H_2 was consumed immediately at room temperature heating up the catalyst. The CH_4 flow was turned on as soon as no change of

temperature was observed. The methane flow was then increased in steps mentioned above until ignition occurred, indicated by a fast temperature rise and a rapid consumption of CH_4 and O_2. For H_2 concentrations below 4 vol.-% no ignition of the catalysed combustion of CH_4 could be observed. The corresponding flow rates and mole fractions are compiled in Table 3. The light-off temperatures, maximum temperatures, conversions of CH_4 and O_2, as well as the yield of CO_2 are depicted in Figure 5.5. To ensure that both sets of experiments are comparable the flow rates of Ar, O_2, and CH_4 were kept the same in both cases.

5.2.2 Parameters for Simulation

In order to interpret the experimentally derived data, it is useful to know the average coverage at certain temperatures, the surface coverage during the reaction along a single channel, and the chemical equilibrium for all inlet conditions. A single channel is simulated, which is assumed to be cylindrical. The radius equivalent to the cross section of the channel (1 mm^2) is $5.6420 \cdot 10^{-4}$ m. Taking into account the free cross section of the monolith, the velocity of 0.25 m s^{-1} at RT calculated for the total catalyst leads to an effective velocity of 0.524 m s^{-1} at the channel inlet. (The catalyst consists of 234 channels with an effective total cross section of 234 mm^2 compared to a cross section of 452.4 mm^2 of the whole structure.)

To get an idea about the different ignition behaviour with and without H_2, the surface coverage in an isothermal channel at 400 K, 500 K, 600 K, and 900 K is calculated for both cases using the DETCHEM^{CHANNEL} v 2.0 and compared to each other.[37] The detailed reaction mechanism [33] for the catalytic combustion of methane is listed in Table 10 Appendix A.

Table 3: Initial conditions, ignition and exit temperatures for all measurements

CH_4/O_2	Total flow [slpm]	Flow CH_4 [slpm]	Flow H_2[slpm]	X(Ar)	$X(O_2)$	$X(CH_4)$	$X(H_2)$	$T_{ignition}$ [K]	T_{exit} [K]
Without H_2									
0.05	6.8538	0.0679	0	0.7921	0.1980	0.0099	0	900.3	1003.5
0.10	6.9216	0.1357	0	0.7843	0.1961	0.0196	0	876.8	1058.5
0.16	6.9895	0.2036	0	0.7767	0.1942	0.0291	0	858.1	1137
0.21	7.0573	0.2714	0	0.7692	0.1923	0.0385	0	835.4	1183
With H_2									
0.05	7.2903	0.0679	0.4365	0.7446	0.1862	0.0093	0.0599	772.2	868.8
0.10	7.3009	0.1357	0.3793	0.7436	0.1859	0.0186	0.0520	771.1	1010.5
0.16	7.3535	0.2036	0.3640	0.7382	0.1846	0.0277	0.0495	763.1	1022.8
0.21	7.3965	0.2714	0.3392	0.7340	0.1835	0.0367	0.0459	756.7	1053.1
0.35	7.6538	0.5429	0.3250	0.7093	0.1773	0.0709	0.0425	724.6	1047.8

As a next step, the surface coverages and the chemical equilibrium at the exit temperatures were calculated for all initial conditions using DETCHEM^{EQUIL}. These values give hints on the different yields of CO_2 and CH_4 and the conversions of O_2. Table 3 shows the parameters for all experiments. The flow rate of the simulated air 6.5879 slpm was kept constant.

5.2.3 Results and Discussion

The addition of H_2 to the feed gas for the catalytic combustion of CH_4 on Pt has a huge impact on the reaction behaviour. A closer look at Figure 5.5 reveals that H_2 is very likely to contribute more than only heat for the ignition to the oxidation as assumed by Deutschmann et al.[32] Since H_2 removes O(s) from the surface by formation of H_2O, it is likely that H_2 has a great impact on the reaction kinetics of CH_4 combustion. Different ignition and maximum temperatures, conversions, and yields of CO_2 indeed indicate an important role of H_2 on the kinetics causing considerable differences between hydrogen-assisted and thermally initiated reaction as seen in this work.

In both cases, the light-off temperature decreases (see Figure 5.5b) with increasing CH_4/O_2 ratio. In the case of methane combustion without H_2, oxygen initially covers the surface.[78] Heating up the catalyst favours desorption in the adsorption/desorption equilibrium providing vacancies for CH_4. Methane decomposes immediately and reacts with the O forming CO_2 and H_2O generating heat, which further shifts the adsorption/desorption equilibrium towards the desorption of O_2. Therefore, more vacancies are generated accelerating the reaction. At fuel-richer conditions the concentration of methane molecules on the surface slowly increases causing the ignition temperature to decrease. One can also recognise this behaviour by calculating the surface coverage at different temperatures, depicted in Figure 5.6 (left part). At 400 K the surface mainly is covered with O(s) and hardly any Pt vacancies are left. Increasing the wall temperature (500 K) shows that now more CH_4 reaches the surface. This is due to a very small amount of C and CH formed by dissociation of CH_4, which is necessary for the combustion reaction.

At 600 K the first product formation is indicated by increasing amounts of CO and H_2O. Comparing ignition experiments of methane on Pt without H_2 addition with experiments of other groups [79] it can be seen that all measured temperatures at the same ratios fit the previous measurements perfectly. Although some groups used Pt foils and N_2 as diluent [77, 80], other groups Pt wires [81], or Pt coated monoliths and Ar dilution (this work), no effect of dilution or shape of catalysts was observed. However, it can be clearly seen that the addition of H_2 has a positive effect on the ignition temperature, which is more than 100 K lower than in case of common combustion. Here, not only CH_4 and O_2 compete for free vacancies but also H_2, which occupies the surface first. On a Pt catalyst, room temperature is sufficient to start exothermic H_2 combustion, which heats up the monolith.

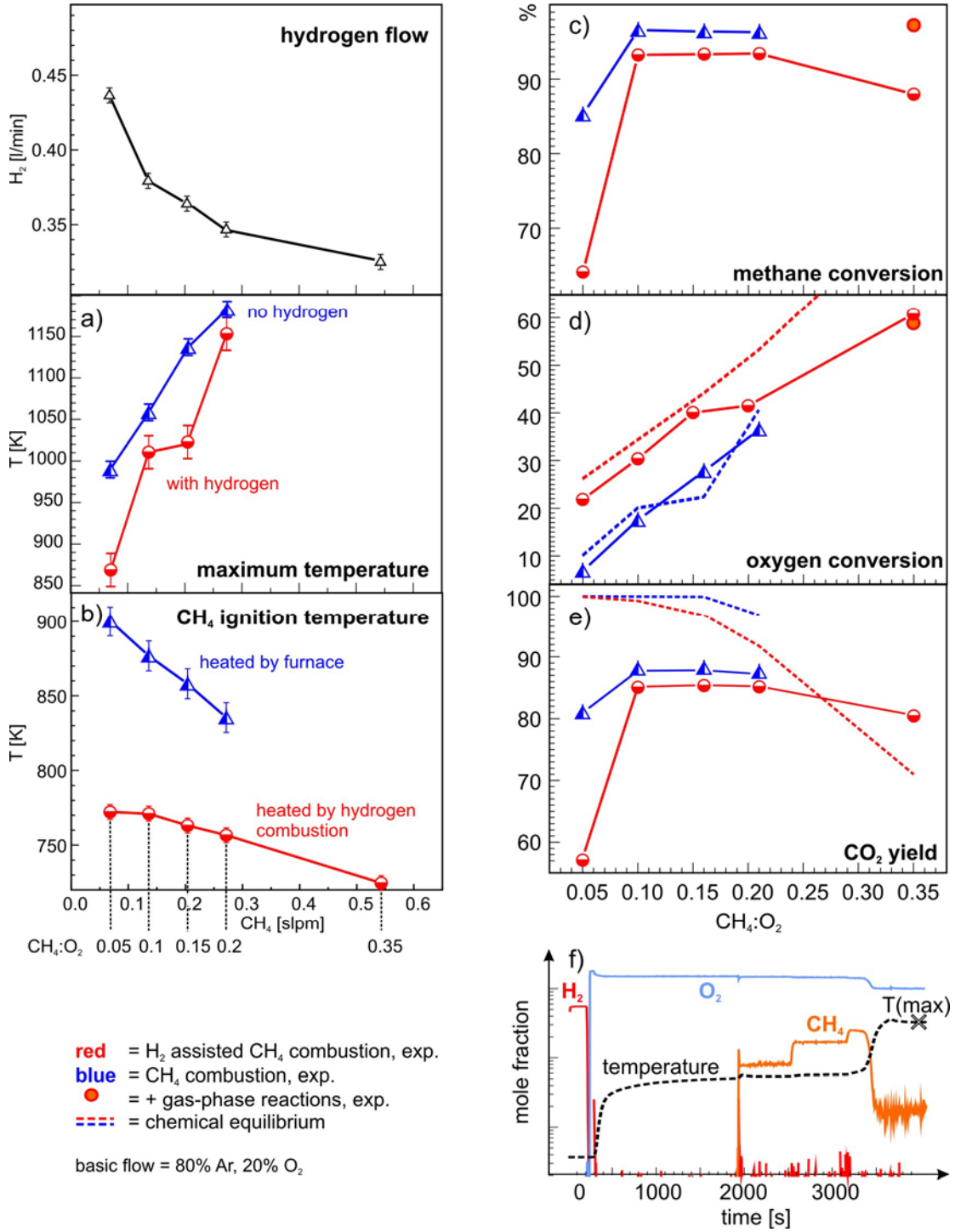

Figure 5.5: CH_4 combustion in simulated air (80 vol.-% Ar and 20 vol.-% O_2). In case of H_2-assisted ignition (red circles) 4.5 vol.-%, 4.7 vol.-%, 5 vol.-%, 5.2 vol.-% and 6 vol.-% H_2 is added. As H_2 was used to provide the heat, the furnace was turned off. Blue up-triangles represent reactions heated by a furnace without any H_2 addition. a) Maximum temperature during catalytic combustion of CH_4 on Pt at different CH_4 flow rates. b) Ignition temperatures. c) CH_4 conversion. d) O_2 conversion. e) CO_2 yield. At a CH_4/O_2 ratio of 0.35 significant gas-phase reactions took place before steady state could be reached. The dashed lines: Values of the chemical equilibrium at the exit temperature. The error bars of about 10% are neglected in c-d) for a better view. f) shows an exemplary H_2-assisted ignition. As soon as H_2 and O_2 flow through the catalyst, H_2 is converted increasing the temperature. CH_4 is turned on and causes again a temperature increase, when the reaction starts.

The added H_2 occupying the surface first under dissociation, reacts with the adsorbed O(s). The produced water leaves the surface continuously generating vacancies, which methane can occupy, too. Figure 5.6 (right side) shows that the coverage of the surface is completely different, if H_2 is added. At 400 K already a huge amount of CO is formed, the surface is mostly covered by carbon, and CH and CH_2 can be found on the surface (not shown), too. Compared to the catalytic combustion without H_2, the number of free adsorption sites on Pt is increased by a factor of about 1000. Nevertheless, the applied mechanism (Table 10, Appendix A) seems not to be perfect to simulate H_2-assisted catalytic combustion, because the carbon coverage, C(s), even at room temperature (not shown) seems over predicted.

The higher maximum temperature (blue symbols in Figure 5.5 a)) of the classical catalytic combustion compared to the H_2-assisted reaction (red) could be due to higher exothermic methane conversion as illustrated in c). To explain this phenomenon it is necessary to have a look at the surface kinetics. In case of H_2 addition water will be formed immediately by oxidation of H_2. Therefore, a certain amount of the surface area is always occupied by H_2O(s). This can be seen clearly by comparing these results with the surface coverage calculations in Figure 5.6 at 900 K, where with H_2 more surface sites are occupied by OH and H_2O than in absence of H_2. The adsorption of CH_4, dissociation as well as the reaction to CO and CO_2 respectively have to happen on the remaining vacancies downstream of the monolith. Since the high flow rate (0.25 m s^{-1}) and the short length of the catalyst (10 mm) result even for these lean mixtures in a very short contact time of some milliseconds CH_4 breakthrough occurs. Comparing the total flow rates of both measurement rows indicates that an effect of heat loss by convection out of the system and a different CH_4 conversion as a consequence can be neglected. The flow rate changes only in the H_2-assisted combustion since for each CH_4/O_2 ratio a different H_2 flow is added. Therefore, the total flow rate is in the same shape of the H_2 addition sketched in Figure 5.5 b) (black triangles).

The equilibrium calculations - as depicted in Figure 5.5 d) dashed lines - show that in case of H_2 addition to the combustion gas more O_2 (in the order of 20%) should be converted; the experimental results support the calculation. Additionally, the trend of increasing conversion of O_2 with increasing CH_4/O_2 ratio is observed, too. The reduced yield of CO_2 in case of addition of H_2 to the combustion gas compared to the conventional combustion can be explained with the equilibrium calculations, as well. Due to the higher concentrations of reducing agents (CH_4 and H_2) in presence of H_2, more reduced species will be observed as reaction products. In this case more CO is formed. However, not only H_2 is responsible for enhanced formation of CO, but also the higher temperatures. With increasing temperatures, the $CO + ½\ O_2 \rightleftharpoons CO_2$ equilibrium favours the formation of CO.

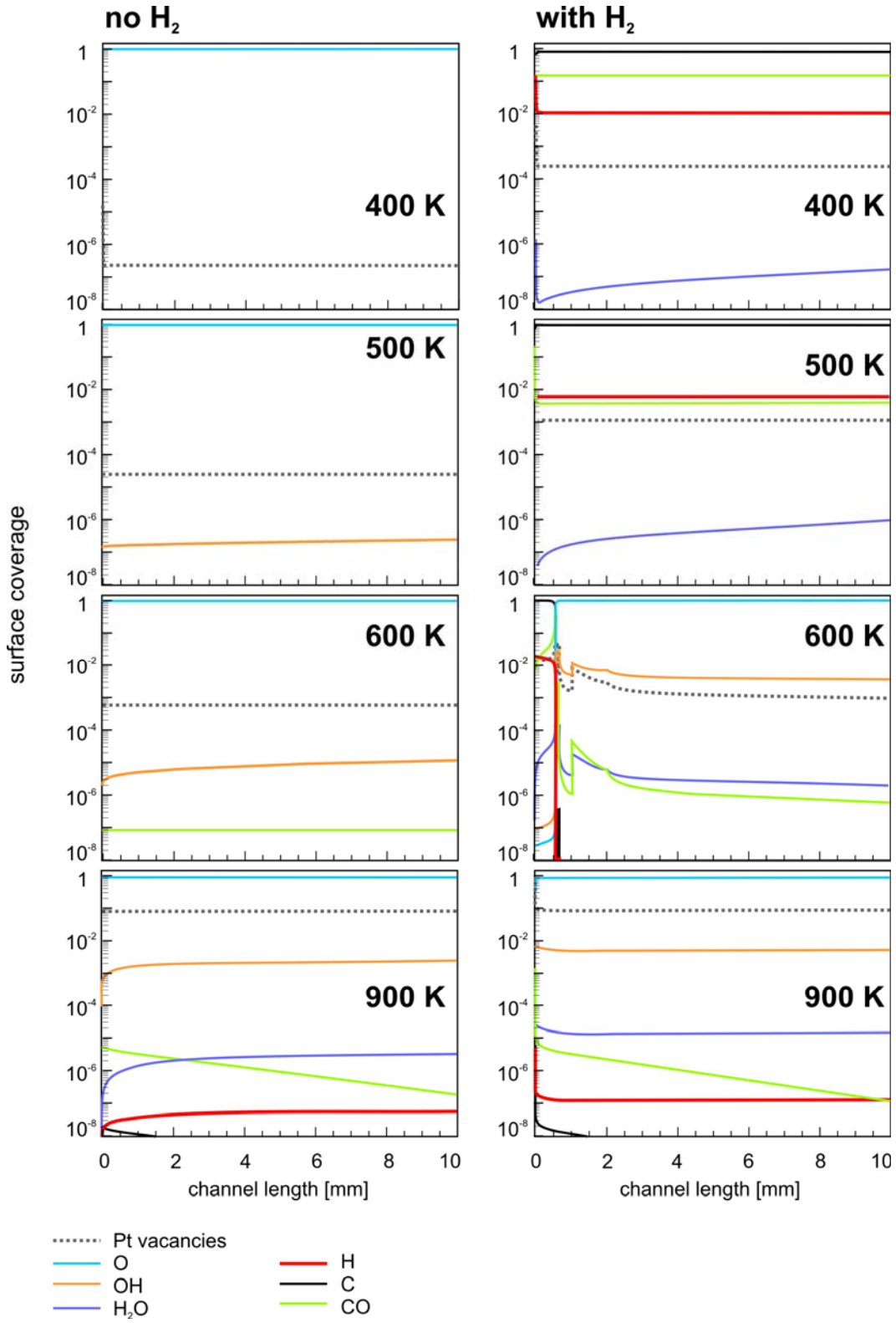

Figure 5.6: Calculation of the surface coverage along a single channel at isothermal conditions for O_2/CH_4 ratios of 0.05 to 0.35. Left part: the feed gas consists of Ar, O_2, and CH_4; right hand side: H_2 is added. The coverage of the surface is completely different, if H_2 is added: At 400 K a huge amount of CO is formed, the surface is mostly covered by carbon. Compared to the catalytic combustion without H_2, the number of free adsorption sites on Pt is increased by a factor of about 1000. Therefore, the ignition temperature decreases due to H_2 addition.

In both cases gas-phase reactions occurred at a critical CH_4/O_2 ratio. For pure combustion of methane, they started at a CH_4/O_2 ratio exceeding 0.2 and in case of the H_2-assisted combustion at a ratio of 0.35. The gas-phase reactions were indicated by a sudden rise of the concentration of CO and temperature. For safety reasons the reaction was stopped immediately. Therefore, the last values at a CH_4/O_2 ratio of 0.35 in Figure 5.5 are not in the trend since the steady state was not reached. Apart from gas-phase reaction caused by the high temperature, oscillatory gas-phase reactions were observed. They were indicated by a clicking noise and a sudden rise of the concentration of CO accompanied by a temperature increase in some degrees and will be discussed in chapter 5.3.

In summary, the addition of H_2 to catalytic combustion processes on Pt is a promising way to improve the reaction control. Less energy is needed to initiate the reaction since the ignition temperature is very low compared to the conventional way. The most important advantage, though, is the lower ignition temperature reached during the combustion. Furthermore, a lower maximum temperature is reached. This does not only spare the catalyst but also the reactor material. Instead of pure H_2, a part of the fuel could be partially oxidised forming syngas, which is then fed to the combustion mixture. However, the interactions between catalytic and gas-phase reactions are not completely understood yet and need some more experimental and in particular numerical investigations since sudden unexpected gas-phase reaction easily can lead to explosions. Furthermore, the mechanistic explanation for catalytic combustion of methane needs to be enhanced, because the influence of H_2 combustion on CH_4 desorption does not fit perfectly. It is known from the literature that Oxygen-assisted pathways (e.g. $CH_3(s) + O(s) \rightarrow CH_2(s) + OH(s)$, 84.6 kJ mol^{-1}) may play a dominant role in the dissociation of CH_4, the pyrolytic pathways ($CH_3(s) + Pt(s) \rightarrow CH_2(s) + H(s)$, 108.0 kJ mol^{-1}) have a minor impact due to the considerable difference in energy of activation.[79] However, the oxygen-assisted pathways are not listed in our Pt mechanism.

5.3 Oscillatory Interactions between Gas-Phase and Surface Reactions at High Temperatures

During the investigation of the catalytic oxidation of methane on Pt (chapter 5.1) and the hydrogen-assisted ignition (chapter 5.2) gas-phase reactions accompanied the heterogeneous reactions at certain combinations of temperature, methane, and hydrogen flows. They were always indicated by a “clicking” noise followed by a peak for CO. As an example, Figure 5.7 shows the mass spectrum during catalytic combustion, where 436 ml min^{-1} H_2 and 135.7 ml min^{-1} CH_4 fed to a simulated air mixture (80 vol.-% Ar and 20 vol.-% O_2) of 6.7859 slpm. The conversion of CH_4 is complete; by catalytic combustion, exclusively CO_2 and H_2O are formed. Since gas-phase reactions provide more heat, CO is formed as well.

This oscillatory behaviour of gas-phase reactions depends on the inlet conditions and the temperature. For instance with H_2 addition these clicks occurred at lower temperatures (~950 K exit gas-phase temperature) than in case of plain CH_4 combustion (~1150 K).

5.3.1 Experimental Conditions

For a better understanding of the interactions between gas-phase and surface reactions experimental conditions were chosen under which oscillatory behaviour was expected according to previous experiments. The same reactor and Pt catalyst as described in chapters 5.1 and 5.2 were used. Here again 20 vol.-% O_2 and 80 vol.-% Ar with a total flow rate of 6.785 slpm (0.25 m s^{-1}) were used and 5 vol.-% H_2 (364 ml min^{-1}) was added to provide the heat for ignition. All the H_2 was consumed immediately at room temperature heating up the catalyst. When a constant temperature was reached CH_4 was turned on with a flow rate of 271.4 ml min^{-1} (corresponding to $CH_4/O_2 = 0.2$ or 3.2 vol.-% of the total gas flow). Only catalytic combustion occurred with this feed. Then the CH_4 flow was increased until the CH_4/O_2 ratio corresponded to 0.30 (4.8 vol.-% CH_4 results in 356.3 ml min^{-1}), with this feed, oscillatory reactions in the gas-phase were observed. The left part of Figure 5.8 displays a cut-out of the mass spectrum taken while the CH_4/O_2 ratio changed from 0.27 to 0.30. The right hand side displays oscillatory behaviour of gas-phase reactions represented by the mole fractions, especially those of CO and CO_2.

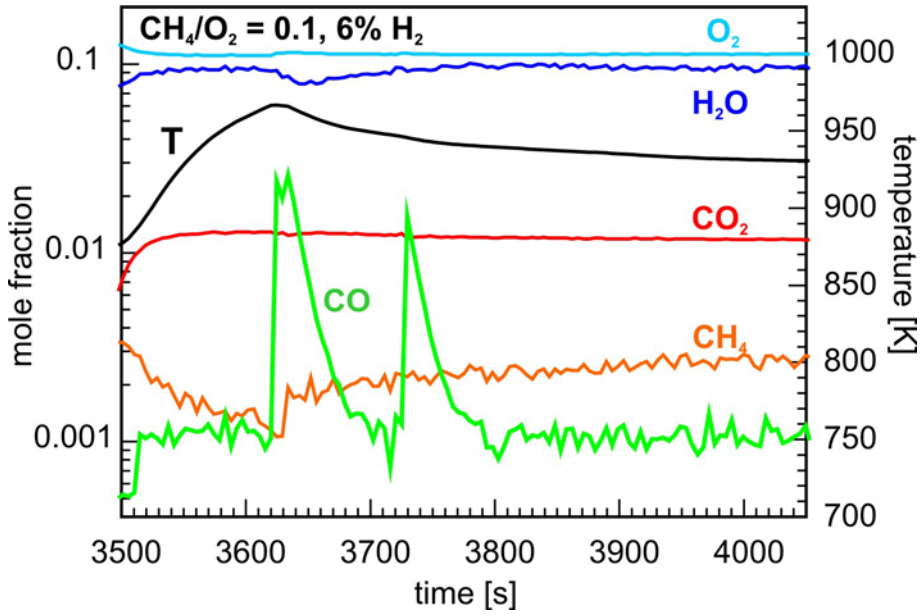

Figure 5.7: Mass spectrum during catalytic oxidation of methane: 80% Ar, 20% O_2 (6.7859 slpm), are fed into the reactor, 436 ml min^{-1} H_2 and 135.7 ml min^{-1} CH_4 (CH_4/O_2 ratio = 0.1) are added. The combustion leads to the formation of H_2O and CO_2 while CH_4 is converted almost completely. The two peaks for CO are due to gas-phase reactions

5.3.2 Results and Discussion

A possible reason for the oscillatory behaviour during the catalytic combustion of methane on Pt coated monoliths could be the formation of a flame in front of the first inert monolith. Simulations show that the diameter of a single channel (1.28 mm) at a gas velocity of 0.26 m s^{-1} is too small to form a flame. On the other hand, the empty quartz tube in front of the monolith with a length of 20 cm and a diameter of 2.6 cm provides enough space for flame generation. The composition of the feed gas was within the flammability limits of H_2 and CH_4, which are 4.1 – 72.5 vol.-% for H_2 in air and 5.1 – 13.5 vol.-% for CH_4, respectively.[82] At the beginning of the reaction, only catalytic combustion occurred in the catalytically active monolith. This exothermic reaction heats up the catalyst and if the thermal radiation heats up the first inert monolith to ignition temperature of the gas mixture a flame may occur. The flow mixture is now consumed very rapidly by a flashback of the flame to the cooler gas inlet where the flame extinguishes. The highly exothermic reaction forms more CO than the catalysed reaction, corresponding to a maximum of the concentration of CO accompanied by a minimum of the concentration of O_2 in Figure 5.8 right. The conversion of CH_4 is almost complete at all times because there is no change in the mole fraction. In the meantime, the catalyst cools slightly down, because the less exothermic CO oxidation provides less heat. Since the flow does not stop, the catalysed reaction restarts, heats up the catalyst and finally ignites the gas-phase mixture once again. This cycle is repeated every 15 s.

With the flame formation in front of the catalyst, the different behaviour with and without H_2 addition can be explained as well. In all cases during the gas-phase reactions, a flammable gas mixture was present. The different measured exit gas-phase temperatures where the flames occurred (around 950 K for H_2 and 1150 K for CH_4) are due to the different ignition temperatures of CH_4/air (~920 K) and H_2/air mixtures (~800 K). However, the flashback of a flame should happen in a much shorter time scale (ms) instead of seconds.

The high concentration of CO during the homogeneous combustion is due to a rapid oxidation of CH_4 by O_2 in the reaction zone of the flame. Subsequently, the CO is oxidised slowly according to reactions 5.1 and 5.2 yielding CO_2, the combination of which can be written as the water-gas equilibrium reaction 5.3.

$$CO + OH \rightleftharpoons CO_2 + H \quad (5.1)$$

$$H + H_2O \rightleftharpoons H_2 + OH \quad (5.2)$$

$$CO + H_2O \rightleftharpoons CO_2 + H_2 \quad (5.3)$$

Since the CO is formed rapidly, but only slowly consumed, the overall CO concentration is above the equilibrium values. Also the residence time of CO in the relatively small reactor volume is short and therefore, the available time for burn-out of CO is too short.

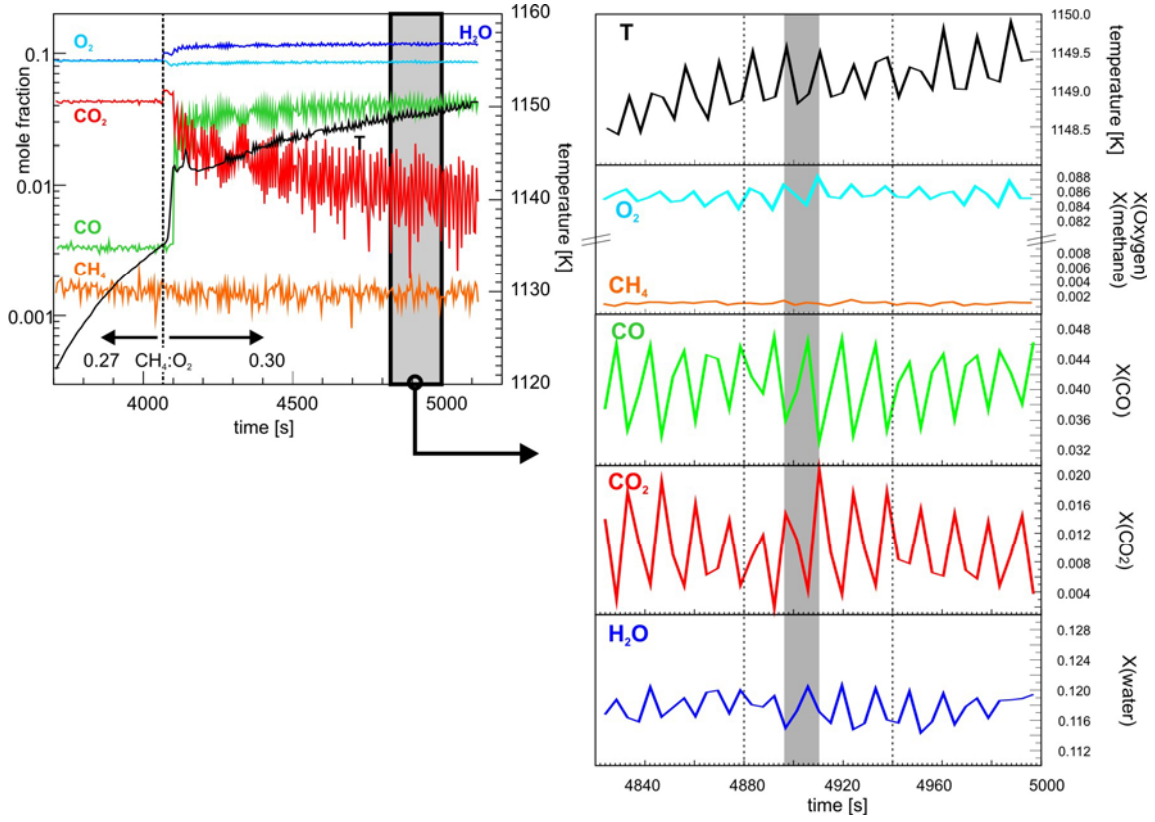

Figure 5.8: Left: Mass spectrum during oscillatory gas-phase reactions. Until 4080 s at a CH_4/O_2 ratio of 0.27 CH_4 is only catalytic converted. At a ratio of 0.30 and a temperature of 1145 K, gas-phase reactions take place, too. They are indicated every 15 s by a clicking sound followed by a sudden CO peak. Right: Zoom in to 3 min during the heterogeneous – homogeneous interaction showing from top to bottom exit gas-phase temperature, O_2, CH_4, CO, CO_2, and H_2O mole fraction.

5.4 Palladium-Palladium Oxide Formation during Catalytic Methane Combustion

Heterogeneous catalytic-reaction systems can be operated far away from thermodynamic equilibrium. Therefore, critical phenomena, such as instabilities, oscillations, or chaos may take place. Although many studies focused on these systems, especially on oscillating reactions (see Table 1 in [83]) they are still not fully understood and need more consideration.

To complete the analysis of the different behaviour of the catalytic combustion of methane after the study of heterogeneous and homogeneous reactions in the previous chapters, this section focuses now on the oscillatory changes in the surface structure during oxidation. Palladium catalysts are known to change the catalytic phase during oxidation reactions and are often used for numerous deep oxidation applications, such as automotive exhaust clean-up, volatile organic destruction, and catalytic combustion for heating and

power.[84] In these reactions the effectiveness of Pd as an oxidation catalyst depends on its complex interactions with gas-phase O_2, which forms PdO_x. At most fuel/air conditions pure Pd^0 is accompanied by PdO, which is formed as a mono- or multilayer on the surface of bulk Pd^0 particles in the presence of oxygen. With time and temperature increase the PdO can grow to independent particles forming a solid two-phase system. While PdO is still supposed to be the catalytically more active phase for CH_4 combustion there are more and more reports [85, 86] showing the presence of both Pd^0 and PdO, which optimises the catalytic performance. An oxidised bulk phase is formed beneath the surface. Isotopic tagging experiments [87, 88] have indicated that the oxidation/reduction cycle of Pd^0/PdO corresponds to a *Mars-van-Krevelan* redox mechanism, where PdO is formed at overall oxidising conditions. Nevertheless, with increasing temperature and/or depleting oxygen concentration the surrounding conditions switch to a reducing milieu (preponderance of methane or hydrogen etc.). The collapse of PdO triggers an autocatalytic way.[87, 89] This redox pathways play a critical role in the activity of supported Pd for oxidation of carbon monoxide [83] and methane.[86] There is still a need for understanding the complex kinetic behaviour. Therefore, as an example the rate oscillations of methane oxidation at lean mixtures on Pd are investigated experimentally and simulated with a mechanism developed by Wolf et al. Only the oxygen containing part of the mechanism is published so far. [90] Jackson et al. has extended the mechanism by incorporating the hydrogen chemistry.

5.4.1 Experimental Conditions

The Catalytic combustion experiments of CH_4 on a Pd coated monolith are carried out in the flow reactor depicted in Figure 3.1. In this case a tubular quartz reactor with a span diameter of 2.6 cm is used. A 10 mm long honeycomb cordierite monolith with a diameter of 24 mm is employed as catalyst. The monolith is composed of about 230 rectangular channels with 1 mm^2 cross-section. The monolith is coated with a 3 wt.-% washcoat consisting of alumina and the noble metal Pd as described in chapter 3.2. The reactor is operated at atmospheric pressure and the gases (Ar, O_2, and CH_4) are fed into the reactor with a constant flow rate of 6.262 slpm, which corresponds to a flow velocity of 0.25 m s^{-1}. The basic conditions were 80 vol.-% Ar, (5.43 slpm) and a mixture of O_2/CH_4 with a stoichiometric ratio of 2.0 for combustion, which corresponds to a flow rate of 1.36 slpm for O_2 and 0.48 slpm for CH_4. Taking into account the smaller gas volume in the catalytic monolith, this results in a velocity of 0.416 m s^{-1} at the channel entrance, which corresponds to a residence time in the order of 10 ms. The reactor was slowly heated up by a furnace using a ramp of 5 K per minute until ignition occurred. The exothermic reaction provides sufficient heat to run the reactor autothermally; hence, the furnace was turned off. Ten minutes after reaching steady state the Ar dilution is slowly decreased until oscillations occur. At an Ar concentration between 74.5 vol.-% and 72.5 vol.-% rate oscillations were observed in the QMS measurement and in a type N thermocouple measurement detecting the exit gas-phase temperature.

Table 4: Parameters of the monolith for the simulation of the oscillatory combustion of CH_4 on Pd.

Physical properties	cordierite monolith	insulation/quartz
mole fraction: $X(O_2)$ $X(CH_4)$ $X(Ar)$	0.21 0.043 0.747	
Porosity	0.495	
heat conduction λ_{rad} [W (m K)$^{-1}$]	2 [a] / 1 [b]	1.36
density ρ [kg m^{-3}]	2100 [a] / 1060.2 [b]	2205
heat capacity c_p [J (kg K)$^{-1}$]	300	730
surface scaling factor $F_{cat/geo}$	45	
catalyst length [mm]	10	
catalyst diameter [mm]	25	
number of channels / shape	230 / square	
channel cross-section [mm^2]	1.13	
Corresponding radius [m]	5.641 10^{-4}	
radiation shield	uncoated cordierite	

a: for compact material, porosity = 0
b: including porosity

5.4.2 Chemical Model

For the simulation, a recently developed mechanism [90] by Wolf et al. was applied in DETCHEM^{MONOLITH}, version 1.5.4.[36] The detailed reaction mechanism, displayed in Table 12, Appendix A, consists of 58 elementary reactions among 52 species. In this mechanism, two states of palladium are decelerated: reduced Pd - denoted Pd(s) – and oxidised palladium (PdO). Bulk species are denoted by a suffix (b). The mechanism also takes into account that the adsorption is temperature dependent, that a surface-surface oxygen exchange (PdO(s) $\rightleftharpoons$ O(s)) and a bulk-surface oxygen exchange (O(b) $\rightleftharpoons$ PdO(s)) take place. Figure 5.9 illustrates the different species of Pd and O molecules. The proposed Pd-O_2 mechanism incorporates surface reactions and bulk uptake and release of O atoms and thereby provides a basis for building larger mechanisms for PdO_x-catalysed hydrocarbon oxidation. The model adopts a detailed description of the surface using multiple Pd-O interactions but no support/Pd catalyst particle interaction. A mean-field approach for surface modelling is implemented. The proposed surface chemistry follows a *Mars-van-Krevelan* mechanism where the balance between sub-surface oxidation and reduction reaction is maintained until the surface layer is destabilised (based on thermodynamics) and a rapid change in the surface coverages takes place.[90]

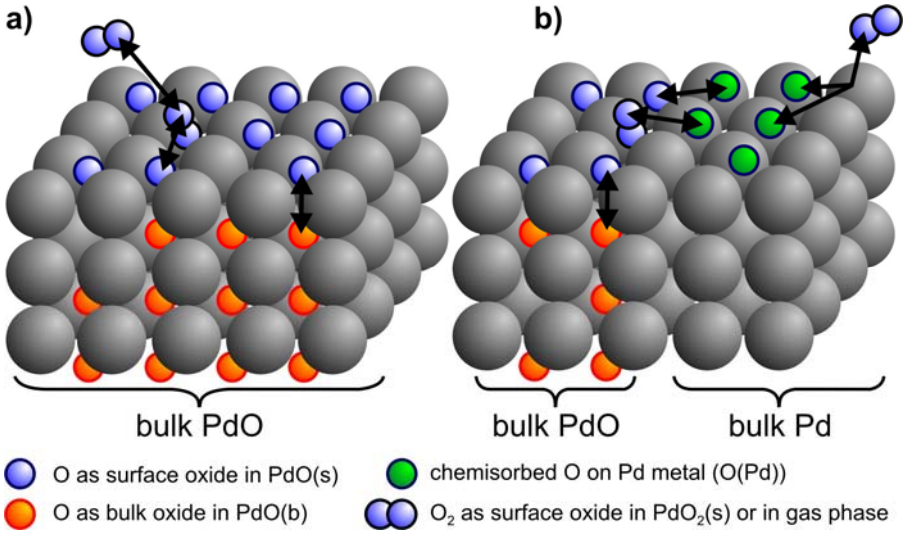

Figure 5.9: Simplified illustration of reactions in mechanism shown on a (100) surface as an example. O and Pd atoms are indicated by smaller and larger circles respectively. a) dominant reactions when bulk is predominately oxidised, and b) reactions when a large fraction of the bulk is reduced.

During heating of PdO(s), the slow increase in surface vacancies leads to a reduction from the bulk phase, which eventually destabilises the predominantly oxide surface layer and leads to the formation of metallic Pd. For catalytic oxidation of species such as CO and CH_4, change in availability of surface oxide and oxide vacancies before and after surface-bulk reduction are thought to play a crucial role. Figure 5.9 shows the oxygen reactions with Pd implemented in the simulation.

5.4.3 Results and Discussion

The phenomenon of Pd-PdO-oscillations is well known in case of hydrogen and CO oxidation.[83, 91] Furthermore, some qualitative rate oscillations during CH_4 oxidation on Pd at fuel-rich conditions are carried out by Zhang et al.[85] It is already known that changes in Pd oxidation state under normal pressures at high temperatures strongly influence Pd activity for catalytic oxidation of hydrocarbons, e.g. CH_4, as well as CO. The rate-limiting steps in catalytic oxidation processes may be changed.

Recent experiments concerning the oxidation of CH_4 in excess O_2 on supported Pd-catalysts performed at temperatures below 700°C have indicated that the rate-limiting step for CH_4 oxidation involves oxide vacancies and neighbouring sites occupied by oxygen permitting rapid H abstraction.[40, 86, 92, 93]

The experiments carried out in the scope of this work are depicted in Figure 5.10. For better visualisation the mole fractions of each species (CH_4, O_2, CO_2, and H_2O) and the temperature of the exhaust gas are plotted in separate diagrams. In general, maxima of the product (CO_2 and H_2O) mole fractions correspond to minima of the reactant (CH_4 and O_2) mole fractions. The rate oscillations could be explained as follows: In these experiments, the

temperature oscillated between 1060 K and 1100 K. As an experimental study by Lyubowski et al. [86] showed that in a temperature range between 623 K and 1103 K the rate of the reaction catalysed by the oxidised Pd significantly exceeds the rate of the reaction catalysed by the reduced metal. The cycle starts with a layer of PdO_x. CH_4 oxidation will occur at Pd atoms sited next to a PdO molecule. At this state, the reaction rate is limited to the available oxygen and remains constant. It is now possible that not only oxygen from the surface but also some oxygen from the lattice can be consumed. Nevertheless, in lean mixtures as applied here the reduction of bulk PdO will play a minor role, which is due to an adequate O_2 gas-phase transport for surface oxidation.[90, 94] In this case the oxide is reduced or thermally decomposed and the reaction rate will decrease to the rate of the reaction with O(Pd) adsorbed on Pd. This behaviour can also be seen in a sharp increase in the mole fractions of CH_4 and O_2 (Figure 5.10) explicable with a decrease of the activity of the catalyst leading to a decrease of the conversion of CH_4 and O_2. Since the partial pressure of O_2 is now higher and the temperature is lower, the metal surface starts to reoxidise. Once a critical thickness of the oxidised layer is reached PdO_x crystals will be formed due to reduced adhesion to the metal.[93, 95] Therefore, more adjacent PdO/Pd sites are provided. The rate of CH_4 oxidation increases and the oscillation cycle starts again.

The correlation between temperature of the product gas, the molar fractions of CH_4, and the trend of the products shown in Figure 5.10 cannot be explained in terms of oxidation and reduction of PdO_x. Since the combustion of CH_4 as well as the oxidation of Pd are exothermic reactions one should expect that in parallel to higher CH_4 conversion accompanied by enhanced product formation the temperature of the exhaust gas should rise. However, the measurement shows the opposite correlation. Just during the period when the consumption of CH_4 and thus the heat release from the oxidation shows a minimum, the temperature increases to its maximum. An error in the measurement can be excluded. Since the shape of the temperature oscillation is the same as that of CH_4 and O_2, a time shift of the measured temperature would be the only explanation as an experimental error. The shift would have to be 90 s by far exceeding the possible residence time of the gas in the connection tubes. Moreover, the correctness of the time scale for mass spectrometer and thermocouple measurements is supported by the fact that both, a sharp temperature rise and a sharp change of the mole fractions occur at the same time and indicate ignition (see Figure 5.11a).

The oscillation of conversion and temperature observed experimentally can be explained by changes in the bonding of O(Pd) to Pd. The time correlation between both oscillations can be explained qualitatively in terms of storage and release of heat in the solid combined with the dynamics of heat transfer. Since the temperature of the catalyst was not measured, no quantitative calculations will be presented in this work.

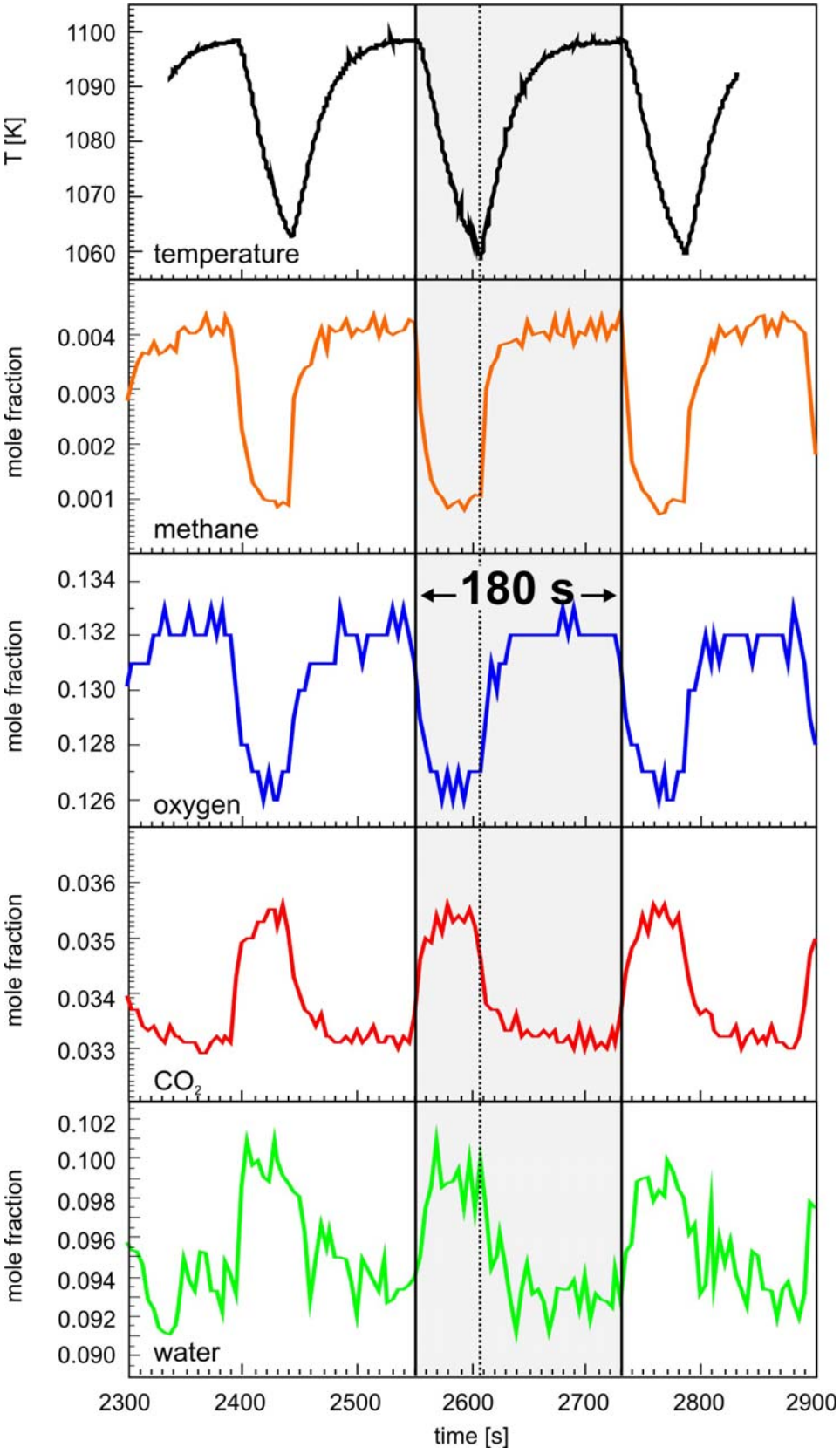

Figure 5.10: Rate oscillation of catalytic methane oxidation in an amorphous Pd-coated monolith. Oscillations occurred at a CH_4/O_2-ratio of 0.21, 74.5 vol.-% Ar, v = 0.25 m s^{-1} (6.262 l min^{-1}, catalyst diameter = 25 mm). A small amount of CO is formed, as well as can be seen in Figure 5.11a.

This process slows down the conversion and decreases the temperature of the catalyst surface. This slow down is accompanied by the regeneration of the active sites by the exothermic reoxidation of Pd leading to an increase in the surface temperature so that the cycle restarts. It should be kept in mind that during the whole cycle almost all CH_4 is converted (between 90% and 98%).

To start the complete combustion of CH_4, which contributes to the major part of heat release, a minimum concentration of PdO vacancies, as the active sites on the PdO phase, has to be present. At a real catalyst there will always be a certain concentration available, even during the growth of PdO on the surface of Pd^0. Yet, the model mechanism starts with a zero concentration of vacancies. For both, the real catalyst and the model mechanism the concentration of vacancies and the conversion of reducing gas molecules like CH_4 increase with higher temperatures (PdO consuming reactions). The more vacancies are available the lower the activation enthalpy is for creating new vacancies (autocatalytic, self-accelerating reaction depending on the vacancy concentration). The more vacancies are formed the more CH_4 adsorption takes place on the PdO. Here the sticking coefficient of CH_4 is significantly higher than on Pd^0 due to the higher surface polarity while the activation enthalpy is slightly higher on PdO. The adsorption and further decomposition of CH_4 on the vacancies of PdO reduces the PdO into Pd^0, which at the same time accelerates the following crucial reaction:

$$\begin{aligned} &PdO(s) + Pd(b) \rightleftharpoons Pd(s) + PdO(b) \\ &(\text{bulk oxidation } \Delta h_f = (-80 + 25X_{Pd(b)})\ \text{kJ mol}^{-1}) \end{aligned} \tag{5.4}$$

$X_{Pd(b)}$ = coverage dependent activation energy of the bulk
$\Theta_{O(Pd)}$ = coverage dependent activation energy of the surface

Furthermore, at higher temperatures the O(Pd) concentration decreases in favour of Pd(s), which then on the other hand accelerates the PdO decomposition until only Pd(s) is left. The CH_4 adsorption and decomposition on pure Pd^0 is lower than on PdO. At the same time the oxygen coverage at high temperatures is very low and hence the CH_4 conversion (activity) drops. When the temperature decreases again due to lower activity to a certain value (dependent on pressure, flow velocity, etc.) the oxygen coverage O(Pd) increases. At the same time, the Pd(s) coverage decreases with corresponding effects on the PdO formation and decomposition reactions. Reaction (5.5) is accelerated, reaction (5.4) is slowing down or zero. Now more and more PdO(s) is formed and the well known Pd/PdO hysteresis is attained again.

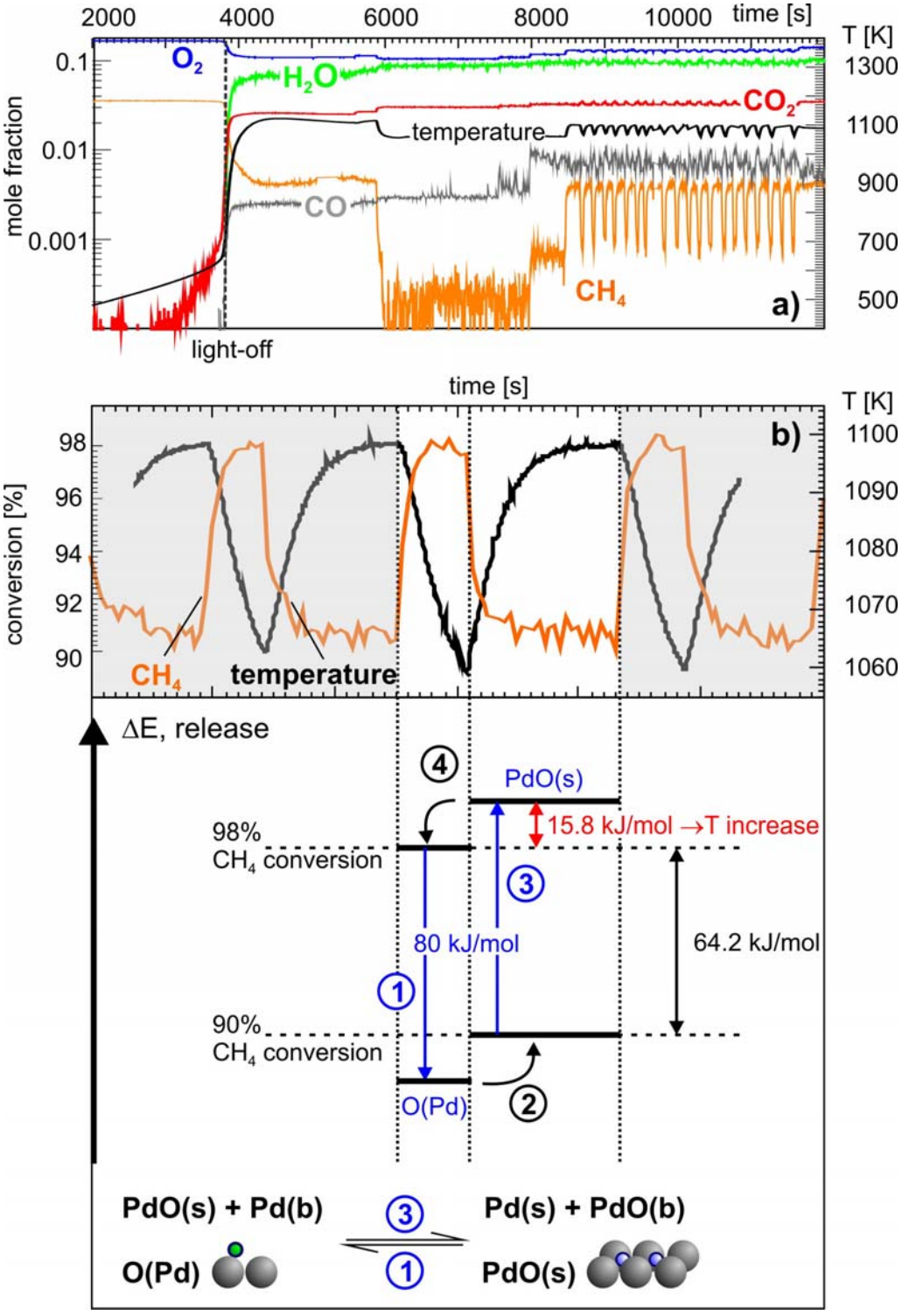

Figure 5.11: a) mass spectrum of the CH_4 combustion. Inlet conditions 80 vol.-% Ar, O_2 and CH_4 (ratio = 2). Furnace is heated until light-off occurs. The furnace is turned off and the Ar is reduced until oscillations started (between 74.5 vol.-% and 72.5 vol.-% Ar). b): Explanation for the temperature behaviour during methane combustion. Top shows the temperature measurement and the CH_4 conversion versus time and bottom the energy release caused by the reactions. Bottom: scheme of reaction pathways leading to the temperature increase. If the bulk PdO(b) is reduced, the PdO(s) bond is weakened, which leads to adsorbed O (O(Pd)). O(Pd) is less active to CH_4 combustion and the conversion decreases

The difference between the heat release of the maximum and minimum CH_4 conversion corresponds to an energy difference of 64.2 kJ mol^{-1} CH_4 flow feed. Since the experiment is carried out in an excess of O_2, enough O is available for all processes. The exothermic total oxidation of Pd yielding PdO (Δh_f = -115.9 kJ mol^{-1},[96]) may play a secondary role for the explanation of the temperature behaviour, because the Δh_f is the same for the formation of PdO(s) and O(Pd). Nevertheless, those two states of bonding are responsible for the different activation energies in the CH_4 combustion cycles. Taking into account all elementary redox reactions of forming bulk Pd(b), surface Pd(s), adsorbed O to O(Pd) or bound O on the surface PdO(s) and in the bulk PdO(b), the following two reactions seem to be sufficient to explain the temperature behaviour (Figure 5.11 b):

$$PdO(s) + Pd(b) \rightleftharpoons Pd(s) + PdO(b) \quad (5.4)$$

$$O(Pd) \rightleftharpoons PdO(s) \quad (\Delta h_f = 0.0 - 57.5\Theta_{O(Pd)} + 137X_{Pd(b)} \text{ [kJ mol}^{-1}\text{]}) \quad (5.5)$$

If the exothermic CH_4 conversion is fast due to many active sites (PdO(s)), the local temperature of the surface is high, too. Now the bulk O (PdO(b)) forms PdO(s) + reduced sub-surface Pd(b), which is an endothermic process (Δh_f of PdO(b) = + 80 kJ mol^{-1}).[90, 97] As the Pd(b) fraction increases, the PdO layers destabilise and result eventually in rapid surface reduction with a transition of PdO(s) to chemisorbed O(Pd).[90, 98] The overall temperature of the gas-phase drops (step 1 in Figure 5.11 b). As O(Pd) is less active for the CH_4 combustion than PdO(s) the CH_4 conversion decreases to 90% producing less energy on the surface (step 2 in Figure 5.11 b). On the other hand this decrease of the surface temperature results in the exothermic oxidation of the bulk Pd(b) forming PdO(b), which promotes the formation of PdO(s) from O(Pd). This exothermic reaction provides more heat (80 kJ mol^{-1}) over compensating the reduced energy release by the slowed down combustion of CH_4 (64.2 kJ mol^{-1}), (step 4 in Figure 5.11 b). This leads to an increase in the gas-phase temperature as determined in the experiment. The surface remains as Pd, since the reaction O(Pd) $\rightleftharpoons$ PdO(b) is fast. At the end of this PdO period, the top layer is oxidised as well. More PdO(s) is now available and activates the CH_4 conversion again. However, all processes depend on the coverage and Δh_f changes due to all processes.

Figure 5.12 shows a comparison of the simulated with the experimental results. The lines represent the simulation, dashed lines for the experiment. The detailed reaction mechanism is able to reproduce the mole fractions of O_2 (blue), H_2O (green), CO_2 (red) and CH_4 (orange) reasonably well. In addition, the trend of the oscillations is the same, as well. The frequency of the oscillations, however, does not fit at all. Whereas in the experiment the duration of one cycle is 180 s the frequency of the simulation is about 1 s. This time scale is too short for surface caused reconstructions as known e.g. from CO on Pt,[83] or H_2 combustion on Pd.[91] An increase in the activation energy of the PdO formation could help to slow down the cycle time, which is due to the fact that the C-H bond brake is the rate limiting step [99] and that PdO sites accelerate this reaction. However, the reality will be

more complex. The transition is influenced by the length of the catalyst, because the CH_4/O_2 ratio differs along the catalyst. Therefore, the process will not occur at all positions at the same time. Some stagnation flow experiments may help to enlight the mechanism. Anyhow, these results show that the oscillatory behaviour can be well explained by the surface model developed by Wolf et al., even if it still has some difficulties to represent the oscillation frequency and needs to be fine tuned in future work.

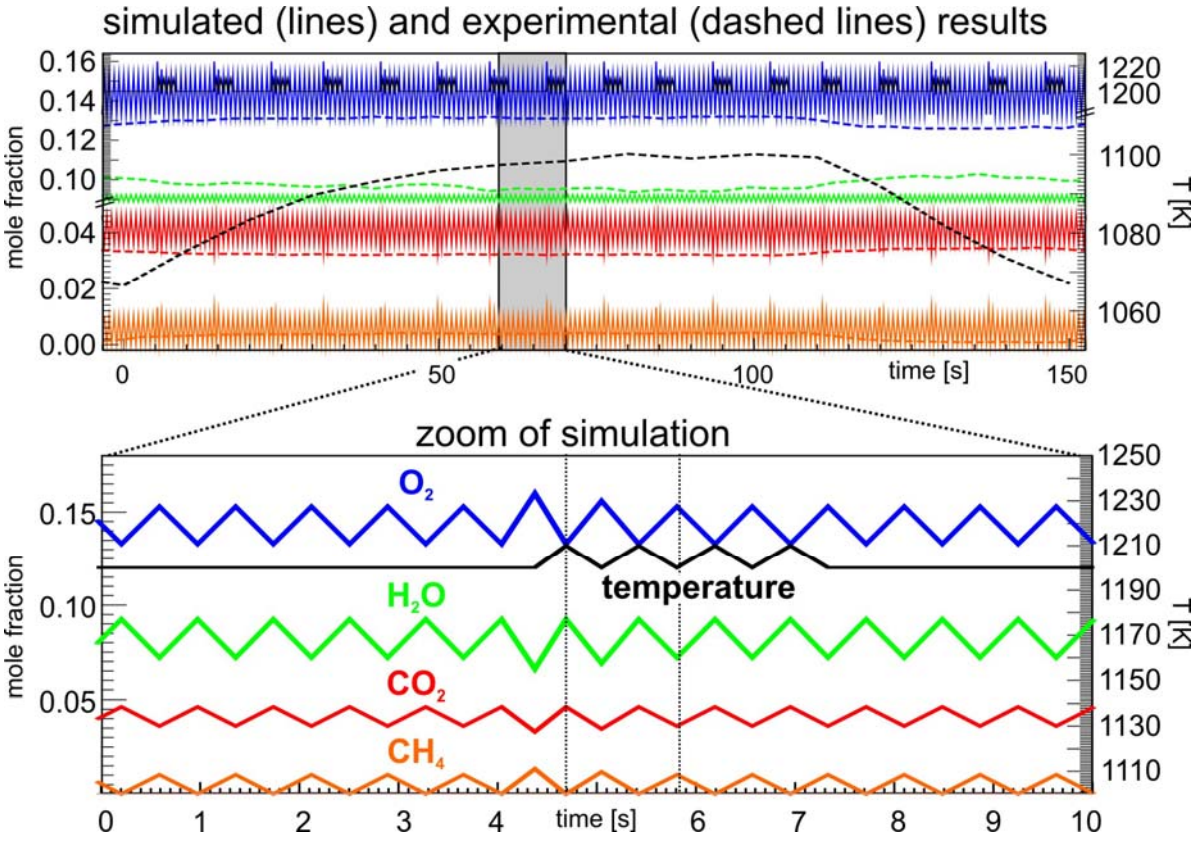

Figure 5.12: Comparison between experimental and simulated results of the methane combustion on palladium. Lines represent the simulation, dashed lines the experiment. The mole fractions fit reasonably well only the oscillation frequency of the simulated results of about 1 s is far too low compared with the experiment (180 s, see Figure 5.10)

CHAPTER VI

6 Catalytic Partial Oxidation of Methane

This Chapter focuses on investigations of the partial oxidation of methane under steady state and on transient state conditions. For the simulation, a detailed reaction mechanism for the CPO of methane developed by Hickman, Tumala, Schmidt, and Deutschmann was applied. The lacking of thermodynamical inconsistence was corrected and the new mechanism (see Table 11, Appendix A) was evaluated using steady-state experiments reported in the first part.[15]

The second part is concerned with the experimental measurement as well as the numerical simulation of the ignition process of CPO of methane on two different support materials.[41] For better understanding of the influence of the physical properties of the support on the reaction rates and ignition, six imaginary cases with varying heat capacity (c_p), heat conductivity (λ), and density (ρ) are simulated.

Furthermore, the catalytic properties of monoliths prepared with rhodium nano-powder are investigated. The nano-powder itself was produced by Laser ablation as described in chapter 3.2.3.

6.1 CPO of Methane on a Rhodium Coated Honeycomb Monolith: Steady-State System

Monolithic catalysts are frequently used in natural gas conversion processes not only for catalytic combustion [28, 69] but also for partial oxidation of light alkanes.[2, 100] In particular at short contact times, a complex interaction of transport phenomena and reaction kinetics can occur. Chemical reactions can take place not only on the catalytically active surface but also in the gas phase as was shown for partial oxidation of methane on rhodium at elevated pressure [6] and oxy-dehydrogenation of ethane on platinum at atmospheric pressure.[101] In those studies, computational tools for the numerical simulation of heterogeneous reactive flows were developed and applied to a two-dimensional simulation of a single-channel in a foam monolith. The complex shape of the pores of the foam monolith was simplified by using a model of a straight tube. Using a simple surface reaction model a three-dimensional simulation of the catalytic partial oxidation of methane to synthesis gas in a wire gauze configuration has been performed previously by de Smet et al.[102]

The understanding of the details of the reactor behaviour demands a sufficient agreement between experimental and modelled flow field without neglecting the complex chemistry. Therefore, the objective of this study is to achieve an appropriate agreement between experimental configuration and flow field model. The use of extruded monoliths exhibiting straight channels with rectangular cross-section guarantees a well-defined geometry. The model describes a three-dimensional flow field coupled with detailed reaction mechanisms and an enthalpy balance including a heat conducting channel wall. As examples, experiments and numerical simulations carried out for the partial oxidation of methane to synthesis gas on a rhodium coated honeycomb monolith are discussed.

6.1.1 Experimental Conditions

The experiments were carried out in the reactor described in chapter 3.1. Here the tubular quartz reactor had an inner diameter of 26 mm. The tube contained a 1cm long extruded monolith with a well-defined rectangular cross-section (1mm x 1mm) of the channels. The catalyst is impregnated with 3 wt.-% Rh. The CH_4/O_2 mixture, diluted by 80 vol.-% Ar, was fed to the reactor at a total volume flow of 7 slpm leading to a uniform velocity of 0.26 m s^{-1} (at 300 K and 1.1 bar) in the monolith channel. Taking into account the smaller gas volume in the catalytic monolith, the effective velocity reaches 0.55 m s^{-1} at the channel inlet. The catalyst consists of 234 channels with an effective total cross section of 234 mm^2 compared to a cross section of 452.4 mm^2 of the whole structure. The reactor was placed inside a furnace, which was heated up to initiate the reaction. After ignition, the furnace was switched off and the reactor then was operated autothermally. The gas

temperature at the exit of the catalytically active monolith was determined using a thermocouple placed inside a thin quartz tube to prevent catalytic reactions. Because of heat losses to the ambience, the temperature measured at the exit of the reactor always was significantly lower than the temperature expected at the exit of an adiabatically run reactor would have been. The composition of the product gas was determined by quadrupole mass spectroscopy.

6.1.2 Modelling the Monolith Channel

Simulating a single channel of a whole catalyst means we need to do some simplifications. Although the experiment indicates a significant heat loss, every channel in the model is assumed to be essentially alike. Thus, radial profiles over the monolith as a whole are neglected, and only one single channel has to be analysed. The flow within these small diameter channels is laminar, although the flow velocity is high.

Table 5: Initial conditions of the experiment used for the plug flow simulations

CH_4/O_2	Total flow [slpm]	velocity [m s^{-1}]	$X(CH_4)$	$X(O_2)$	X(Ar)
1.43	7.057	0.26[a] / 0.55[b]	$1.33\cdot10^{-01}$	$9.31\cdot10^{-02}$	$7.74\cdot10^{-01}$
1.54	7.057	0.26[a] / 0.55[b]	$1.13\cdot10^{-01}$	$7.31\cdot10^{-02}$	$8.14\cdot10^{-01}$
1.65	7.057	0.26[a] / 0.55[b]	$1.19\cdot10^{-01}$	$7.18\cdot10^{-02}$	$8.10\cdot10^{-01}$
1.76[c]	**7.057**	**0.26[a] / 0.55[b]**	$\mathbf{1.27\cdot10^{-01}}$	$\mathbf{7.20\cdot10^{-02}}$	$\mathbf{8.01\cdot10^{-01}}$
1.88	7.057	0.26[a] / 0.55[b]	$1.29\cdot10^{-01}$	$6.87\cdot10^{-02}$	$8.02\cdot10^{-01}$
1.99	7.057	0.26[a] / 0.55[b]	$1.37\cdot10^{-01}$	$6.89\cdot10^{-02}$	$7.94\cdot10^{-01}$
2.10	7.057	0.26[a] / 0.55[b]	$1.39\cdot10^{-01}$	$6.64\cdot10^{-02}$	$7.94\cdot10^{-01}$
2.21	7.057	0.26[a] / 0.55[b]	$1.46\cdot10^{-01}$	$6.61\cdot10^{-02}$	$7.88\cdot10^{-01}$
2.32	7.057	0.26[a] / 0.55[b]	$1.50\cdot10^{-01}$	$6.44\cdot10^{-02}$	$7.86\cdot10^{-01}$

a: calculated velocity for the total catalyst
b: effective velocity at the channel inlet
c: 3D simulation of this parameters is depicted in Figure 6.3

To prove the detailed reaction mechanism of CPO of methane on rhodium shown in Table 11, the detailed reaction mechanism is applied in three-dimensional simulations in a CH_4/O_2 ratio range between 1.4 and 2.4 in collaboration with L. Maier[4].[15] The numerical results are evaluated with the experimental achieved results. In these calculations, the three-dimensional *Navier-Stokes* equations for the simulation of the rectangular shaped channel

[4] Dr. Lubow Maier, University of Karlsruhe, Institute for Chemical Technology and Polymer Chemistry

were solved using Fluent 4.4 coupled with DETCHEM.[103] These equations are coupled with an energy conservation equation and an additional conservation equation for each chemical species. The energy conservation equation takes into account heat transport by convection and conduction in the gas phase, heat release due to chemical reactions in the gas phase and on the catalytic surface, and heat conduction in the channel walls. Furthermore, at the outer boundary of the channel wall a term describing external heat loss was added taking into account the experimentally occurring heat loss. The temperature-dependent external heat loss was specified so that the predicted temperature at the exit of the catalyst agrees with the experimentally measured temperature. Because selectivity and conversion in catalytic partial oxidation of light alkanes strongly depend on the spatial temperature profile, the detailed description of the energy balance is crucial for the understanding of the reaction; for more details see Chapter 4. The conditions assumed for the simulation of the single channel of the catalytically active monolith were identical with those used for the experiment. The simulated channel is 1.1 cm in length with the first millimetre being non-catalytic. For saving calculation time only a quarter of the channel is simulated as depicted in Figure 6.1.

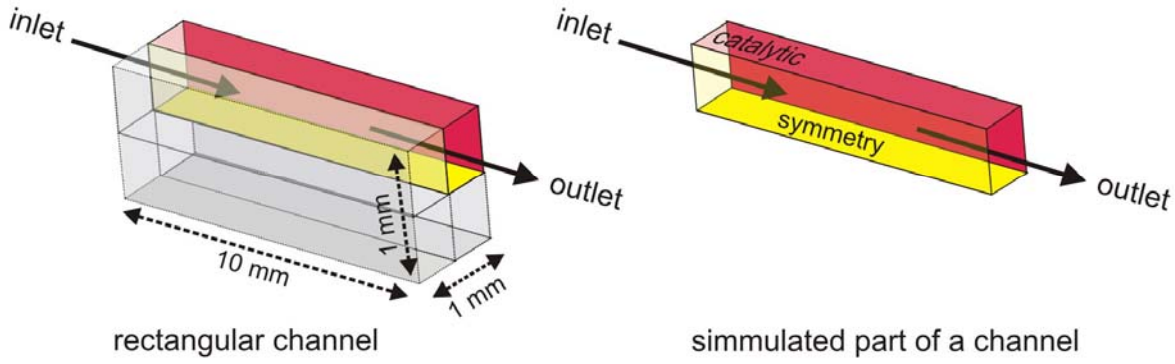

Figure 6.1: Scheme of the simulated part of a rectangular honeycomb monolith channel; only a quarter of the whole channel is simulated.

6.1.3 Results and Discussion

Exemplary, Figure 6.2 shows selectivity, conversion, and outlet temperature as function of the CH_4/O_2 ratio. A good agreement is shown between experimentally determined and computed selectivity and conversion. The selectivity for the formation of synthesis gas and the conversion of methane are lower than the data reported by the Schmidt group [2] due to significant heat loss in the reactor. The computed peak temperature is much higher than the exit temperature, not only due to heat loss but also due to endothermic steam reforming. Nevertheless, at a CH_4/O_2 ratio of about 1.8 a maximum yield of synthesis gas could be determined in the simulation as well in the experiment.

The three-dimensional simulation including the detailed reaction mechanisms allows to study this behaviour in more detail. In previous studies, a surface-reaction mechanism proposed in 1993 by Hickman and Schmidt was used in their pioneering work in 1993, in which steam and CO_2 reforming is not significant.[2, 6] New experimental studies [104] indicate, that, at least steam reforming seems to be an important reaction step being one of the reasons for the development of the revised reaction mechanism.

Figure 6.3 shows the profiles of temperature and the species mass fractions for a CH_4/O_2 ratio of 1.8 revealing fast O_2 consumption at the catalyst leading edge while the consumption of CH_4 takes place over almost the whole length of the reactor. Complete oxidation is limited to the catalyst entrance, where O_2 is still available. Because CH_4 as well as re-adsorbed H_2O decompose into atoms on the surface (Table 11), it cannot be distinguished between direct partial oxidation of CH_4 to H_2 and steam reforming.

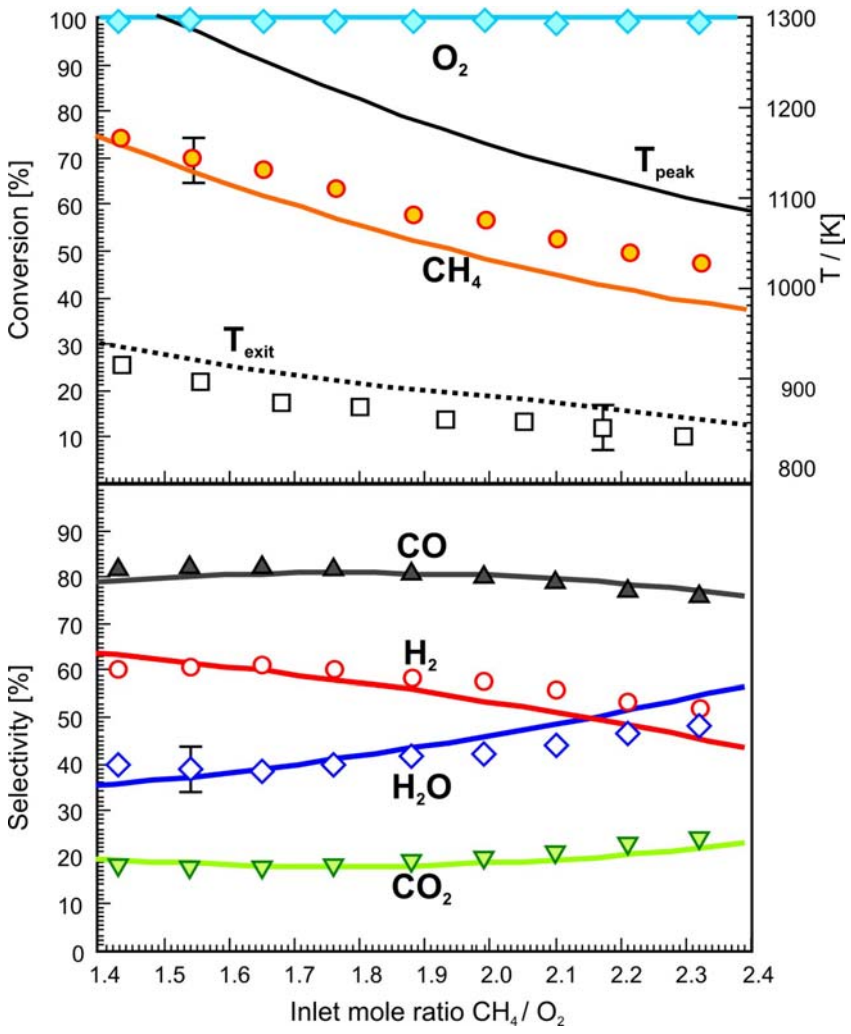

Figure 6.2: Effect of CH_4/O_2 ratio on selectivity, conversion, as well as peak (simulation) and outlet temperature; symbols = experiment, lines = simulation. No washcoat is used. The reactor is operated at atmospheric pressure (1.1 bar). The total feed flow rate of 0.26 m s^{-1} corresponds to a residence time of few milliseconds.

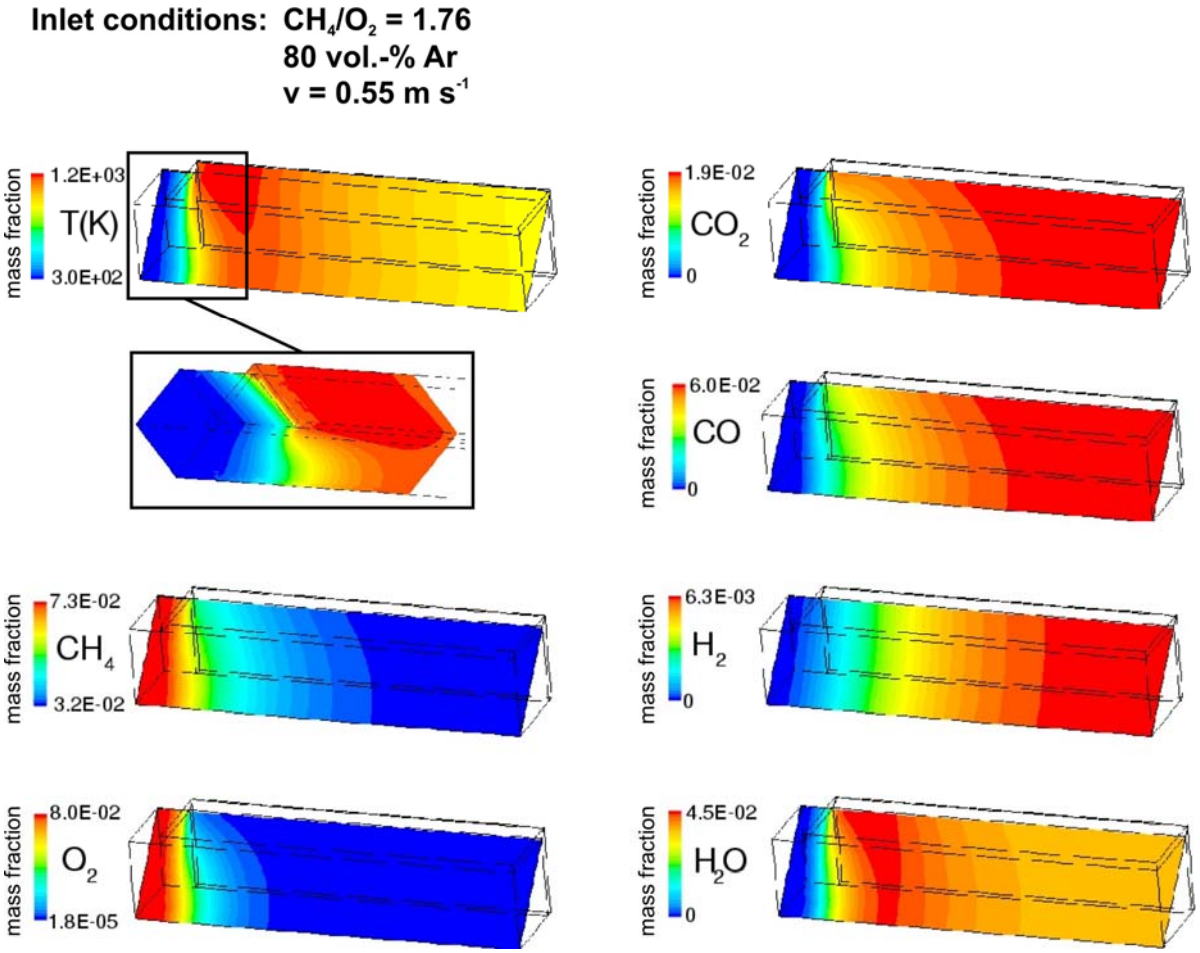

Figure 6.3: Species mass fractions and temperature in the monolith channel (1 mm x 1 mm) at CH_4/O_2 ratio of 1.76, 80 vol-% Ar.[15] The contour plots represent the diagonal face of the simulated channel section reaching from the inner corner of the catalytic walls to the channel axis; the diagonal coordinate has been enlarged for visual clarity, the total length is 1.1 cm with the first millimetre not being catalytically active (no wall is shown). The upper left figure shows the temperature profiles in the channel wall, the inlet, and the front symmetry face at the catalyst entrance. The simulation also reveals that chemical reactions in the gas phase are not significant at atmospheric pressure but become important above 10 bar. [6]

At least further downstream H_2 is only formed via steam reforming. In contrast to that, CO_2 reforming is not significant. The temperature profiles exhibit the strong axial and radial gradients due to chemical reactions and heat transport.

From the results, one can draw the conclusion that this new mechanism is capable to simulate the CPO of methane on rhodium-coated monoliths. It does not only describe the conversion of methane and the selectivity for the formation of the products in steady-state experiments very well but it is also useful to calculate the species concentrations in the flow field of a single channel. In the following chapters it will be applied for more complex processes, e.g. for ignition. A comparison of the 3D with previous 2D simulations shows hardly any difference at the flow rates used in the present work.

6.2 Influence of the Physical Properties of the Support Material on Light-off of CPO

Transient conditions such as light-off and extinction of reactions, homogeneous ignition, and ageing of the catalysts are very important in heterogeneous catalysis, especially to control the operation of reactors in commercial applications. The material properties of the catalyst such as heat capacity, heat conductivity, density, and geometry affect the reaction behaviour. Therefore, it is important to understand the impact of the physical properties not only on steady state conditions but also the impact on transient conditions such as light-off.

Table 6: Material properties of the catalytic monolith and the insulation used in the model [97]

physical properties	alumina monolith	cordierite monolith	insulation/quartz
Porosity	0.368	0.495	
heat conduction λ_{rad} [W (m K)$^{-1}$]	20[a] / 12.6[b]	2[a] / 1[b]	1.36
density ρ [kg m^{-3}]	3500[a] / 2214[b]	2100[a] / 1060.2[b]	2205
heat capacity c_p [J (kg K)$^{-1}$]	850	300	730
surface scaling factor	45	1.5	
catalyst length [mm]	5	10	
catalyst diameter [mm]	6	6	
number of channels / shape	24 / triangular	11 / square	
channel cross-section [mm^2]	0.43	1.13	
corresponding radius [m]	3.713 10^{-4}	5.641 10^{-4}	
radiation shield	uncoated alumina	uncoated cordierite	
T(gas) / T(surface) at start up [K]	300 / 700	300 / 850	
$X(CH_4)$	0.1259	0.1367	
$X(O_2)$	0.0740	0.0843	
X(Ar)	0.8000	0.7790	
velocity[c] [m s^{-1}] at RT	2.0196	2.0196	

a: for compact material, porosity = 0
b: including porosity
c: velocity in the reactor = 1 m s^{-1}.

As an example, the CPO of methane is carried out on two different kinds of support materials: Alumina and cordierite. The influence of the properties of the support materials on the reaction rate and ignition was determined experimentally and compared with the results of simulations performed using the material properties of the catalytically active monoliths compiled in Table 6.

6.2.1 Alumina as Support Material

Alumina as support material is often used in heterogeneous catalysis.[7, 105] Some advantages of this material are the mechanical strength, even at high temperatures, and high surface areas.

a) Experimental Conditions

An alumina honeycomb monolith was used, which is composed of 24 channels with triangular cross-section (0.43 mm^2 each), 5 mm in length and 6 mm diameter.

The monolith was coated with about 3 wt.-% rhodium as described in chapter 3.2. The reactor was operated at atmospheric pressure. A gas mixture consisting of CH_4 and O_2 with a molar ratio of 1.7 diluted with 80 vol.-% Ar was fed at a constant flow rate of 1.7 slpm resulting in a flow velocity of 1.0 m s^{-1} into the preheated (700 K) monolith. This flow rate corresponds to a gas hourly space velocity (GHSV) of $1.96 \cdot 10^6$ and a residence time of approximately 20 ms. The composition of the product gas was determined by gas chromatography (GC) and QMS. The latter was applied for transient measurements such as the ignition experiment of this study. The furnace was used to ignite the reaction by heating up the monolith at a heating rate of 5 K per minute. As soon as light-off occurred, the furnace was turned off.

b) Modelling the Transient Behaviour

To describe the transient behaviour of the whole monolith, it is necessary to couple the reactive flow field in single catalytic channels with the temperature distribution of the entire reactor (model sketched in Figure 3.1). The single channels are modelled by the steady state, two-dimensional boundary-layer equations with transport coefficients that depend on composition and temperature. Surface and gas phase reactions are modelled by elementary-step based reaction mechanisms using the tools for reaction kinetics of the DETCHEM computer package.[35] Along the channel, a varying surface coverage of adsorbed species is taken into account at the catalytic wall.

Here again the detailed surface-reaction mechanism (Table 11) for the CPO of methane on rhodium is applied. Since this mechanism is based on elementary steps, it covers the aspects of global kinetics such as steam or CO_2 reforming. In the ignited steady state, the total surface coverage is low. Therefore, the coverage dependency of the rate coefficients was neglected in previous studies.[15] However, before ignition the surface usually reveals a high coverage with adsorbed species. Therefore, coverage dependent activation energies were chosen for the desorption of CO and oxygen, which is also supported by a recent SFG (sum-frequency generation) study at atmospheric pressure.[106,

107] The mechanism describing the heterogeneous reactions applied here consists of 38 reactions among six gas phase species and 11 surface species (see Table 11).

The simulation also includes a detailed mechanism for gas-phase reactions considering up to 414 reactions among 35 species, which is given in Table 9.[76] However, gas phase reactions are found to be not significant under the conditions applied in this work.

c) Temperature and reaction kinetics in the catalytic monolith during light-off

Using the experimental procedure described in 6.2.1 a), the behaviour of the reactor during ignition was determined. While no conversion occurred at low temperatures, an increasing but small amount of methane and oxygen was consumed above 600 K leading to some water and carbon dioxide formation, whereas no syngas is formed. In the experiments ignition was determined by the sudden, rapid increase in methane and oxygen conversion and temperature. This process was coincident with the onset of the formation of synthesis gas. At the ignition point, the furnace was switched off. As the CPO of methane is strongly exothermic, heat release is sufficient to keep the reaction ignited.

Figure 6.4 (top) displays the numerically predicted temperature distribution in the solid monolithic structure as function of time during light-off. The temperature ranges from 675 K (blue) to 925 K (red). At ignition, the front face of the preheated monolith (furnace temperature is 700 K) is cooled down by the incoming gas (368 K). At the monolith exit, the temperature remains high enough (700 K) to lead to light-off. Here, at first total oxidation of CH_4 to CO_2 and H_2O occurs as indicated by Figure 6.4 (top) showing the gas-phase temperature and species concentration profiles at 0.1, 10, and 100 seconds after ignition. The highly exothermic reaction produces heat, which leads to an increase in the temperature further upstream. There is no H_2 and CO produced at this moment.

The main reaction zone moves towards the monolith entrance during the first few seconds after ignition (Figure 6.4, top). After 10 s, the maximum of CO_2 production already occurs at the channel entrance (Figure 6.4, bottom). Since the temperature rises and oxygen is consumed rapidly, some CO is formed at the channel exit. The hottest part of the reactor is now at the front face, where the highly exothermic total oxidation occurs causing a downstream heat transfer. The only slightly exothermic direct partial oxidation occurs at the exit of the catalyst. At 10 s the temperature is high enough for the formation of hydrogen formation, again beginning at the exit of the channel.

Later, with higher temperatures, the formation of hydrogen and CO increases while the formation of CO_2 and H_2O decreases. After approximately 60 s, conversion and selectivity reach steady state. While the temperature of the solid still has its maximum at the entrance of the catalyst, the gas-phase reaches its maximum temperature, averaged over the radial coordinate, at the exit of the monolith. While most of the oxygen is consumed in the

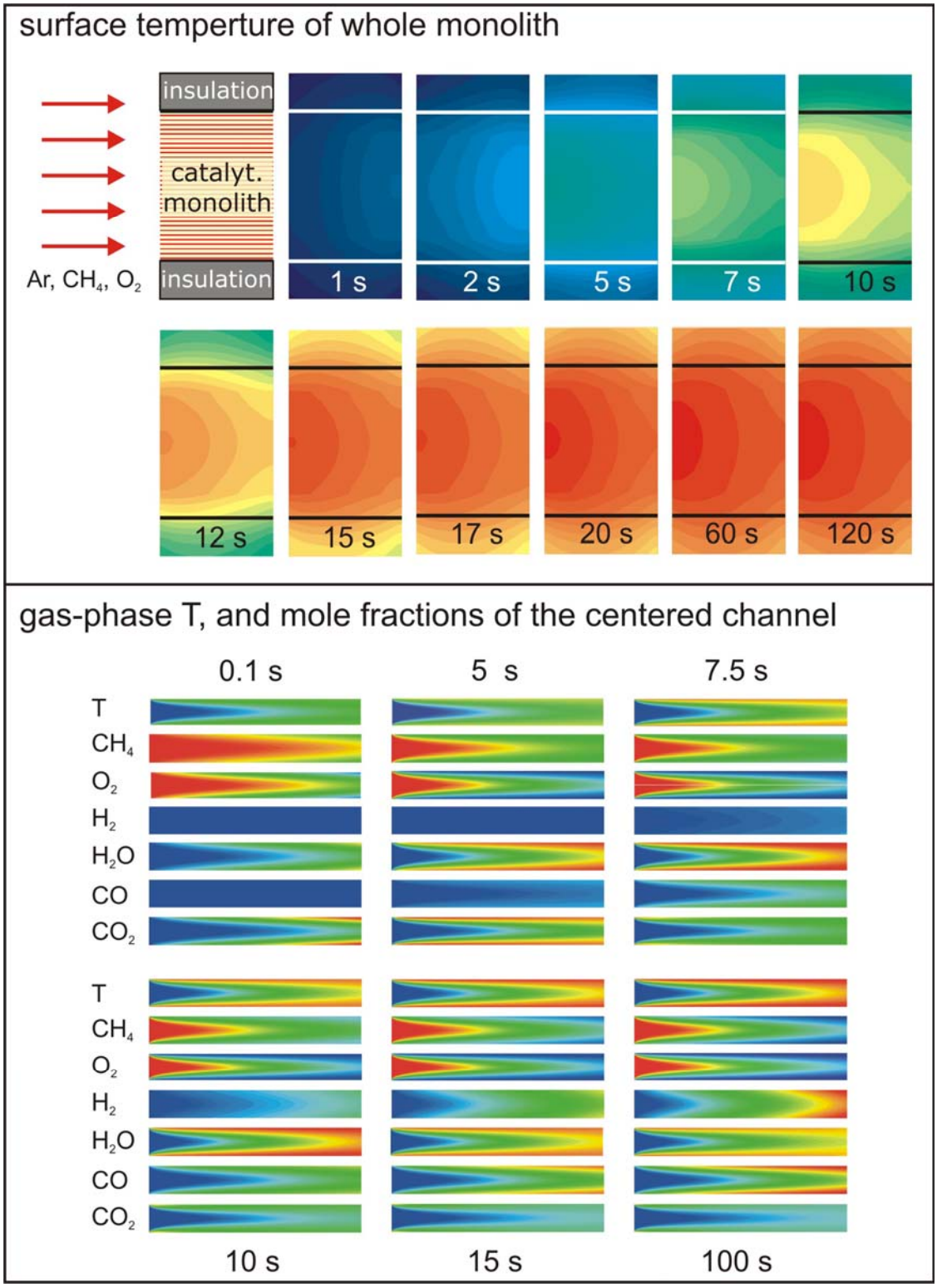

Figure 6.4: top: Numerically predicted temperature distribution in the solid structure of the catalytic monolith and the thermal insulation during light-off. The maximum (red) and minimum (blue) temperatures are 675 and 925 K, respectively. Ignition starts at about 15 s, see Figure 6.5.
bottom: Gas-phase temperature and species mole fractions in a single channel in the monolith's centreline 0.01 s, 5 s, 7.5 s, 10 s, 15 s and 100 s after ignition. The temperature range is 385-900 K, the ranges of the mole fractions are CH_4: 0.043-0.094, O_2: 0-0.055, H_2: 0-0.0412, H_2O: 0-0.058, CO: 0-0.042, CO_2 : 0-0.056.

first part of the reactor leading to total oxidation of methane, most of the syngas, in particular hydrogen is formed further downstream. CO formation starts before hydrogen formation. The two reaction pathways forming hydrogen are direct partial oxidation and steam reforming. CO is formed via direct partial oxidation and steam reforming as well but apparently not via CO_2 reforming. The endothermic steam reforming leads to a temperature decrease along the catalytically active monolith; radial heat loss through the insulation enhances the decrease of temperature. The model includes the calculation of the surface coverage with adsorbed species along the catalytic channels as function of time.

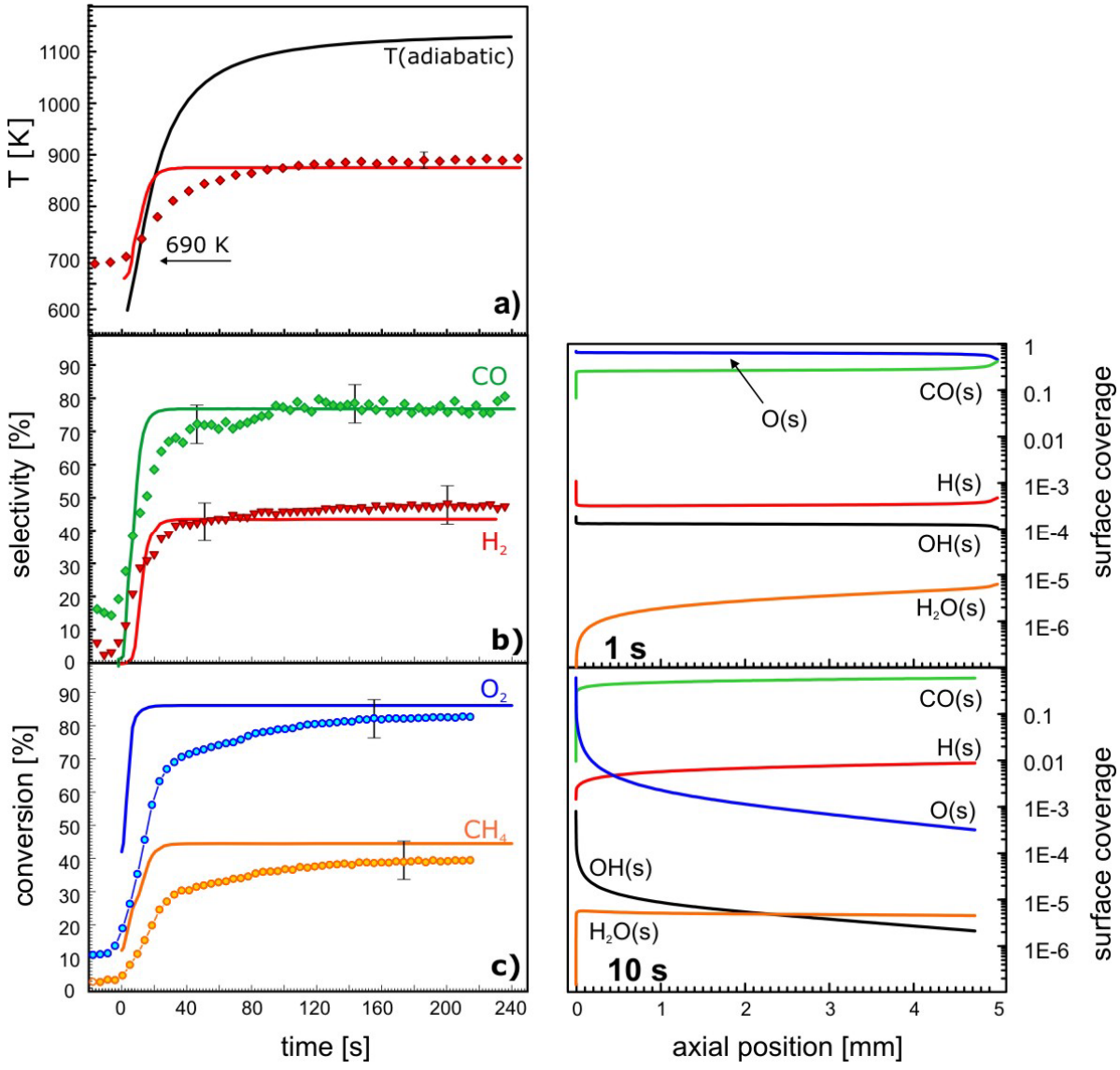

Figure 6.5: a) Temperature profile during light-off. Diamonds represent the measured gas-phase temperature at the exit of the catalytic monolith. The numerically predicted gas-phase temperature is depicted by a solid black line, the temperature of the catalytic surface at the entrance by a dashed-dotted line and at the exit by a dashed line. b) H_2 and CO selectivity and c) O_2 and CH_4 conversion as function of time; symbols/lines represent the experimental/numerical data, respectively.
Right: Surface coverage of CO, O, H, OH, H_2O on rhodium 0.1 s (top) and 10 s (bottom) after ignition.

Figure 6.5 right displays the computed surface coverage 0.1 and 10 s after ignition. Before ignition, the surface is mainly covered by O_2 blocking reactions other than total oxidation. The system is controlled by surface reaction kinetics, in particular by the availability of adsorption sites for methane. The strong sticking of oxygen leads to rhodium oxides increasing the total amount of O_2 available for reactions on the catalyst. The adsorption-desorption equilibrium for O_2 slowly shifts towards desorption with increasing temperature leading to an increase in vacancies on the surface. These vacancies give rise to the adsorption of CH_4 decomposing during adsorption. The large amount of reactive O_2 available at the surface (chemisorbed and as rhodium oxide) leads to fast formation of CO and finally to total oxidation. The temperature increase caused by the total oxidation leads to a further shift of the adsorption-desorption equilibrium of O_2 towards desorption, and hence to more available adsorption sites, self-accelerating the reaction leading to ignition. Furthermore, the rhodium oxide is reduced during light-off. After ignition, the overall reaction is controlled by radial heat and mass transport as can be seen clearly from the steep radial gradients in the profiles of composition and temperature of the gas phase shown in Figure 6.4 (bottom). The total surface coverage is lower and one can only recognise a significant coverage with O_2 at the entrance of the catalyst where complete oxidation occurs. Further downstream, the coverage with O_2 rapidly decreases; all adsorbed O_2 here is due to re-adsorbed H_2O. O_2 on the catalyst is only sufficient for CO formation. CO and H_2 are desorbed before they are oxidised completely.

Since the simulation computes the processes in the single channels at five radial positions, the impact of radial temperature gradients over the entire monolith on the conversion and selectivity in the individual channels can be elucidated. According to the temperature profiles as shown in Figure 6.4 (top) the conversion and the selectivity for the formation of syngas are lower in the outer regions where the temperature is lower (not shown).

d) Experiments Compared with Simulation

In Figure 6.5 left, the numerically predicted gas-phase temperature, conversion of CH_4 and O_2 and the selectivity for the formation of syngas at the catalyst exit are compared with the experimentally derived data. The simulation of the exit gas-phase temperature is in good agreement with the experimental results. The simulated surface temperature at the catalyst exit is slightly higher than the gas-phase temperature. The predicted ignition gas-phase temperature at the catalyst exit was slightly lower than the experimentally determined temperature, which is still within the error bar of the measurement. The slower temperature rise in the experiment is due to the response time of the reactor and QMS. The predicted temperature rather increases like the adiabatic reactor temperature, which is derived from the experimental exit product composition assuming overall adiabatic reactor conditions. As

mentioned earlier, the specification of an accurate term describing heat transfer at the outer wall of the reactor's tube is crucial for the simulation and needs further consideration.

Numerically predicted selectivity for the formation of H_2 and CO (Figure 6.5b) and the conversion of O_2 and CH_4 (Figure 6.5c) agree well with the experimentally determined data. Only little CO and hardly any H_2 is produced at the ignition point. Then, the selectivity for the formation of syngas increases rapidly. However, the simulation reaches steady state faster than the experimentally determined data. The temporal resolution of the used QMS is several seconds explaining the deviations.

A comparison of the present numerical simulation of the single channel using the (parabolic) boundary layer model with a simulation applying a fully elliptic code (Fluent plus DETCHEM), which also accounts for axial diffusion, lead to the same results. Therefore, the deviations between experiment and simulation are not due to the simplifications of the boundary layer approach.

Since the channels of the monolith have a relatively large diameter (0.74 mm) and the length of the monolith is only 5 mm, oxygen breaks through in the experiment and in simulation. The reaction is not yet completed, explaining the low selectivity for the formation of synthesis gas compared to many other experimental studies. The objective of this study was gaining a better understanding of the reactor, in particular breakthrough of oxygen is indeed needed to understand the kinetics.

6.2.2 Cordierite as Support Material

There are many applications using cordierite as support material for a catalyst. As examples, the automotive catalytic converter and a gas-turbine engine with the combustor section based on flow through catalyst monoliths should be mentioned.

a) Experiment

To be able to compare the different behaviour of the support material on the reaction the same experimental conditions are chosen as in chapter 6.2.1. The only difference is the support material, which is cordierite in this case. The honeycomb monoliths (10 mm long and 6 mm in diameter) were coated with rhodium. The rectangular cross section of 1 mm^2 of a single channel results in a hydraulic diameter of 1.13 mm. A 10 mm long inert monolith in front of the catalyst serves as radiation shield. A ceramic cloth is wrapped around both monoliths preventing gas bypass.[41]

The exit gas-phase temperature was monitored using a type K thermocouple placed in a quartz nose behind the monolith. The product composition was determined by QMS as function of time.

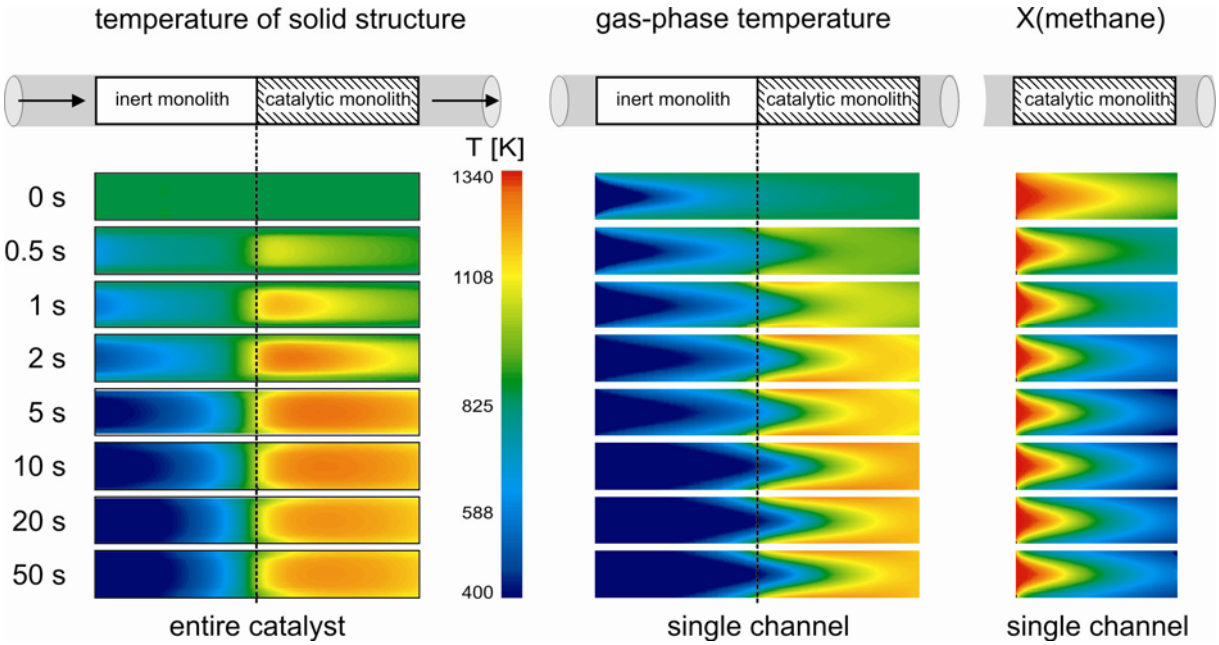

Figure 6.6: Temperature of the solid structure of the monoliths (left), gas-phase temperature (centre) and methane mole fraction (right, range: 0.0-0.137) in a single channel in the centre of the monolith during light-off; the radial coordinates are stretched differently. An inert monolith served as radiation shield and is included to the simulation.

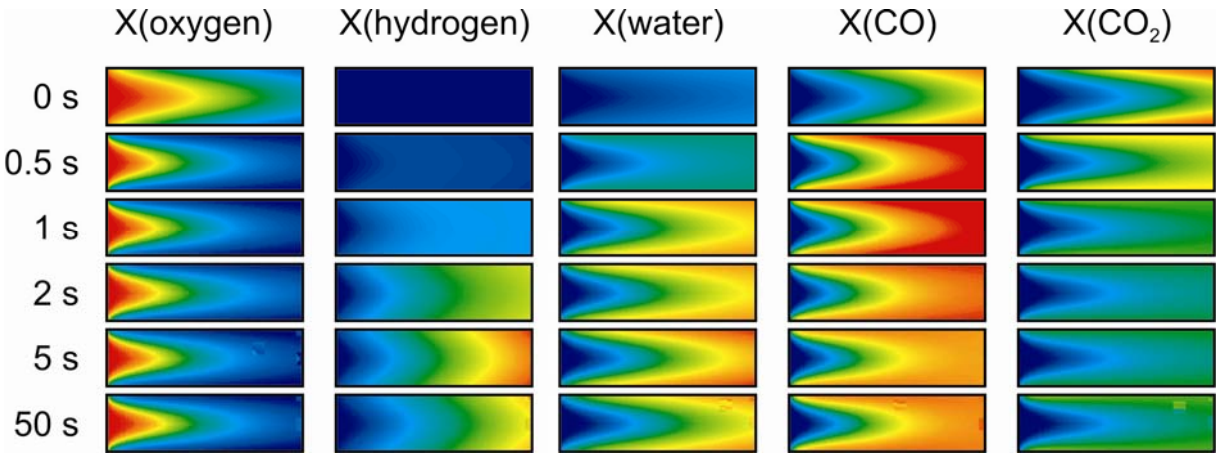

Figure 6.7: Gas-phase mole fractions in a single channel in the centre of the monolith during light-off; the radial coordinates is stretched. (ranges: O_2 = 0 – 0.08, H_2 = 0 – 0.05, H_2O = 0 – 0.07, CO = 0 - 0.05, CO_2 =0 – 0.03

In the example discussed, the molar CH_4/O_2-ratio at the inlet was 1.6, this mixture was diluted with 78 vol.-% Ar. The total volume flow of the mixture at standard conditions (298 K and atmospheric pressure) was 1.7 slpm. At the inlet of the individual channels, this flow rate leads to a flow velocity of 2.0 m $s^{-1}$and a residence time of a few milliseconds. The furnace was used to ignite the reaction by heating up the monolith with a heating rate of 5 K per minute. As soon as light-off occurred, the furnace was turned off. Here, light-off is recognised from the rapid increase in conversion detected by the QMS occurring at 850 K for the chosen conditions.

b) Modelling

The simulation was performed using the mechanisms and models for surface and gas phase reactions lined out in chapter 6.2.1. In order to describe the catalyst loading, the ratio of catalytically active to geometrical surface area has to be known; it can be derived from chemisorption measurements (chapter 3.3.1). Compared to alumina monoliths, the catalytically active surface area of cordierite is smaller by a factor of 10.

The material properties of the support and the insulation are compiled in Table 6. The total porosity of the monolithic structure is 0.495. Heat losses due to conduction, convection, and thermal radiation at the exterior walls of the monolith are included in the simulation and the front radiation shield is simulated, as well.

c) Results and Discussion

Figure 6.6 (left) shows the numerically predicted temperature distribution of the solid structure during light-off. The time is set to zero when the conversion of methane rapidly increases. At this time the furnace, which was used to heat up both the inert and the catalytic monolith, is switched off. The cold feed gas is heated up (Figure 6.6, centre) and an almost homogeneous temperature distribution occurs.

It can be clearly seen how the reaction starts at the front end, where methane is oxidised, mainly to CO_2 and H_2O (Figure 6.7), and the temperature increases. Further downstream, only little conversion occurs. During ignition, radial temperature profiles over the entire monolith are established due to external heat losses (the furnace is turned off now) as well as in the single channel, where the exothermic heterogeneous reactions lead to higher temperatures on the catalytically active wall develop. After approximately 2 s, a hot spot occurs in the first section of the catalytic monolith. After 50 s, the temperature profile in the solid becomes smooth due to heat conduction in the solid structure leading to steady state. This behaviour is a contrast to alumina as support, where the reaction starts at the rear end of the monolith and no hot spot is observed. It is noteworthy that not only the different

heat conductivity of the support but also the total loading and the porosity of the catalyst as well as the geometry influence the temperature distribution.

The product profiles in the single channel (Figure 6.7) reveal that total oxidation is the main reaction during light off leading to a the fast temperature increase. The only slightly exothermic formation of syngas begins slowly with increasing temperatures. One can also recognise that a large part of the formed hydrogen comes from a consecutive reaction, in which the steam reacts with methane. The steam is mainly formed near the entrance of the catalyst where a large amount of oxygen is still available. Aside from heat losses this endothermic reaction causes the slight temperature decrease further downstream.

The coefficient of diffusion of hydrogen by far exceeds that of the other species leading to the different shape of the radial profiles, which also means that modelling the processes in the single channel by a two-dimensional description as done here is necessary. After ignition, the overall reaction is transport-limited.

It is also worth mentioning that the overall conversion reaches its maximum a few seconds after ignition, which seems to be apparently caused by the interaction of different modes of heat transport. Three terms, which describe formation and consumption of heat, influence the light off. The first one is the ambient temperature, which is still close to the temperature of the furnace, the second one the initially very high rate of total oxidation releasing a large amount of reaction heat and leading to the temperature peak discussed above, and the third one the relatively warm heat shield.

d) Experiment vs. Simulation

A qualitatively good but not perfect agreement between experimentally determined and numerically predicted conversion and selectivity as function of time could be achieved (see Figure 6.8). At the ignition point only little CO and no H_2 are produced. Then the selectivity for the formation of syngas increases rapidly. In the simulation, the steady state is reached somehow faster than in the experiment. This deviation is probably due to by the temporal resolution of QMS in the order of several seconds and by the response time of the reactor. Oxygen breakthrough is caused by relatively large channel diameter of 1.13 mm compared to the 10 mm catalyst length. The ignition starts at a temperature of 830 K.

Comparing alumina and cordierite, it can be said that the model is able to describe the different reaction behaviour. In the case of alumina, the ignition temperature is about 140 K lower compared to cordierite. This is due to the larger catalytically active surface area. Furthermore, the ignition starts here at the rear end of the catalyst not in the front as in case of the cordierite support. Even though the simulated curves are steeper than the experimental ones, both studies show that cordierite is igniting much faster.

These results prove that simulations based on mechanisms using detailed chemistry offer a useful tool to study the impact of external parameters on reactor performance, particularly at transient conditions.

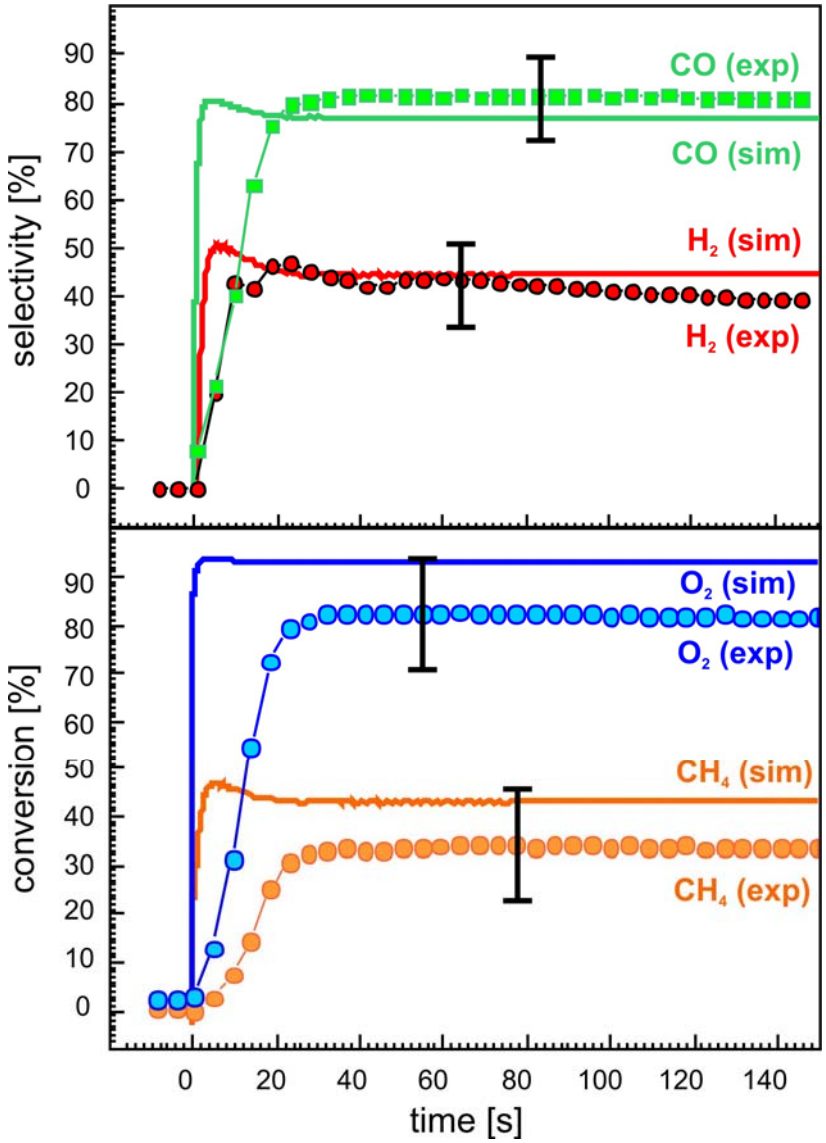

Figure 6.8: Comparison of experimentally derived and numerically predicted conversions (left) and selectivities (right). Lines depict the simulated results and symbols the experiments.

6.2.3 Effect of Physical Properties of the Support Material on the Reaction: A Parameter Study –

As mentioned earlier the physical properties of the support material have a huge impact on the reaction rates and ignition behaviour of CPO of methane. For better understanding, six virtual catalysts are simulated including an inert monolith serving as front radiation shield.[42] The values "c_p <<, c_p >>, λ <<, λ >>, ρ <<, ρ >>" refer to the physical properties of cordierite. In each simulation only one parameter of the physical properties like heat capacity c_p, thermal conductivity λ, and density ρ are changed and compared with alumina and cordierite (see Table 7). The gas mixture enters the reactor at room temperature, while the monolith is heated up to ignition temperature. The model included mechanisms for gas-phase as well as surface reactions. (see Appendix A, Table 9, Table 11)

Table 7: Material properties of the imaginary monoliths

physical properties	alumina	cordierite	c_p <<	c_p >>	λ <<	λ >>	ρ <<	ρ >>
Porosity	0.368	0.495	0.495	0.495	0.495	0.495	0.495	0.495
heat conduction λ_{rad} [W (m K)$^{-1}$]	12.6	1	1	1	**0.005**	**50**	1	1
density ρ [kg m^{-3}]	2214	1060.2	1060.2	1060.2	1060.2	1060.2	**106**	**106020**
heat capacity c_p [J (kg K)$^{-1}$]	850	300	**1**	**2300**	300	300	300	300
surface scaling factor	45	1.5	1.5	1.5	1.5	1.5	1.5	1.5
catalyst length [mm]	5	10	10	10	10	10	10	10
catalyst diameter [mm]	6	6	6	6	6	6	6	6
channel cross-section [mm^2]	0.43	1.13	1.13	1.13	1.13	1.13	1.13	1.13
corresponding radius [10^{-4} m]	3.713	5.641	5.641	5.641	5.641	5.641	5.641	5.641
T(gas) / T(surface), start up [K]	300/700	300/850	300/850	300/850	300/850	300/850	300/850	300/850
X(CH_4)	0.1367	0.1367	0.1367	0.1367	0.1367	0.1367	0.1367	0.1367
X(O_2)	0.0843	0.0843	0.0843	0.0843	0.0843	0.0843	0.0843	0.0843
X(Ar)	0.7790	0.7790	0.7790	0.7790	0.7790	0.7790	0.7790	0.7790
velocity [c] [m s^{-1}] at RT	2.0196	2.0196	2.0196	2.0196	2.0196	2.0196	2.0196	2.0196

[c]: velocity of the gas flow calculated for the reactor diameter is 1 m s^{-1}

a) Results and Discussion

In Figure 6.9 the temperature profile of each catalyst is depicted. The first two cases, alumina and cordierite, are experimentally and numerically studied and described in chapters 6.2.1 and 6.2.2. Not only the temperature profile gives a hint on the reaction behaviour, but also the mole fractions, selectivity, and conversion during light-off shown in Figure 6.10

As mentioned before, with alumina as support material the ignition starts at the back end of the catalyst. The reaction zone moves upstream to the front heating up the catalytic monolith. Finally, the temperature at the catalyst entrance is high enough that reactions start as soon the gas enters. The whole ignition process is quite slow and steady state is reached after about 30 s. On the other hand, the maximum temperature is (with a value of 916 K) low and no hot spot appears. This behaviour of the temperature distribution is a big advantage of this material because the sintering of the catalytic material at this temperature is minimised.[14, 108, 109]

Catalysts using cordierite as a support behave the opposite way. Ignition starts immediately at the entrance of the catalytically active monolith. The temperature rises rapidly and it takes only approximately 10 s to reach steady state. However, the final maximum temperature (about 1300 K) and the hot spot at the entrance support the sintering of the catalytically active material.[51] This leads to a loss of catalytically active surface area, which decreases by a factor of about 5 compared to a cordierite catalyst as prepared (BET_{used} = 4.1 $m^2\ g^{-1}$, BET_{new} = 20.9 $m^2\ g^{-1}$, see chapter 3.4). The loss of the BET surface of catalysts, which are covered with a washcoat is less significant.

Since in both cases the same mechanisms and program were used to verify the experimental work, they can now be used to simulate imaginary catalysts in order to find the best support material.

Influence of Heat Capacity

The main effect of c_p on the reaction is its influence on reaction time, which easily can be seen in Figure 6.9 c), d), and Figure 6.10. A low c_p causes the reaction to ignite at once and steady state is reached after only a couple of seconds. High c_p values slow down the heat change in the solid structure. This results in a delayed start-up and a long time until steady state is reached.

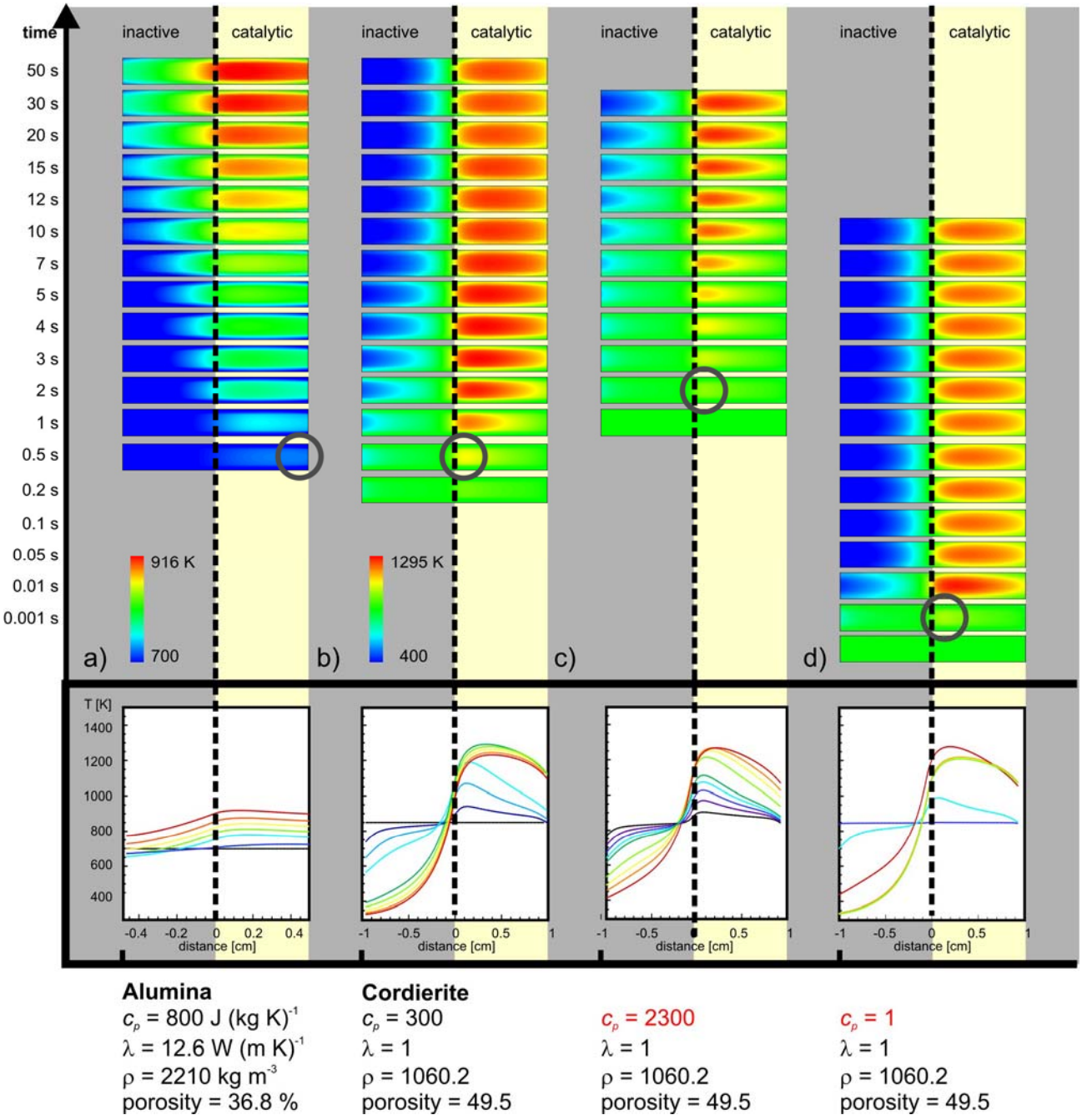

Figure 6.9: Temperature profile of an inert and catalytic monolith during the ignition of CPO of methane on rhodium. Alumina and Cordierite are real systems, while the other six systems are virtual ones based on cordierite. The grey circle marks the start point of ignition. The simulations were done together with B. T. Schädel[5].

[5] Benjamin T. Schädel, Institute for Chemical Technology and Polymer Chemistry

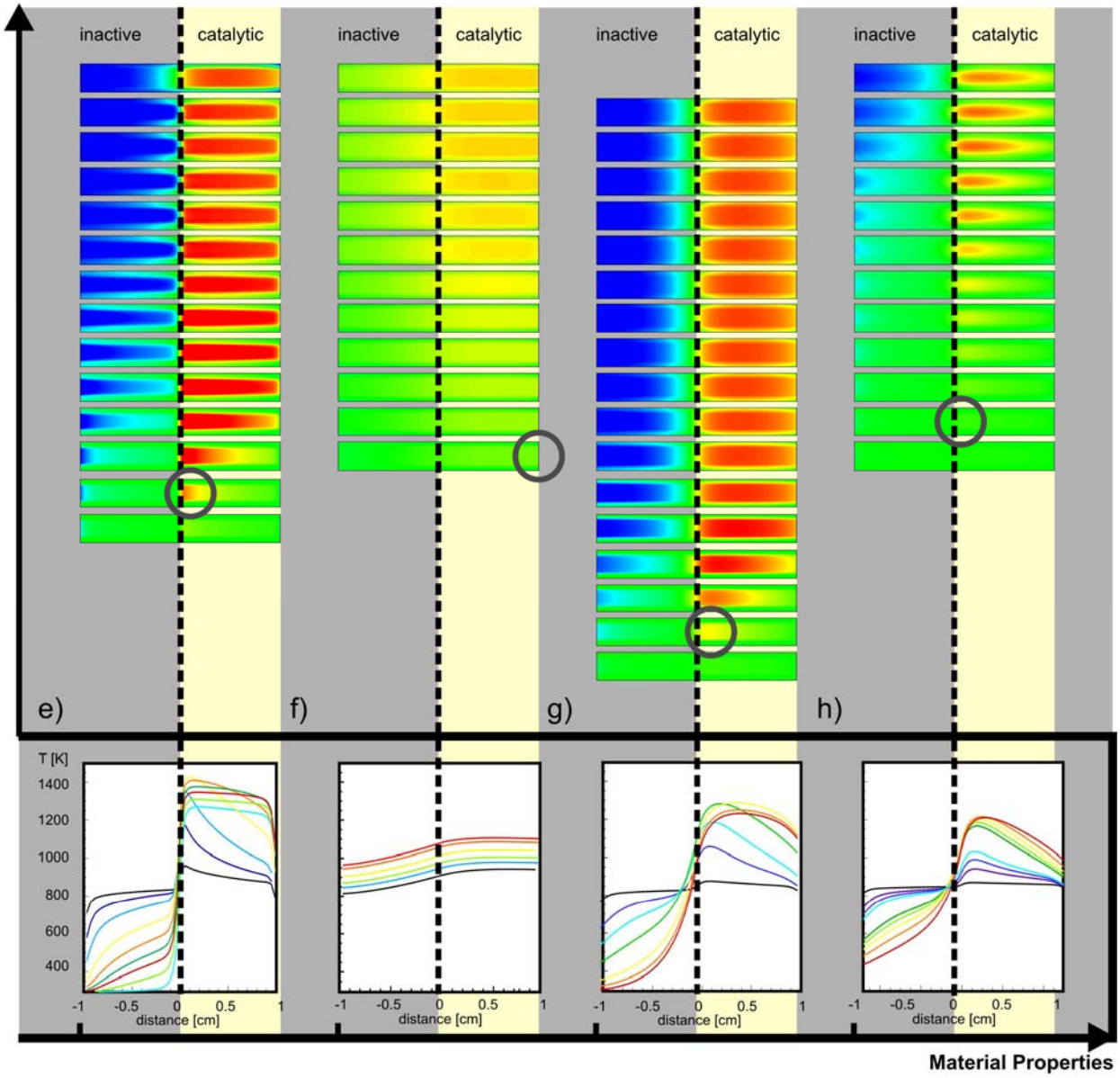

e)	f)	g)	h)
c_p = 300	c_p = 300	c_p = 300	c_p = 300
λ = 0.005	λ = 50	λ = 1	λ = 1
ρ = 1060.2	ρ = 1060.2	ρ = 106	ρ = 10602
porosity = 49.5	porosity = 49.5	porosity = 49.5	porosity = 49.5

Rewriting Fourier's law of heat conduction with energy equation for solids

$$\rho c_p \cdot \frac{\partial T}{\partial t} = \left(\nabla \cdot \lambda \nabla T\right), \quad \frac{\partial T}{\partial t} = \frac{\lambda}{\rho c_p} \cdot \nabla^2 T \tag{6.1}$$

it can simply be seen that a higher c_p value will result in a lower heat transfer rate.[67] So a lower c_p value results in higher heat transfer rate and hence the solid structure heats up fast. Therefore, the surface temperature increases fast, which is represented in a higher reaction rate.

In both cases the ignition starts at the catalyst entrance and the maximum temperature in the catalyst is the same.

Influence of Heat Conductivities

The heat conductivity has the strongest impact on the catalyst temperature (Figure 6.9 d), e)). While in case of low λ the temperature rises fastest with a maximum temperature of 1400 K at about 7 s, there is only a moderate temperature change at low λ values. With increasing thermal conductivity, the temperature becomes more homogeneous due to fast heat exchange in the solid. Within the set of parameters considered in the present work (Table 6), the total temperature change along the catalyst decreases from 1100 K (for λ <<) to 200 K (for λ >>).

In addition, it is worth to mention that the position of ignition is influenced by the thermal conductivity. It is the only physical parameter that lead to an ignition starting from the rear end of the catalyst.

From equation (6.1) it can be seen that the rate of heat transfer is directly proportional to the thermal conductivity. Hence, a higher thermal conductivity results in a faster temperature build up in the solid and results in faster ignition.

Influence of the Density

A low density of the support material is more favourable compared to a high density. The ignition starts fast (Figure 6.9 g)) and reaches steady state after 20 s when all conversions and selectivities remain constant (Figure 6.10). At high ρ values steady state is not reached after 100 s. Actually it seems that the reaction will extinguish. This is indicated by a decrease of O_2 and CH_4 conversion. Here ignition starts again at the front of the catalyst. Equation (6.1) reveals that the density of the solid material has an inverse effect on the temperature build up. Hence a higher density results in a slower temperature rise and

therefore in a delayed ignition. Concluding all the above together, the *thermal diffusivity* α can be defined as

$$\alpha = \frac{\lambda}{\rho c_p} . \tag{6.2}$$

A higher value of thermal diffusivity results in a faster temperature increase and hence facilitating the surface reaction and the ignition.

b) Conclusion

These results show that for the CPO of methane on rhodium a support material with the following parameters is desirable: Next to a high catalytic surface area, the catalyst should have a small c_p and small ρ for fast ignition. In order to prevent huge temperature peaks, which will cause sintering of the catalytic material, the catalyst should have a high thermal conductivity.

Anyway, those physical parameters apparently have no impact on the selectivity for the formation of H_2 and CO. Furthermore, the conversion of O_2 and CH_4 hardly changes. However, the real alumina catalyst with the largest catalytically active surface area shows the highest selectivity for the formation of synthesis gas and the highest conversion. Therefore, a big catalytically active surface area is favourable to improve the selectivity for the formation of H_2 and CO as well as the conversion.

The discussion in the recent paragraph shows that detailed reaction mechanisms integrated into a program coupling surface and gas phase chemistry with the flow field in a single channel and temperature distribution of the catalyst, are powerful tools for designing catalytic reactors. Here, the version 1.5.4 of DETCHEM^{MONOLITH} was applied. Nevertheless, for developing new catalysts it is also necessary to take into account not only the surface area, but also the pore-size distribution. Gas phase reactions catalysed by solid materials occur at the exterior and interior surface of the porous catalyst. A common method to increase the reaction rate by increasing the surface is the dispersion of the catalyst on a suitable porous support such as γ-alumina. Here, diffusion of reactants and products to and from the catalytically active centres in the washcoat can limit the effective reaction rate.[110] Since the computer code DETCHEM has tools for washcoat simulations, which are already successfully applied for automotive catalytic converters,[111, 112] the washcoat model will be applied in future work simulations.

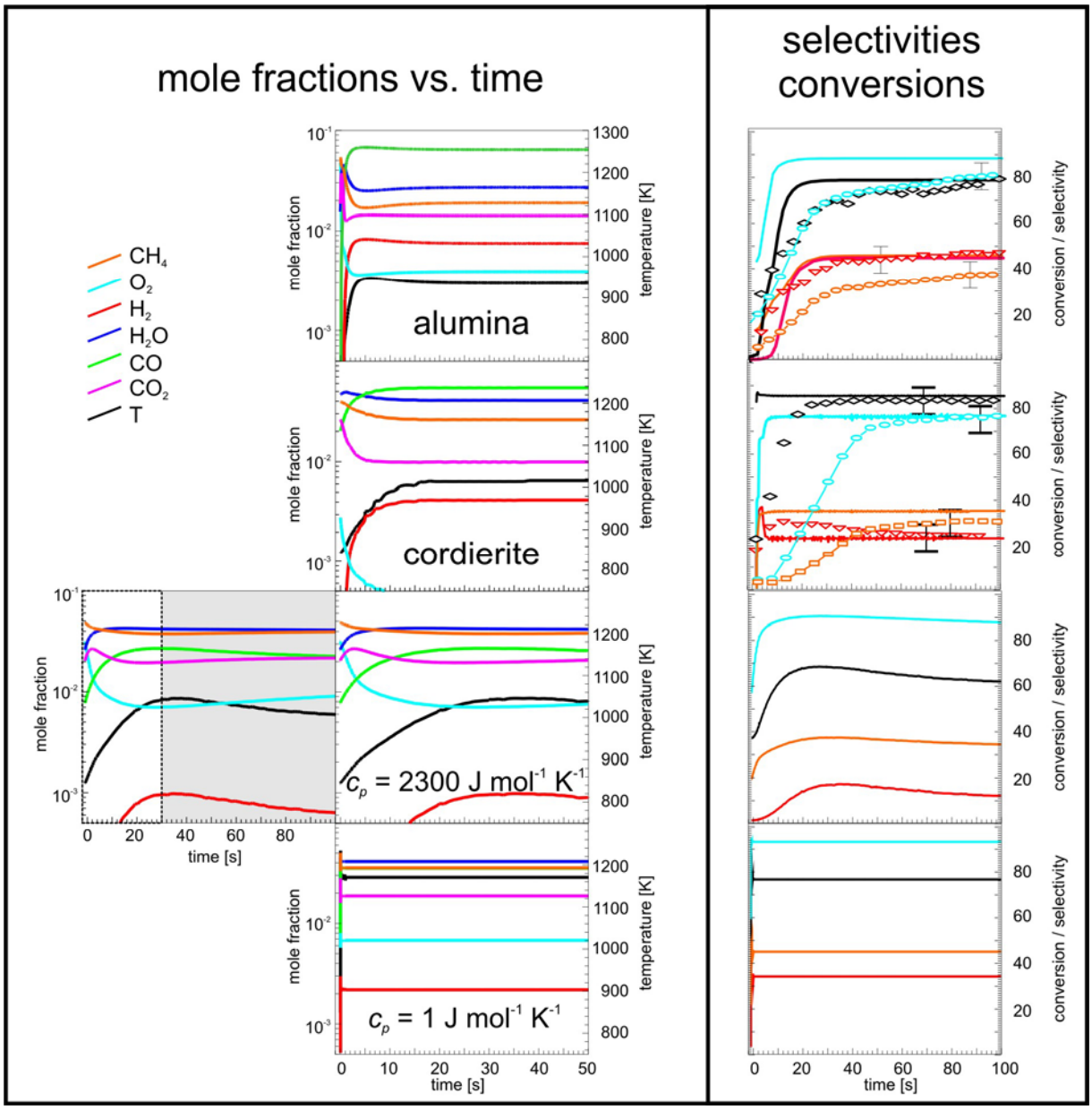

Figure 6.10: Mole fractions (left) at the first 50 s of start-up .Since in case of c_p = 2300 J kg^{-1} K^{-1} and ρ = 10602 kg m^{-3} steady state was not reached after 50 s the spectra for the first 100 s are depicted, too. Right: conversions and selectivities are depicted.

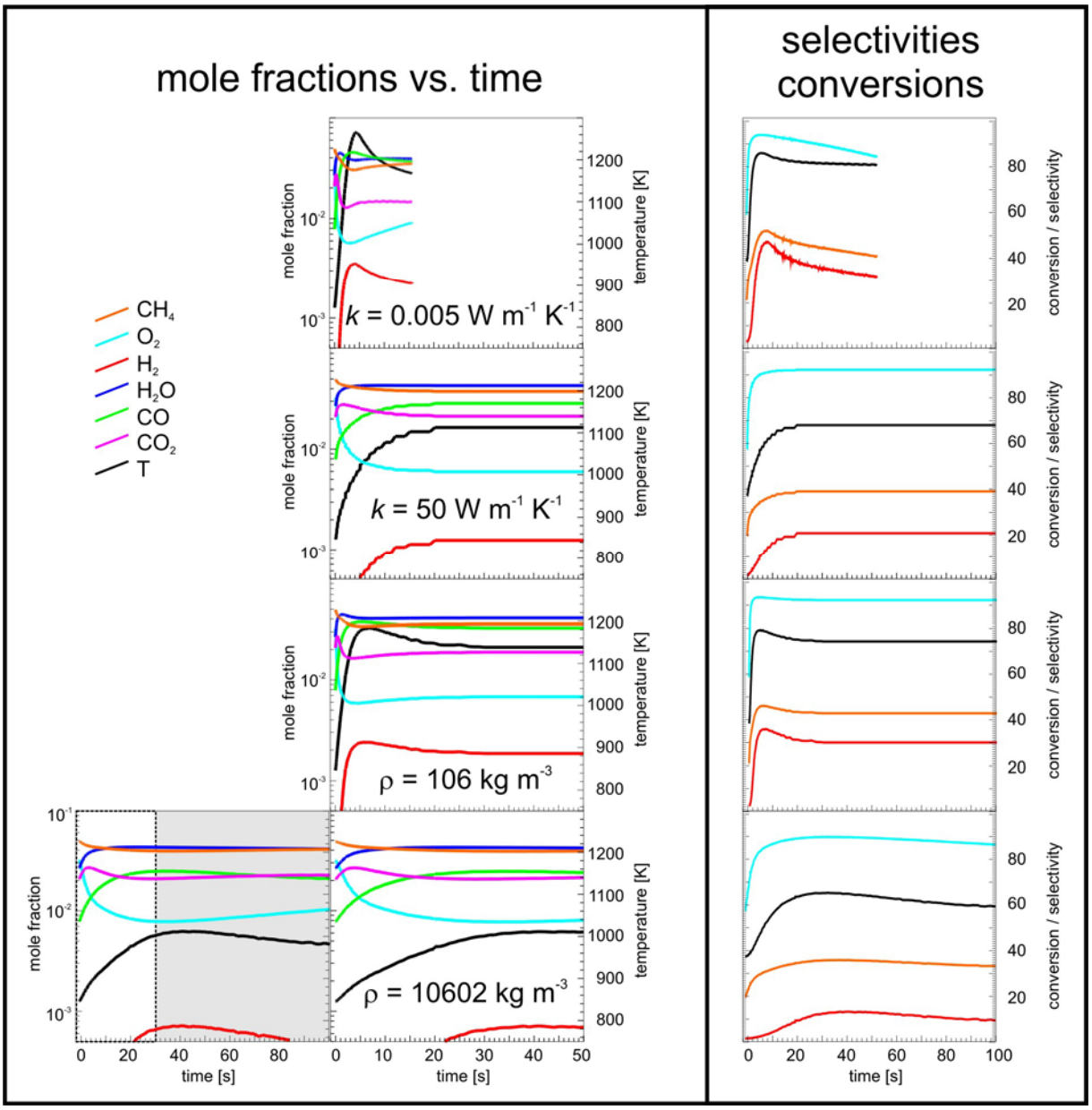
mole fractions vs. time
selectivities
conversions
CH4
O2
H2
H2O
CO
CO2
T
k = 0.005 W m-1 K-1
k = 50 W m-1 K-1
ρ = 106 kg m-3
ρ = 10602 kg m-3
mole fraction
temperature [K]
conversion / selectivity
time [s]

6.3 Comparison of Convential Impregnated Catalysts with Rh-Nanoparticle Supported Monoliths

Every substance in a sub-100 nm length scale regardless of composition will have new properties. This is where much of the scientific perspectives of nanoparticles are. Noble metal and semiconductor nanoparticles are good examples of this principle. The optical, electrical, mechanical, magnetic, and chemical properties can be systematically manipulated by adjusting the size, composition, and shape of this class of materials on the sub-100 nm length scale. Electron transport, manifested in phenomena like *Coloumb* blockade, as well as the catalytic and thermodynamic properties of structures can be tailored when one can rationally design materials on this length scale.[113] It is going to far to mention all the potential applications for nanoparticles. The interested reader may be referred to literature.[114-119]

Nanoparticles may also exhibit outstanding properties as catalysts. Therefore, rhodium nanoparticles produced by laser ablation were fixed on two different support materials. These two catalysts were used for catalytic partial oxidation of methane and the results were compared with those obtained using a catalyst prepared by the wet impregnation of alumina with a Rh salt solution.

6.3.1 Experimental Conditions

The experiments are carried out in the reactor described in chapter 3.1. Here the tubular quartz reactor has an inner diameter of 8 mm. Different methane/oxygen mixtures (range between 1.4 and 2,1), diluted by 75 vol.-% Ar, flow at 300 K and 1.1 bar with a uniform velocity of 1 m s^{-1} (corresponding to 1.70 slpm over the whole monolith) into the monolith channel. The reactor resides inside a furnace, which provides the heat for the reaction and is heated up in steps of 6 K per minute to initiate the reaction. After ignition, the furnace is switched off until steady state is reached. Since the weakest catalyst needs an ignition temperature of 861 K, all other experiments are heated up to 861 K, too. The product composition of the gas phase is determined by quadrupole mass spectroscopy. To obtain the gas temperature at the exit of the catalytic monolith a type N thermocouple is used. Because of heat losses to the ambience, the measured exit temperature was always significantly lower than the adiabatic reactor temperature would be.

As mentioned above three different types of catalysts are used. The classical produced one is an alumina honeycomb monolith. It consists of 24 channels with 0.43 mm^2 triangular cross-section, is 5 mm long and 6 mm in diameter. It is coated with about 3 wt.-% rhodium by wet impregnation as described in chapter 3.2.

For the two other types cordierite served as support material. These monoliths are 10 mm long 6 mm wide and have 11 channels with a well-defined rectangular cross-section (1 mm x 1 mm). The Rh powder used for the coating is produced by laser ablation (Chapter 3.2.3). For the first set of catalysts the Rh nano-powder is elutriated in water and added onto the monolith. A homogeneous Rh slurry was only achieved by stirring the powder in a diluted alumina washcoat suspension. As soon the Rh entered the water it formed clusters with a size of around 100 μm.

All catalysts are treated the same way. After drying they are calcined at 600 °C for 6 h and reduced with H_2 (10 vol.-% H_2 in N_2, 500 °C, 30 min) before the first use.

6.3.2 Results and Discussion

Figure 6.11 shows the experimental results of the CPO of methane on Rh determined by three different types of catalysts. The red circles are the values of a conventional made catalyst by the wet impregnation method (Rh-Al). The green up-triangles are the results observed by a plain cordierite catalyst treated with Rh nanoparticles in water (nano-Rh-c) and the blue diamonds represent the data based on a cordierite monolith treated with a washcoat suspension including Rh nanoparticles (nano-Rh-w). However, during preparation of the nanoparticles catalyst it was found that the particles do not remain in nanometre size, the Rh forms clusters on 100 μm scale at least.

The first diagram depicts the CH_4 conversion versus the CH_4/O_2 ratio, b) the H_2 selectivity, c) the CO selectivity, d) the maximum reaction temperature at a furnace temperature of 861 K and e) the ignition temperature. O_2 is completely converted in all cases.

Nano-Rh-c is the least effective of all tested catalysts. This is revealed in the 250 K higher ignition temperature compared to the best one ensued by a pure CH_4 conversion and pure H_2 and CO selectivity. The catalytic active surface is the smallest due to the preparation. This catalyst also cannot keep the reaction running and extinguishes without further heating by the furnace. Since it was not possible to get a suspension of the Rh nanopowder in plain water (Rh sedimented after a view seconds without stirring), no homogenous Rh loading could be achieved.

Far better results are shown by the catalysts nano-Rh-w and Rh-Al, which exhibit almost the same activity. Both convert the same amount of fuel resulting in the same selectivity for the formation of H_2 up to 90%. An autothermal run of the reaction was possible, but for better comparison of all catalysts, the temperature of the furnace was kept constant. Differences occur only in the ignition temperature, maximum temperature, and the selectivity for the formation of CO. The ignition temperature of the Rh-Al (about 600 K) is the lowest and due to a very high surface area. Lower light-off temperatures are favourable, because less energy for the start-up of the reaction is needed. On the other hand, the catalyst nano-Rh-w is slightly better concerning the selectivity for the formation of CO. The reduced

production of CO_2 results in a lower temperature, because the formation of CO releases less heat than the formation of CO_2 due to the difference of the enthalpies of reaction. Lower temperatures lead to reduced thermal stress and less sintering. Since for the catalysts Rh-Al and nano-Rh-w the important catalytic properties are at about the same level, the results reported here do not permit to decide whether the slight advantages of the nano-seize metal justify the expensive method of preparation.

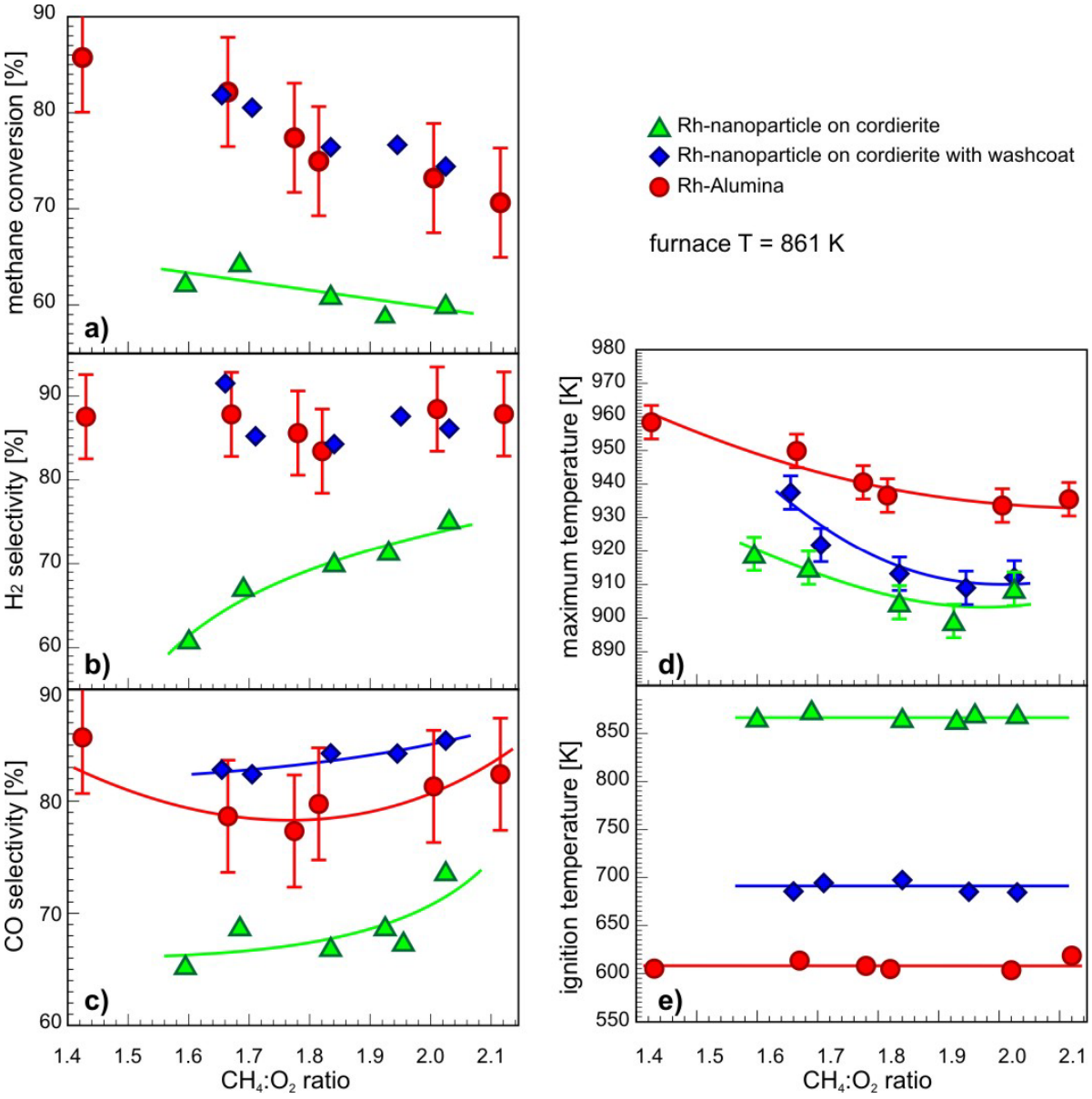

Figure 6.11: Comparison between three different kinds of catalysts. Red circles is classical Rh coated alumina catalyst prepared by the wet impregnation method, the two other catalysts are treated with Rh-nano powder. The green triangles have cordierite as support material and the blue diamonds are based on cordierite with alumina washcoat. Sketch a) shows the CH_4 conversion, b) H_2 selectivity, c) CO selectivity, d) maximum temperature at steady state, and e) ignition temperature. To be able to compare the steady-state conditions in all cases the furnace was heated to 860 K, which was the ignition temperature of the worst catalyst. v = 1 m s^{-1} (total flow of 1.70 l min^{-1}), 75 vol.-% Ar dilution. O_2 conversion was always 100%.

6.3.3 Conclusion

The honeycombs loaded with nano-particles as a catalytically active component did not show any significant improvement of the results of the CPO of methane. In fact, the monoliths impregnated with a Rh salt solution using the classical method, lead to the best results. The big advantage of nano-particles, the very high surface area, was lost during preparation due to coagulation effects. The only way to avoid this disadvantageous effect would be the development of additives stabilising the suspension and thus leading to a homogeneous distribution of nanoparticles on the surface of the monolith.[120] Nevertheless, sintering will occur at high-temperature catalysis, which will deactivate the catalyst by forming larger metal clusters. As long as sintering cannot be prevented it is doubtful that costly nanoparticles catalysts will find some applications in high-temperature catalysis.

For better understanding of the behaviour of nanoparticle supported catalysts it will be necessary to have chemisorption measurements as well as microscopic pictures of the catalysts.

CHAPTER VII

7 Reactions in a Platinum Tube

Within the scope of this work, a model system was set up, where only a single platinum tube with an inner diameter of 1 mm and 32.1 mm length served as catalyst. During high-temperature catalysis the crystallographic orientation of the Pt tube could be estimated to be that of a Pt(111) single crystal.

In the first set of experiments, the model reactor is tested with a well known reaction. Therefore, the catalytic oxidation of CO on Pt at atmospheric pressure was examined in order to understand the ignition behaviour.

The second set of experiments focused on the more complex CPO of methane at very high temperatures (up to 1400 K). Here not only the oxidation of methane and steam reforming seem to play a major role but also the carbon deposition, which caused the reaction to oscillate at CH_4/O_2 ratios exceeding 1.9

7.1 Steady-State Analysis of CO Oxidation

As mentioned previously, carbon monoxide is an important intermediate in the oxidation of all hydrocarbons, and an accurate knowledge of the oxidation chemistry of this component is required to obtain a quantitative understanding of more complex hydrocarbon oxidation processes. For this reason, the detailed kinetics of CO oxidation have been the subject of a large number of studies.

Especially the catalytic oxidation of CO on platinum is one of the most investigated heterogeneous reactions since first studies of *Langmuir*.[121] This reaction is well characterised at low pressures ($p_{CO} \leq 10^{-4}$ mbar). On Pt(100) and Pt(110) island formation or oscillations could be observed and explained.[122-124] The microscopic reason of these phenomena may be caused by surface reconstructions influenced by adsorbates. In this work no such phenomena could be observed and therefore they will not be discussed in more detail. The interested reader may be referred to [122]. This system was chosen to test the newly constructed reactor.

7.1.1 Experimental Conditions

The experiments concerning the oxidation of CO were carried out in a 37 mm long Pt-tube with an inner diameter of 1 mm as described in chapter 3.1. The gases Ar, O_2, and CO were fed into the reactor with a total flow rate of 0.2356 slpm. This corresponds to a velocity of 5 m s^{-1} within the tube. Three sets of experiments are carried out. First the conversion of CO was determined as a function of the gas velocity for $CO/O_2 = 0.11$ and 81 vol.-% Ar. In the second series of experiments, the influence of the Ar dilution ranging from 65 to 95 vol.-% for $CO/O_2 = 0.11$ and a flow velocity of 5 m s^{-1} was measured and finally the flow velocity was varied between 5 and 9 m s^{-1} at 81 vol.-% Ar dilution and CH_4/O_2 of 0.11. The parameters used in this study are compiled in Table 8. Each experiment started at room temperature using the given parameters. The furnace was heated to 923.15 K using a heating rate of 6 K min^{-1} and held constant for some time. The surface temperature of the Pt-tube was measured with a type N thermocouple at the rear end of the tube; the gas phase composition was monitored as a function of time using a QMS. Due to the high heat loss of the system, no significant temperature increase could be observed during ignition. Therefore, it was difficult to find the ignition point by the common criterion. The ignition and extinction temperature was rather defined as the temperature at which the molar fraction of CO_2 exceeded the limit of detection ($X(CO_2) = 0.0002$) significantly fast.

Table 8: Conditions of the experiments: change of CO/O_2 ratio, Ar dilution, and velocity

	Total flow [slpm]	Flow CO [slpm]	Flow O_2 [slpm]	Flow Ar [slpm]	X(CO)	X(O_2)	X(Ar)
CO/O_2	*(65±1) vol.-% Ar, v = 5 m s^{-1}*						
0.03	0.2356	0.0034	0.1140	0.1178	1.1254E^{-02}	0.33658	0.65217
0.05	0.2356	0.0056	0.1122	0.1178	1.7756E^{-02}	0.32758	0.65467
0.11	0.2356	0.01071	0.1071	0.1178	3.5781E^{-02}	0.31575	0.64847
0.21	0.2356	0.0196	0.0982	0.1178	6.1514E^{-02}	0.28639	0.65209
0.26	0.2356	0.0272	0.0906	0.1178	7.0508E^{-02}	0.27211	0.65738
0.42	0.2356	0.0337	0.0841	0.1178	0.10269	0.24191	0.65540
Ar [%]	*CO/O_2 = 0.11 ± 0.011, v = 5 m s-1*						
64.85	0.2356	0.01071	0.1071	0.1178	3.5781E^{-02}	0.31575	0.64847
67.72	0.2356	0.01071	0.1071	0.1178	2.8195E^{-02}	0.29460	0.67720
73.70	0.2356	0.00857	0.0857	0.1414	2.5007E^{-02}	0.23795	0.73704
81.11	0.2356	0.00643	0.0643	0.1649	1.8107E^{-02}	0.17080	0.81109
87.71	0.2356	0.00428	0.0428	0.1885	1.2111E^{-02}	0.11078	0.87711
94.54	0.2356	0.00214	0.0214	0.2120	5.8404E^{-03}	5.4241E^{-02}	0.93992
v [m s^{-1}]	*CO/O_2 = 0.11±0.011, (81 ±1) vol.-% Ar*						
5	0.2356	0.00643	0.0643	0.1649	1.8107E^{-02}	0.17080	0.81109
6	0.2827	0.0771	0.0077	01979	1.7849E^{-02}	0.17034	0.81181
7	0.3299	0.0090	0.0900	0.2309	1.8738E^{-02}	0.16973	0.81153
8	0.3770	0.0103	0.1028	0.2639	1.6879E^{-02}	0.17444	0.80868
9	0.4241	0.0116	0.1157	0.2969	1.7507E^{-02}	0.17335	0.80915

7.1.2 Results and Discussion

Figure 7.1 shows the experimental results of the catalytic oxidation of CO in a Pt-tube. The conversion of CO (blue circles), the ignition temperature (red up-triangles), and the extinction temperature (down-triangles) are plotted as a function of the gas velocity (top), dilution with Ar (centre), and CO/O_2 ratio (bottom). For a better comparison of the CO conversion, the reactor was heated to 923.15 K at a rate of 6 K per min in all experiments.

All series of experiments have one trend in common: With increasing temperature of ignition the lower the conversion of CO decreases and vice versa. In other words, a low temperature of ignition indicates a high activity of the catalyst.

Anyway, the influences of velocity, dilution, and CO/O_2-ratio are not so simple. Nevertheless, the trends can be described in terms of the coverage with CO. If the total amount of CO is high, the Pt surface is mainly covered by CO. There is hardly any vacancy

left for O_2 adsorption. However, the adsorption of both components is essential for the oxidation of CO on the surface. Higher temperatures are necessary to shift the equilibrium describing the adsorption of CO towards desorption leaving free vacancies for the adsorption of O_2.

The top graph indicates the following trend: With increasing gas velocity, the conversion of CO decreases and in parallel the ignition and extinction temperatures increase. Although the CO/O_2-ratio and the dilution with Ar are kept constant, the total molar flux of CO increases leading to the observed trend. Another hint to the strong influence of the coverage with CO on the reaction kinetics follows from the difference between ignition and extinction temperature. The extinction temperature is lower than the ignition temperature. As mentioned before, while heating up the system the surface is mainly covered by CO. As known from the literature CO blocks the O_2 adsorption if the coverage of the surface with CO exceeds a critical CO value (about 0.4).[125] O_2 needs for adsorption two vacancies sited next to each other. Cooling down while the reaction is ignited implies that there is always some O_2 on the surface.

The maximum of the conversion and the corresponding minima of temperatures in the centre graph are due to two effects. Here the CO/O_2-ratio and velocity are constant and the dilution with Ar is varied in a range from 65 vol.-% to 95 vol.-%. With increasing dilution (up to 75 vol.-%) the conversion of CO increases and the ignition temperatures decrease. Again like mentioned above the total flux of CO decreases leading to less CO occupation of the surface, which leads to decreasing ignition temperatures. Again, the difference between ignition and extinction temperature (in the order of about 6 K) suggests kinetics controlled by the coverage with CO. For dilutions exceeding 80 vol.-% the second effect becomes predominant. The activity of the catalyst decreases again while ignition and extinction temperatures increase. This is a result of the lower concentrations of the reactants. They do not reach the surface in time and a brake through of CO is observed. Due to the decreasing overall coverage of the surface, the difference between ignition and extinction temperature decreases and finally disappears at a dilution of about 95 vol.-%; the ignition and extinction temperatures are the same and the surface coverage is no longer the rate-controlling feature.

Finally yet importantly, the bottom figure shows the influence of the CO/O_2-ratio. The velocity and dilution with Ar are kept constant for this series of measurements. With CO/O_2-ratios increasing from $CO/O_2 = 0.011$ (very low CO partial pressure, i.e. very lean mixture) to $CO/O_2 = 0.46$ the conversion of CO decreases accompanied by increasing ignition and extinction temperatures. The higher the O_2 concentration is the lower the coverage of the surface with CO. The rate limiting critical coverage of the surface with CO is not reached.

Therefore, the reaction starts at low temperatures combined with a high conversion of CO. Under these conditions, practically no temperature hysteresis can be observed since O_2 has no inhibiting effect on the adsorption of CO.

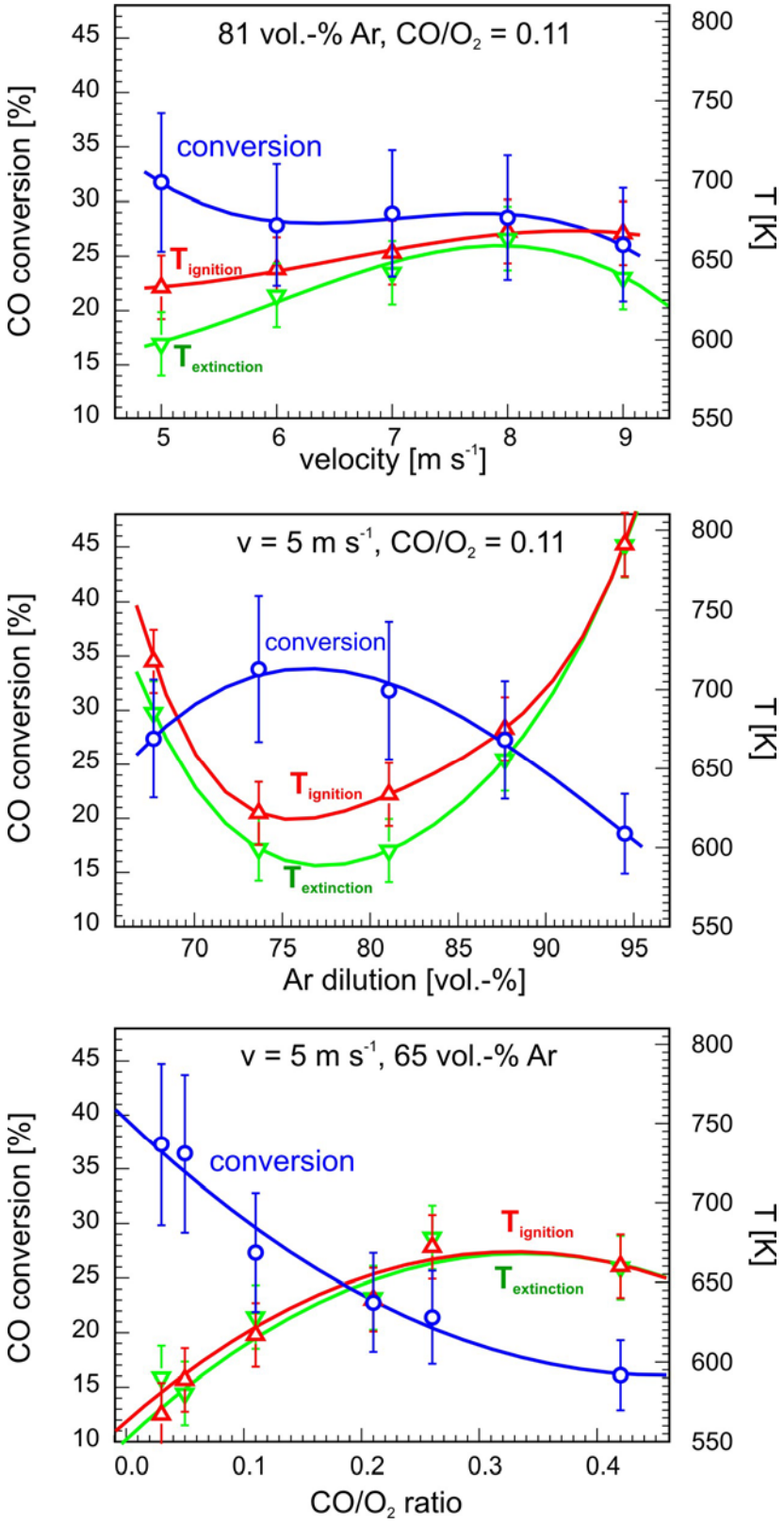

Figure 7.1: Catalytic oxidation of CO in a Pt-tube. Blue circles represent the CO conversion at 923 K furnace temperature, the red up triangles the ignition temperature and the green down triangles the extinction temperature. Top: CO conversion versus different velocities, centre CO conversion at different Ar dilutions and bottom CO conversion versus CO/O_2 ratio.

The flow experiments in a Pt-tube with a fast measurement (QMS) and atmospheric pressure behave similar to stagnation flow experiments on a Pt-foil investigated by Sum Frequency Generation (SFG).[126] Therefore, this setup can be used to complete SFG measurements. In addition, it is obvious that this reactor can be used for kinetic studies and is now used for the investigation of the CPO of CH_4 in a Pt-tube.

7.2 Catalytic Oxidation in Fuel-rich Methane-Oxygen Mixtures

7.2.1 Experimental Conditions

In this set of experiments, the reactor as described in chapter 3.1 was equipped with a 37 mm long Pt-tube with an inner diameter of 1 mm. The gases Ar, O_2, and CH_4 were fed into the reactor with a total flow rate of 0.4712 slpm corresponding to a velocity of 10 m s^{-1} in the tube. The dilution of 75 vol.-% Ar (0.353 slpm) was kept constant in all experiments. The CH_4/O_2 ratio changed between 1.44 and 3.0. Each experiment started at room temperature with the given flow rates. The furnace was heated to 1373.15 K using a heating rate of 10 K per minute; subsequently the temperature was kept constant for some time. The surface temperature of the Pt-tube was measured with a type N thermocouple at the front end of the tube and the gas-phase composition was monitored using a QMS. Due to the high heat loss of the system, the furnace had to provide heat all the time.

Some difficulties occurred during the measurements with the Pt-tube. A blind measurement with only Ar showed that in this set-up the mass spectrometer did not get enough sample for its measurement at all temperature regions. Since a membrane pump expedited the sample gas, air entered the system if the total flow through the reactor was not high enough. An increasing O_2 peak and "CO" peak detected the air, where the "CO" was due to the coincidence of the masses of CO and N_2. The temperature dependent functions of air dilution and incoming molecules were determined and the spectra are corrected as described in chapter 3.5. Though, the values of O_2 and CO need to be treated carefully and could only be taken to see a trend. These experiments were performed in cooperation with T. T. Nam[6].

[6] Tran Tham Nam, University of Karlsruhe, Institute for Chemical Technology and Polymer Chemistry

7.2.2 Results and discussion

As mentioned above, in the series of experiments described in this chapter the CH_4/O_2 ratio is the highest compared to the experiments described in previous chapters. In some cases there even was an excess of CH_4 in the feed gas. Depending on the CH_4/O_2-ratio, the behaviour of the reactor changed considerably. For CH_4/O_2-ratios ranging from 1.44 to 1.84, steady-state conditions occurred for all temperatures. For CH_4/O_2-ratios exceeding 1.9, oscillations occurred at temperatures close to 1250 K. In fuel-rich mixtures the reaction kinetics become rather complex at high temperatures. Besides the total and partial oxidation of CH_4, steam reforming, carbon deposition from CH_4 and carbon removal play a role. A simulation designed to explain the processes occurring during the partial or total oxidation of methane for the whole range of CH_4/O_2-ratios needs to include at least the reactions listed below.

Oxidation of CH_4

$$CH_4 + \tfrac{1}{2} O_2 \rightleftharpoons CO + 2 H_2 \qquad \Delta H_R = -36 \text{ kJ mol}^{-1}, \qquad (1.1)$$

$$CH_4 + 2 O_2 \rightleftharpoons CO_2 + 2 H_2O \qquad \Delta H_R = -802 \text{ kJ mol}^{-1}, \qquad (1.2)$$

Steam reforming

$$CH_4 + H_2O \rightleftharpoons CO + 3 H_2 \qquad \Delta H_R = +206 \text{ kJ mol}^{-1} \qquad (7.1)$$

$$CO + H_2O \rightleftharpoons CO_2 + H_2 \qquad \Delta H_R = -40.9 \text{ kJ mol}^{-1} \qquad (7.2)$$

$$CH_4 + 2 H_2O \rightleftharpoons CO_2 + 4 H_2 \qquad \Delta H_R = +165 \text{ kJ mol}^{-1} \qquad (7.3)$$

Carbon oxidation[127]

$$2 C + O_2 \rightleftharpoons 2 CO \qquad \Delta H_R = -221.0 \text{ kJ mol}^{-1} \qquad (7.4)$$

$$C + O_2 \rightleftharpoons CO_2 \qquad \Delta H_R = -393.5 \text{ kJ mol}^{-1} \qquad (7.5)$$

$$C + H_2O \rightleftharpoons CO + H_2 \qquad \Delta H_R = +131.3 \text{ kJ mol}^{-1} \qquad (5.3)$$

CO_2 dissociation

$$CO_2 \rightleftharpoons CO + \tfrac{1}{2} O_2 \qquad \Delta H_R = +283.17 \text{ kJ mol}^{-1} \qquad (7.6)$$

Boudouard-Equilibrium:

$$2 CO \rightleftharpoons C + CO_2 \qquad \Delta H_R = -172.5 \text{ kJ mol}^{-1} \qquad (7.7)$$

Carbon deposition from CH_4

$$CH_4 \rightleftharpoons C + 2 H_2 \qquad \Delta H_R = +74.9 \text{ kJ mol}^{-1} \qquad (7.8)$$

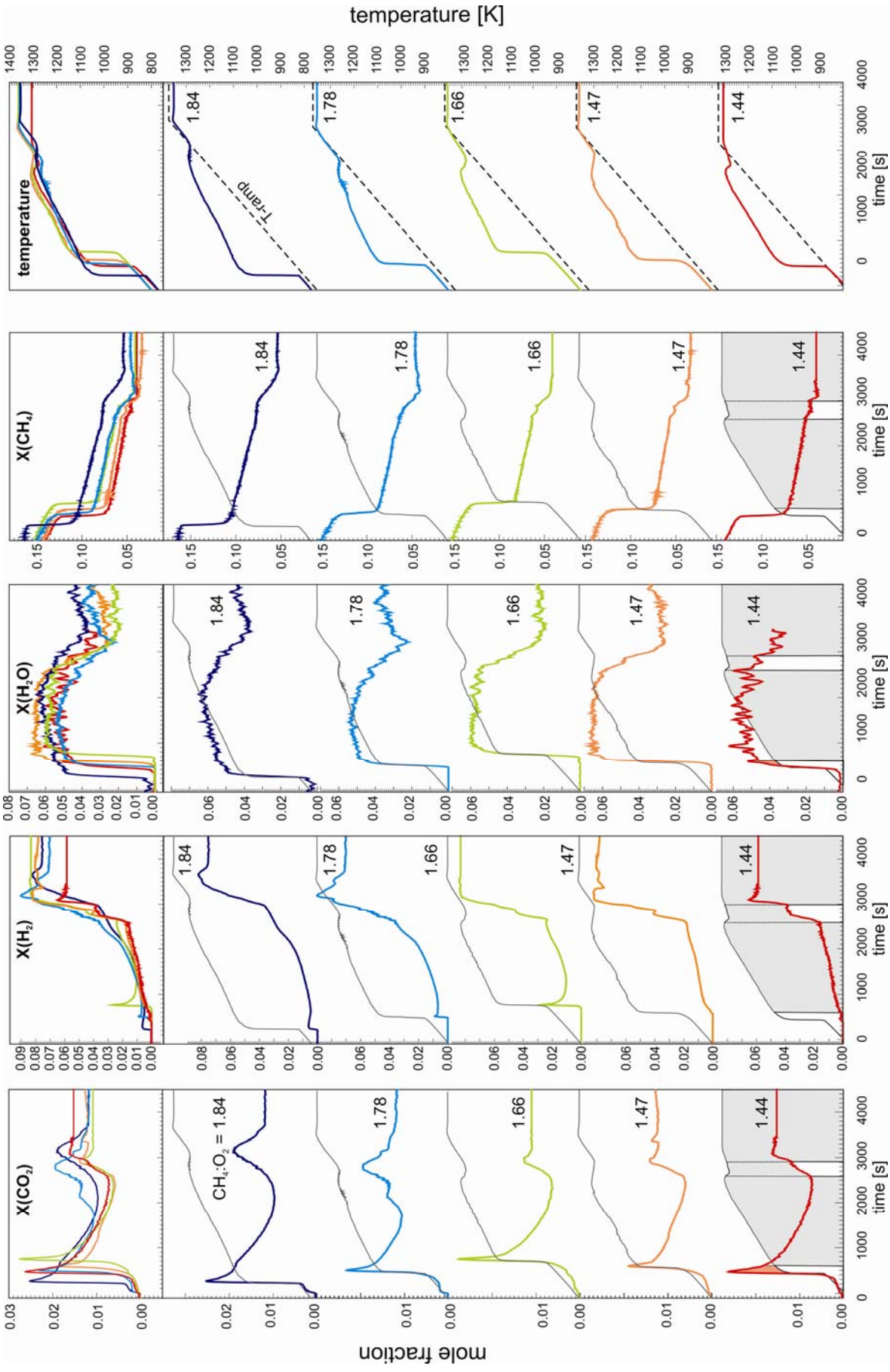
temperature [K]
temperature
T-ramp
1.84
1.78
1.66
1.47
1.44
X(CO2)
X(H2)
X(H2O)
X(CH4)
CH4:O2 = 1.84
mole fraction
time [s]

Figure 7.2: Mass spectra of CO_2, H_2, H_2O, CH_4, and temperature during CPO of methane at different CH_4/O_2 ratios in a Pt-tube. Dilution is 75 % Ar and the total flow of 0.4712 slpm corresponds to a velocity of 10 m s^{-1}. In the last series of plots not only the temperature at the tube entrance is shown but also the temperature ramp of the furnace. At least four reaction pathways can be observed. First combustion (forming of CO_2 and water), followed by CPO indicated by H_2 increase, third steam reforming, and finally carbon deposition. Cooling down the curve show the same behaviour. At this conditions O_2 break through occurred.

a) CPO at the CH_4/O_2 Ratio between 1.44 and 1.84

Figure 7.2 shows the mole fractions of CO_2 (first column), H_2 (second column), H_2O (third column), CH_4 (fourth column), and the temperature of the product gas (fifth column) during furnace heating of the reactor, and ignition. The lines contain the different CH_4/O_2 ratios, starting with the compilation at the top; the individual mixtures are given in the following lines starting with $CH_4/O_2 = 1.84$. In order to see the influence of the temperature of the product gas, it is included in each graph. For better visualisation, only the heating ramp is displayed. The cooling down of the system showed exactly the same behaviour, which can be seen in Figure 3.8. Despite the correction of the mole fractions of O_2 and CO described in chapter 3.5.2, the error is still large. Therefore, both mole fractions are not shown. Since there is a high thermal conductivity along the platinum tube, a constant temperature distribution in the reactor can be assumed leading to the assumption of a quasi steady state at each time point.

The results compiled in Figure 7.2 are consistent with the existence of four different pathways of the oxidation of CH_4. First, during ignition oxidation of CH_4 takes place for all ratios. This explains the sudden increase in the formation of CO_2 and H_2O combined with the consumption of CH_4 and the absence of the formation of H_2. As this reaction is highly exothermic, the temperature rises by approximately 200 K to approximately 1100 K. This leads to the partial oxidation of CH_4 forming CO and H_2. This reaction is less exothermic than the combustion and thermodynamically favoured at higher temperatures. The enhanced formation of CO (not shown) is coincident with the decrease of the formation of CO_2.

Temperatures of the external furnace of approximately 1250 K and a temperature of the product gas of approximately 1300 K give rise to a second major formation of CO_2 and H_2 coincident with a decrease of the formation of H_2O caused by the steam reforming reactions. The endothermic reaction and consumed heat leading to a temperature drop of approximately 50 K. At the entrance of the Pt-tube, O_2 is available and combustion providing water occurs all the time. The length of the tube (nearly 4 cm) is sufficient for steam reforming taking place further downstream. Comparing the different inlet conditions one can clearly recognise that the steam reforming of CH_4 becomes more and more important, when the partial pressure of CH_4 is increased. At temperatures in the range of 700 K, carbon deposition starts also forming H_2. However, the produced carbon reacts with H_2O in a water-gas shift reaction forming CO and H_2. This reaction becomes predominant

when the furnace is heated up to 1350 K and explains the increase in H_2 at these temperatures.

b) CPO at the CH_4/O_2 Ratio between 1.90 and 3.00

Further increase in the CH_4/O_2 ratio leads to a complex reaction dynamics. In a wide range of temperatures of the furnace, no steady state was observed, oscillation occurred instead. Actually, the shape and frequency did not depend on the CH_4/O_2 ratio; during heating up and cooling down, however, differences in shape and frequency occurred. One example ($CH_4/O_2 = 1.99$) of complete curves for temperature of the product gas and the molar fractions of the most important species during heating and cooling is depicted in Figure 7.3. The top area shows the compilation of molar fractions and temperature and for better visualisation the molar fraction of each species is zoomed in at interesting furnace temperatures.

Firstly, it is worthwhile to mention, that the results are far away from thermodynamic equilibrium and that shape, intensity and frequency of the oscillations indicate self-sustaining patterns of interactions between the processes responsible for the oscillations. It seems that carbon or graphite islands on the surface have an important impact on the oscillatory behaviour. During experiments performed using a brand new tube, oscillations with a high frequency (three in a minute) occurred already at a CH_4/O_2 ratio of 1.4, during experiments performed using a tube with aged surfaces, oscillations only occurred at higher CH_4/O_2 ratios as described here. This observation is consistent with the assumption that the surface of the Pt-tube has been modified due to the deposition of some C(s) species, which could not be removed even by oxidation in pure O_2 at 1300 K for several hours. In the literature, active and passive species of C(s) are well known. In Somorjai's model [128, 129] the catalyst is still active, although the surface can be covered up to 95% by irremovable modifications of carbon. The unchanged activity of the catalyst implies that the deposited carbon either is highly porous leading to a fast diffusion of the methane and oxygen to the metal surface or exhibits active sites similar to those of the platinum surface.

In literature, two main mechanisms discussed, describing dynamic instabilities in surface reactions.[122] The first one describes nonisothermal systems, where any exothermic reaction has the potential for exhibiting bistable or oscillatory behaviour as well as developing spatial patterns when coupled with transport mechanism. The occurrence of these thermo-kinetic oscillations depends on the operating conditions. The exothermic reaction leads to a temperature increase accelerating the reaction rates, which are restrained, e.g., by a temporarily almost complete consumption of one or more reactants. Although the CPO of CH_4 involves exothermic reactions, this model cannot really explain in detail the oscillations observed in a flow reactor. Therefore, the impact of changes in the surface structure on the reactions seems to exceed that of transport phenomena.

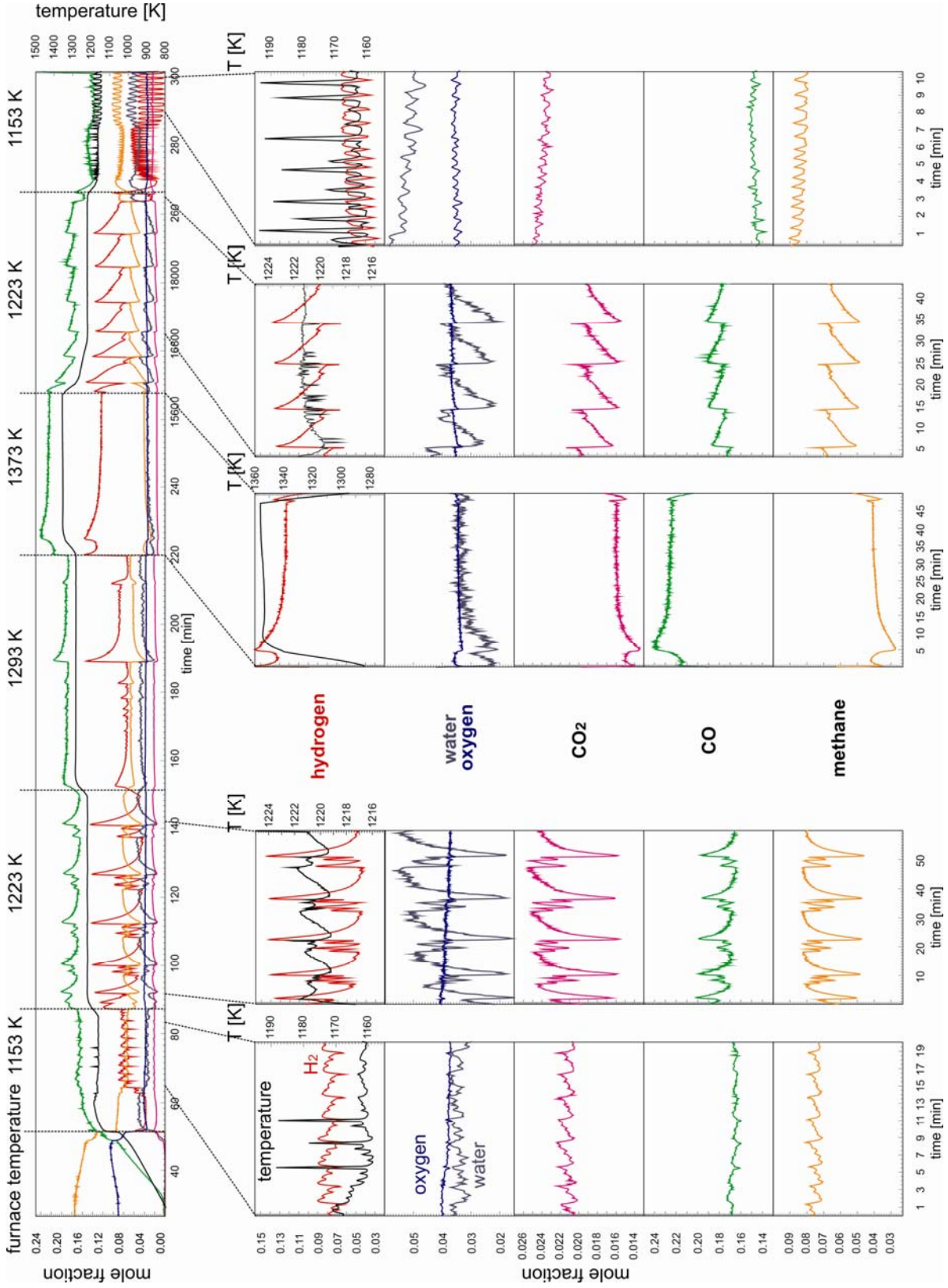

Figure 7.3: mass spectrum of the CPO of methane at a CH_4/O_2 ratio of 1.99. The furnace is heated up in 10 K per minute until first oscillations occurred (1153 K). Then the furnace is heated up to 1223 K, 1293 K and 1373 K. The shape of the oscillations change when cooling down. The lower part shows a zoom of the mole fractions of H_2 , Water and O_2, CO_2, CO, and CH_4.CPO at the CH_4/O_2 Ratio between 1.90 and 3.00.

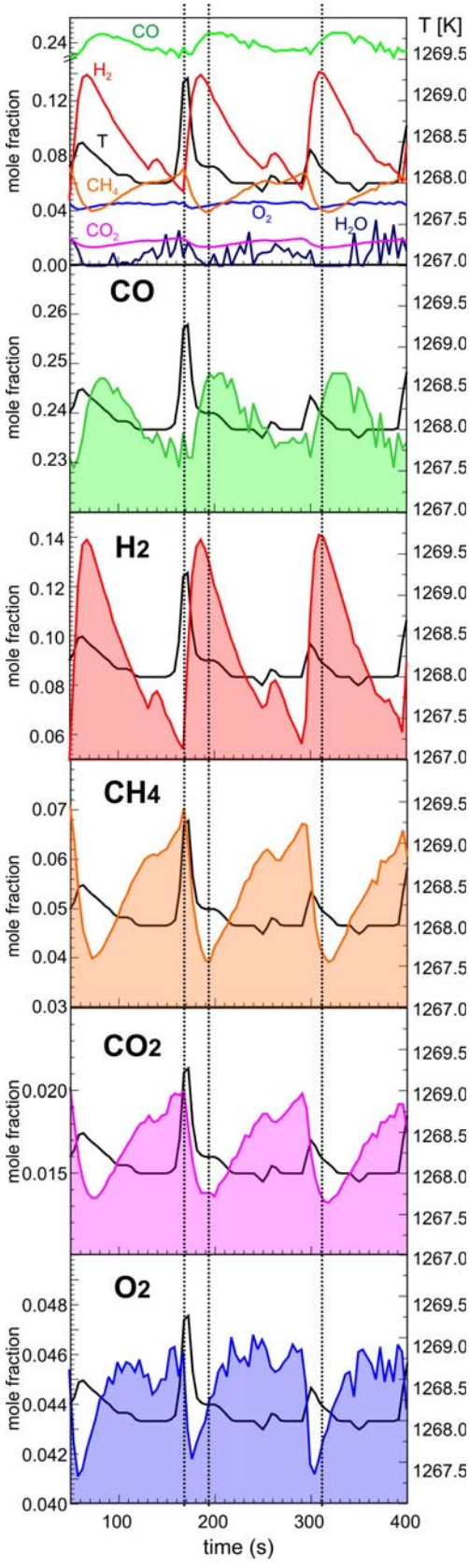

Figure 7.4: Rate oscillations at CH_4/O_2 = 2.1. Black line in each graph: Pt temperature. The furnace temperature is 950 °C. For better visualisation each species is plotted in a separate graph.

The second model applies for isothermal systems. Bistable behaviour can occur whenever the adsorbing gases have different site requirements. For example CO and O_2 show oscillations on Pt(110) based on surface phase transitions due to adsorption. For instance, the clean Pt(110) surface is reconstructed in a missing row manner, exhibiting a 1×2 LEED pattern. Adsorption of 0.5 ML of CO lifts the reconstruction completely, and a 1×1 LEED pattern structure is established. This structure has a higher sticking probability for O preventing further increase in the coverage with CO. Most of the adsorbed CO will be consumed by the reaction and leave the surface as CO_2. As soon as the coverage of CO drops again beneath about 0.5 ML the reconstruction of the surface sets in, reducing the sticking probability for O to the old value so that CO-adsorption dominates once more. However, even if the experiments carried out in this work are quasi isothermal, because of the high heat loss, a surface reconstruction as in the case of CO oxidation is unlikely.

The rate oscillations observed during the work reported here, are probably due to modifications of the catalyst surface. Apparently, carbon deposition and carbon removal by oxidation have a major influence on the rate of the partial catalytic oxidation of methane. An explanation could be as follows:

When the oscillation cycle starts at temperatures above 1150 K (Figure 7.4), the surface is free of any carbon. Therefore, the exothermic CH_4 oxidation reactions will take place forming CO, CO_2, H_2, and H_2O. Nevertheless, these two reactions do not exclusively occupy the Pt(s)-sites. Steam reforming reactions occur and carbon deposition from CH_4 will be an additional pathway. Carbon

slowly covers the surface decreasing the possibility for CH_4 to contact and react with the active sites on the surface and the remaining concentration of CH_4 increases. However, close to the entrance of the Pt-tube (about 3 mm) total oxidation occurs all the time forming CO_2 and H_2O, serving as possible reactants further downstream. With increasing formation of C(s), the *Boudouard*-reaction is enhanced. This is indicated by the fact that the maximum of the conversion of CH_4 (minimum in CH_4 mole fraction) is coincident with the maximum of the production of CO and corresponds to a minimum of CO_2 consumed by the *Boudouard*-reaction. At atmospheric pressure and temperatures above 950 K the *Boudouard*-equilibrium in fact favours the formation of CO. Only if all solid carbon is consumed the CO/CO_2 is determined by the dissociation of CO_2. Since even at high temperatures this equilibrium favours the formation of CO_2, CO_2 will be formed.[130] Due to the pyrolysis of methane on the surface, the formation of H_2 reaches its maximum, too.

The experimental data do not permit to decide, whether the deposition and oxidative removal of carbon change the structure of the surface of the Pt in such a way that the sticking probability of the molecules decreases or carbon islands simply block the surface and thus prevent the contact of the gaseous reactants with the metal surface. In both cases, the conversion of methane decreases, as the formed carbon decreases the possibility for CH_4 to contact and react with the active sites on the surface. That means CH_4 passes through the Pt tube without reaction. In addition, as more carbon is formed less active sites for CO_2 or O_2 are left. However, it seems that now the most favoured adsorption species is O(s), which slowly oxidises C(s) to CO_2, freeing more and more vacancies. As mentioned above, graphite can diffuse on the surface keeping the free vacancies constant. Therefore, the conversion of O_2 does not change until a critical coverage with carbon is reached. Again, it is not clear, whether the sharp temperature peak before the cycle starts is due to a change of the surface structure to a situation, in which no carbon is left or due to a sudden complete exothermic oxidation of the carbon by O(s) when a critical amount of surface vacancies is reached. In some way, the initial state of the surface is restored and the cycle restarts.

An overview on the oscillatory behaviour of the catalytic partial oxidation of methane under all conditions applied in the present work is compiled in Figure 7.5. Since in all cases the shapes of the curves representing the concentrations of H_2, H_2O, O_2, CH_4, CO, and CO_2 were the same, only the molar fraction of H_2 is presented. Figure 7.3 reveals that the oscillating behaviour is very complex. The period of the oscillations differs from a couple of minutes per cycle up to nearly 45 min. It is rather difficult to find a trend depending on the CH_4/O_2 ratio. It seems that the time of the cycle increases with higher CH_4 values, which may be due to an enhancement of carbon deposition by a higher partial pressure of CH_4 combined with a slow down of the removal of deposited carbon with decreasing concentration of O_2.

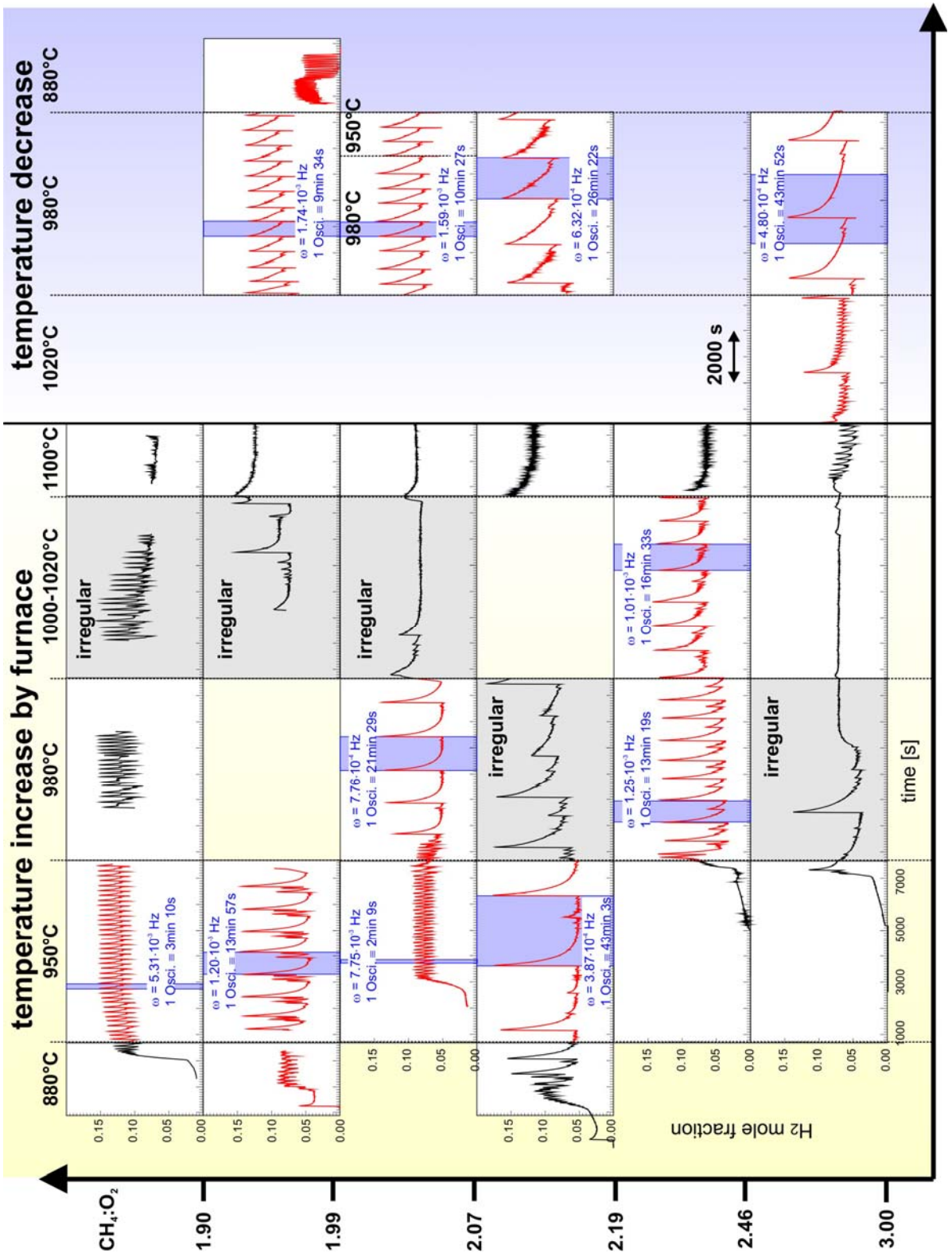

Figure 7.5: Oscillatory behaviour of the CPO of CH_4 at varying CH_4/O_2 ratios during heating up and down cooling of the reaction. Since H_2 is mostly affected by the oscillations only the H_2 mole fractions are depicted.

In between all conditions investigated in the present work, the oscillation stopped at a maximum temperature (1373 K). At temperatures exceeding this limit, the pyrolysis of CH_4 and the *Boudouard*-reaction dominate the overall process. In Figure 7.2 one can recognise that CH_4 and O_2 are converted nearly completely and the production of H_2 and CO reaches its maximum.

Additionally, the cycle time is different during heating up and down cooling (Figure 7.5), again due to a different structure of the surface. It seems that the shapes and structure of the carbon islands affect the oscillation, too. In general, two differences are obvious. Firstly, at a given temperature the reaction oscillates faster during down cooling than it does during heating up. Secondly, the shape changes: In case of heating up the peak for H_2 is very sharp followed by a strong exponential decay. While down cooling, the peak for H_2 is sharp, too, but the decrease is not so steep.

There are many questions left open. There is no satisfactory explanation for the small peaks occurring between two oscillation periods. In future work it will be necessary to have some surface imaging experiments to see how the surface really changes and which structures cause the oscillating behaviour. It will also be necessary to develop a detailed reaction mechanism, because the global reactions mentioned in this chapter can only give hints on the processes going on. There are no surface reaction mechanisms available in literature to describe those phenomena.

CHAPTER VIII

8 Conclusion and Outlook

The objective of this work was to study total and partial oxidation of methane over Pt, Pd, and Rh catalysts for a wide range of conditions. An experimental set-up, which is easily available for modelling and numerical simulation, was developed that also allows the study of transient processes such as light-off. The experimental data were used to evaluate surface-reaction schemes from literature and to improve them where necessary and possible. To compare experimentally derived and numerically predicted data, available numerical codes such as DETCHEM and Fluent were used. Crucial conditions, at which the models need improvement, were found.

Consequently, catalytic oxidation of methane covering a wide range of CH_4/O_2 volumetric ratios (lean mixtures with $CH_4/O_2 < 0.5$ as well as fuel-rich mixtures with $CH_4/O_2 > 0.5$) was studied using Pt, Pd, and Rh catalysts. First, the catalytic combustion in lean mixtures was investigated experimentally and numerically. The light-off of the reaction was studied as well as the kinetic behaviour for the hydrogen-assisted ignition. For these conditions, the reaction was studied experimentally and the results were compared with simulations for steady state and transient conditions. Furthermore, the interaction between homogeneous and heterogeneous reactions was investigated over platinum based catalysts and also rate oscillations caused by surface and bulk oxidation/reduction cycles over palladium based catalysts or carbon deposition and removal in a tubular platinum catalyst. In fuel-rich mixtures, the partial oxidation of CH_4 for the production of synthesis gas (H_2 and CO) competes with the total oxidation. This competition was explained in very detail, also for transient processes. The numerical analysis also included a study of the impact physical catalyst properties on the light-off behaviour.

In the experimental study, a flow reactor system with appropriate product analysis and temperature measurement was designed, set-up, and applied. The reactor consists of a 40 cm long quartz tube with varying inner diameters. A honeycomb catalyst coated with Rh, Pd, or Pt is placed inside. Two chemical inert monoliths are placed in front of and behind the catalyst and serve as radiation shields. An 1 mm thick ceramic cloth wound around the catalyst prevents gas bypass. The gas temperature at the exit of the catalytic monolith and outside the quartz tube is monitored using thermocouples. The reaction is ignited by heating up the reactor using a furnace. The gases are premixed at room temperature and flow into the quartz tube at atmospheric pressure. The product composition is determined by a quadrupole mass spectrometer (QMS), which also allows the study of transient phenomena.

For the evaluation of reaction mechanisms, detailed numerical simulations of the physical and chemical processes using the recently developed computer program package DETCHEM and the commercially available CFD code FLUENT are applied. The numerical codes take into account detailed mechanisms of surface and gas phase reactions as well as mass and heat transport processes in the channels and heat transport in the solid monolithic structure. The channels are simulated under steady-state conditions in three-dimensions by an elliptic approach using FLUENT and in two dimensions by a parabolic approach using $DETCHEM^{CHANNEL}$. Transient phenomena are simulated by $DETCHEM^{MONOLITH}$, which includes transient heat balances of the monolithic structure and two-dimensional, parabolic flow field simulations of a representative number of single channels.

The catalytic combustion of CH_4 was carried out on honeycomb monoliths coated with Pt (chapter 5.1). The transient ignition was simulated using a recently developed code $DETCHEM^{MONOLITH}$, including a detailed surface-reaction mechanism listed in Appendix A. The simulation matches the results of the experiment well. However, for concentrations of the CH_4 in the feed gas exceeding 4 vol.-%., gas-phase reactions become significant, resulting in the formation of some CO. This impact of homogeneous reaction on the heterogeneous reaction is described in chapter 5.3. Two-dimensional simulations of the entire monolith are carried out in addition, revealing in detail the physical and chemical processes occurring in the monolithic structure during the ignition. Under the given conditions, conversion starts at the rear end of the circumferentially sited channels, while the feed gas still cools the inner channels of the catalyst. The exothermic reaction then heats up the entire monolithic structure and conversion in the inner channels is initiated, again beginning at the rear end.

In some of these measurements, oscillating reaction rates were observed, which may be caused by the establishment of a flame in front of the reactor (Chapter 5.1). It may be formed at the entrance of the monolith and this burns the feed up stream until the cold wall is hit and the flame is extinguished. In all experiments, a flammable gas mixture was present. The varying exit gas-phase temperatures, at which the flames occurred (about 950 K for H_2 and 1150 K for CH_4), may be caused by the variation of the ignition

temperatures of the CH_4/air and H_2/air mixtures (~920 K and ~800 K, respectively). Again, the reaction starts in the catalyst channel and heats up the front radiation shield until the flame is ignited. It would be interesting to simulate these oscillations in future work. However, it would be necessary to use a code able to solve elliptical equations, because the boundary layer assumptions used in the present work do not meet the given conditions.

The addition of H_2 to catalytic combustion of methane on Pt is a promising way to easier ignite the reaction (Chapter 5.2). The energy needed to initiate the reaction is reduced by the presence of hydrogen, since the ignition temperature is considerably lower than the ignition temperature in the absence of hydrogen. Instead of adding pure H_2, part of the fuel could be partially oxidised to synthesis gas, which is then fed to the combustion mixture. However, the interactions between catalytic and gas-phase reactions are not completely understood yet and need some more experimental and in particular numerical investigations, because sudden gas-phase reactions can easily lead to explosions. Furthermore, the mechanism for the catalytic combustion of methane needs to be upgraded, because the influence of the combustion of H_2 on the desorption of CH_4 does not seem to fit perfectly.

A big challenge in kinetics is the verification of oscillating behaviour caused by surface processes. In chapter 5.4, the catalytic combustion of CH_4 on Pd is investigated. The oxidation and reduction of the catalyst (PdO $\rightleftharpoons$ Pd) causes changes in the rate of the combustion reaction. Pd sites next to chemically bound PdO are more reactive than sites next to oxygen adsorbed on Pd. The enhanced heat release causes the reduction of the bulk PdO to Pd, thus the surface is destabilised and forms only adsorbed O(s). This is less reactive for the oxidation of CH_4 and the surface cools down. This results in oxidation of the bulk, again forming PdO, and the cycle starts again. Although, these results show that the oscillatory behaviour can be explained by the surface model developed by Wolf et al. in principle, the model still has difficulties to represent the frequency of the oscillation.

Prior to investigation and simulation of the ignition of CPO of methane on monoliths coated with Rh (Chapter 6.2), a given reaction mechanism was made thermodynamic consistent regarding the overall reaction enthalpies and forward and reverse rate coefficients. Furthermore, the dependence of the activation energies for O(s) and CO(s) desorption on the coverage was taken into account. A three-dimensional steady-state simulation of a square channel was carried out including heat transport within the catalyst structure. The numerically predicted exit temperature, conversion, and selectivities agree well with the experimentally determined data. The 3D contour plots showed that the more exothermic total combustion occurred in the entrance region. Further downstream, O_2 is consumed completely and steam reforming takes place forming more H_2. Comparison of 3D with 2D-simulations showed no differences in overall conversion and selectivities predicted.

With a detailed reaction mechanism working reasonably well and with DETCHEM^{MONOLITH} as a program, coupling the reaction mechanism with a two-dimensional flow field and a two-dimensional heat balance of the solid monolith, the light

off and the influence of different support materials were investigated. In the experimental study and in the numeric simulation, alumina and cordierite served as support material. The results of experiment and simulation were compared, and the influence of the physical properties of the solid structure on the ignition was determined. In both cases, total oxidation of methane to carbon dioxide and water indicates the start of ignition. As ignition proceeds, the concentrations of hydrogen and carbon monoxide increase and the temperature rises. In case of alumina, the simulation revealed the movement of the reaction zone from the rear face to the front face of the monolith during ignition. A strong competition between direct partial oxidation, total oxidation, and steam reforming occurs in the reactor. Before ignition, oxygen completely covers the surface. At steady state, oxygen is the primary adsorbed species in the catalyst entrance region, where total oxidation occurs. Further downstream, the coverage with oxygen decreases rapidly, and steam reforming leads to an increase in the selectivity for the formation of synthesis gas. The ignition in a cordierite monolith was faster and started the front end of the catalyst. A series of simulations varying the physical properties of the catalyst (Chapter 6.2.3) showed that only the thermal conductivity λ has an influence on the region where ignition starts. Catalysts with a high λ ignite in the rear end and low λ causes a rapid ignition in the front end. The variation of the physical parameters c_p and ρ, indicates that the catalyst should have a small heat capacity, i.e., a small c_p and a small ρ for fast ignition. In order to prevent high temperature peaks, favouring sintering of the catalytically active material, the catalyst should have a high thermal conductivity; the requirement of a large catalytically active surface area is obvious.

A variety of current studies on catalysis focus on the application of nanoparticles as catalytic active components. Recent studies of Volpp et al. [59] showed that Rh nanoparticles prepared by laser ablation onto a support material are promising catalysts for the removal of NO_x from automotive exhaust gases at low temperatures, at which the commonly used catalysts have no effect. In this work, Rh nanoparticles were prepared and tested as catalysts for the CPO of CH_4 at high temperatures. However, the nanoparticles did not show any improvement for the CPO of methane. In fact, the monolith impregnated conventionally with a Rh salt solution showed the best results. This may be caused by a loss of the nanoparticles' high surface area during preparation of the catalyst. While suspending or slurring respectively the Rh particles in H_2O, the particles formed clusters. To preserve the high surface are it would be necessary to prepare the nanocatalysts in a different way, e.g., by laser ablation directly onto the support, or by addition of stabilising molecules to the liquid. Even if such efforts are successful, costly nanoparticle catalysts will only find applications if the sintering of the support or washcoat can be prevented.

For a better understanding of the kinetic behaviour of catalytic reactions, a tubular catalyst fully made out of platinum was used, which is even more well-defined regarding its numerical flow field treatment. The 37 mm long Pt tube with an inner diameter of 1 mm

was first applied for the oxidation of CO at varying flow velocity, CO/O_2 ratio and argon dilution. The ignition and extinction temperatures as well as the conversion of CO were determined. The experiments showed clearly that CO adsorption controls the kinetics of this heterogeneous reaction. The coverage with CO influences the overall oxidation, which is recognised by the hysteresis between the ignition and extinction temperatures, with the second one always being lower. While heating up the system, the surface is mainly covered by CO, which blocks the adsorption of O_2 if the coverage with CO exceeds about 0.4. For adsorption, O_2 needs two vacancies sited close to each other. While the reaction is ignited, there is always some O_2 on the surface implying that the reactor has to cool down below the ignition temperature to extinguish the reaction. Then the critical coverage with CO (0.4) is reached and CO is inhibiting the adsorption of O_2.

Finally, the CPO of CH_4 at high temperatures was carried out in the Pt-tube. The CH_4/O_2 ratio was varied between 1.4 and 3.0 at a constant dilution with Ar of 75%. The furnace was heated to 1373 K at a heating rate of 5 K min^{-1}. Since there is a huge heat loss due to radiation and the high heat conductivity of Pt, the reaction could be assumed to be quasi steady state at each temperature for CH_4/O_2-ratios ranging up to 1.8. In the experiments, four main reaction pathways, occurring at different temperatures, could be recognised. First total combustion occurred followed by CPO, then steam reforming, and carbon deposition. Cooling down showed the same behaviour. At CH_4/O_2-ratios exceeding 1.9, oscillations occurred at certain temperatures, which may be due to competition between carbon deposition on the surface and its removal by oxidation. However, it will be necessary to focus on surface analysis as well as on the development of a detailed reaction mechanism including deposition and oxidative removal of carbon in order to understand the reactions in the Pt tube completely.

The work presented here showed that the combination of detailed experimental studies with numeric simulations based on reaction mechanisms based on the molecular behaviour and appropriate transport models, does not only help to understand the reactor behaviour at steady-state conditions but also at transient operation. The total and partial oxidation of methane over Pt, Pd, and Rh catalysts for a wide range of conditions was studied. An experimental setup was configured to match the needs for modelling and numerical simulations. In fact, it was not only possible to evaluate the catalytic combustion mechanism on Pt but also to improve and evaluate the surface reaction mechanism for the CPO of CH_4 by comparing experimentally derived and numerically predicted data. In addition, the light-off of both reactions was studied experimentally and numerically the first time. These numerical tools helped to reveal the kinetic behaviour by addition of H_2 to a combustion mixture. Furthermore, some crucial conditions were found, where the models break down and further model development is needed. So far, the active catalytic surface area used in the simulation is a roughly estimated parameter. More detailed determination of this value may substantially improve the simulation results.

APPENDIX

Appendix A: Gas-Phase and Surface-Reaction Mechanisms

Table 9: Gas-phase reaction mechanism for methane combustion [131]

1.	**H_2-O_2 React. (no HO_2, H_2O_2)**				**A [cm, mol, s]**	**β**	**E_A [kJ mol^{-1}]**
O_2	+ H		$\rightleftharpoons$ OH	+ O	$2.000E^{+14}$	0.0	70.300
H_2	+ O		$\rightleftharpoons$ H	+ H	$5.060E^{+04}$	2.670	26.300
H_2	+ OH		$\rightleftharpoons$ H_2O	+ H	$1.000E^{+08}$	1.600	13.800
OH	+ OH		$\rightleftharpoons$ H_2O	+ O	$1.500E^{+09}$	1.140	0.420
2.	**Recombination Reactions**						
H	+ H	+ M(1)	$\rightleftharpoons$ H_2	+ M(1)	$1.800E^{+18}$	-1.000	0.0
O	+ O	+ M(1)	$\rightleftharpoons$ O_2	+ M(1)	$5.400E^{+13}$	0.0	-7.4
H	+ OH	+ M(2)	$\rightleftharpoons$ H_2O	+ M(2)	$5.530E^{+22}$	-2.000	0.0
3.	**HO_2 Formation/Consumption**						
H	+ O_2	+ M(1)	$\rightleftharpoons$ HO_2	+ M(1)	$2.300E^{+18}$	-0.800	0.0
HO_2	+ H		$\rightleftharpoons$ OH	+ OH	$1.500E^{+14}$	0.0	4.200
HO_2	+ H		$\rightleftharpoons$ H_2	+ O_2	$2.500E^{+13}$	0.0	2.900
HO_2	+ H		$\rightleftharpoons$ H_2O	+ O	$3.000E^{+13}$	0.0	7.200
HO_2	+ O		$\rightleftharpoons$ OH	+ O_2	$1.800E^{+13}$	0.0	-1.7
HO_2	+ OH		$\rightleftharpoons$ H_2O	+ O_2	$6.000E^{+13}$	0.0	0.0
4.	**H_2O_2 Formation/Consumption**						
HO_2	+ HO_2		$\rightleftharpoons$ H_2O_2	+ O_2	$2.500E^{+11}$	0.0	-5.200
OH	+ OH	+ M(1)	$\rightleftharpoons$ H_2O_2	+ M(1)	$3.250E^{+22}$	-2.000	0.0
H_2O_2	+ H		$\rightleftharpoons$ H_2	+ HO_2	$1.700E^{+12}$	0.0	15.700
H_2O_2	+ O		$\rightleftharpoons$ OH	+ HO_2	$9.630E^{+06}$	2.0	16.630
H_2O_2	+ OH		$\rightleftharpoons$ H_2O	+ HO_2	$5.400E^{+12}$	0.0	4.200
5.	**CO Reactions**						
CO	+ OH		$\rightleftharpoons$ CO_2	+ H	$6.000E^{+06}$	1.500	-3.100

CO	+ HO_2		⇌ CO_2	+ OH		$1.500E^{+14}$	0.0	98.700
CO	+ O	+ M(1)	⇌ CO_2	+ M(1)		$7.100E^{+13}$	0.0	-19.000
CO	+ O_2		⇌ CO_2	+ O		$2.500E^{+12}$	0.0	200.000
6. CH Reactions								
CH	+ O		⇌ CO	+ H		$4.000E^{+13}$	0.0	0.0
CH	+ O_2		⇌ CHO	+ O		$3.000E^{+13}$	0.0	0.0
CH	+ CO_2		⇌ CHO	+ CO		$3.400E^{+12}$	0.0	2.900
CH	+ H_2O		⇌ CH_2O	+ H		$4.560E^{+12}$	0.0	-3.200
CH	+ H_2O		⇌ $3CH_2$	+ OH		$1.140E^{+12}$	0.0	-3.200
CH	+ OH		⇌ CHO	+ H		$3.000E^{+13}$	0.0	0.0
7. CHO Reactions								
CHO	+M(1)		⇌ CO	+ H	+M(1)	$4.500E^{+14}$	0.0	66.000
CHO	+H		⇌ CO	+ H_2		$9.000E^{+13}$	0.0	0.0
CHO	+O		⇌ CO	+ OH		$3.000E^{+13}$	0.0	0.0
CHO	+O		⇌ CO_2	+ H		$3.000E^{+13}$	0.0	0.0
CHO	+OH		⇌ CO	+ H_2O		$1.000E^{+14}$	0.0	0.0
CHO	+ O_2		⇌ CO	+ HO_2		$3.000E^{+12}$	0.0	0.0
CHO	+ CHO		⇌ CH_2O	+ CO		$3.000E^{+13}$	0.0	0.0
CHO	+ M(1)		⇌ CO	+ H	+M(1)	$4.500E^{+14}$	0.0	66.000
8. CH_2 Reactions								
$3CH_2$	+ H		⇌ CH	+H_2		$6.000E^{+12}$	0.0	-7.500
$3CH_2$	+ O		→ CO	+H	+H	$7.600E^{+13}$	0.0	0.0
$3CH_2$	+ $3CH_2$		⇌ C_2H_2	+ H_2		$1.200E^{+13}$	0.0	3.4
$3CH_2$	+ $3CH_2$		⇌ C_2H_2	+ H	+ H	$1.100E^{+14}$	0.0	3.4
$3CH_2$	+ CH_3		⇌ C_2H_4	+ H		$4.200E^{+13}$	0.0	0.0
$3CH_2$	+ O_2		⇌ CO	+ OH	+ H	$1.300E^{+13}$	0.0	6.200
$3CH_2$	+ O_2		⇌ CO_2	+ H_2		$1.200E^{+13}$	0.0	6.200
$1CH_2$	+ M(1)		⇌ $3CH_2$	+ M(1)		$1.200E^{+13}$	0.0	0.0
$1CH_2$	+ O_2		⇌ CO	+ OH	+ H	$3.100E^{+13}$	0.0	0.0
CH_3	+ H		⇌ $1CH_2$	+ H_2		$6.000E^{+13}$	0.0	63.2
$3CH_2$	+ O		⇌ CO	+ H_2		$4.400E^{+13}$	0.0	0.0
$3CH_2$	+ H		⇌ CH	+ H_2		$6.000E^{+12}$	0.0	-7.500
9. CH_2O Reactions								
CH_2O	+ M(1)		⇌ CHO	+ H	+ M(1)	$1.400E^{+36}$	-5.54	404.580
CH_2O	+ H		⇌ CHO	+ H_2		$1.270E^{+08}$	1.62	9.000
CH_2O	+ O		⇌ CHO	+ OH		$4.150E^{+11}$	0.57	11.600
CH_2O	+ OH		⇌ CHO	+ H_2O		$3.400E^{+09}$	1.18	-1.870
CH_2O	+ HO_2		⇌ CHO	+ H_2O_2		$3.000E^{+12}$	0.0	54.7
CH_2O	+ CH_3		⇌ CHO	+ CH_4		$7.830E^{-08}$	6.1	8.200
CH_2O	+ O_2		⇌ CHO	+ HO_2		$6.000E^{+13}$	0.0	170.700
CH_2O	+ M(1)		⇌ H_2	+ CO	+ M(1)	$3.250E^{+36}$	-5.54	404.580
10. CH_3 Reactions								
CH_3	+ M(1)		⇌ $3CH_2$	+ H	+ M(1)	$1.000E^{+16}$	0.0	379.000
CH_3	+ M(1)		⇌ CH	+ H_2	+ M(1)	$6.900E^{+14}$	0.0	345.03
$1CH_2$	+ CH_3		⇌ C_2H_4	+ H		$1.600E^{+13}$	0.00	-2.38
CH_3	+ O		⇌ CH_2O	+ H		$8.430E^{+13}$	0.0	0.0
CH_4	+ M(4)		⇌ CH_3	+ H	+ M(4)	$2.400E^{+16}$	0.000	439.00
				LOW		$1.290E^{+18}$	0.000	379.97
				TROE		0.000 1350.0	1.0	7830.0
CH_3	+ OH		→ CH_3O	+ H		$4.000E^{+14}$	0.0	64.8
CH_3O	+ H		→ CH_3	+ OH		$4.750E^{+16}$	-0.13	88.0
CH_3	+ OH		⇌ $1CH_2$	+ H_2O		$3.000E^{+13}$	0.0	11.64
CH_3	+ O_2		⇌ CH_2O	+ OH		$1.700E^{+11}$	0.0	37.400

CH_3 + HO_2		⇌ CH_3O	+ OH		$1.600E^{+13}$	0.0	0.0
CH_4 + O_2		⇌ CH_3	+ HO_2		$3.900E^{+13}$	0.0	238.0
CH_3 + CH_3	+ M(1)	⇌ C_2H_6	+ M(1)		$3.610E^{+13}$	0.000	0.00
			LOW	$3.630E^{+41}$	-7.000	11.60	
			TROE	0.620	73.01180.0	0.0	
11a. CH_3O Reactions							
CH_3O + M(1)		⇌ CH_2O	+ H	+ M(1)	$5.000E^{+13}$	0.0	105.0
CH_3O + H		⇌ CH_2O	+ H_2		$1.800E^{+13}$	0.0	0.0
CH_3O + O_2		⇌ CH_2O	+ HO_2		$3.000E^{+10}$	0.0	8.9
CH_2O + CH_3O		⇌ CH_3OH	+ CHO		$1.150E^{+11}$	0.0	5.2
CH_3O + O		→ O_2	+ CH_3		$1.320E^{+13}$	0.0	0.0
CH_3 + O_2		→ O	+ CH_3O		$0.600E^{+14}$	0.0	131.0
CH_3O + O		⇌ OH	+ CH_2O		$1.800E^{+12}$	0.0	0.0
CH_3O + OH		⇌ CH_2O	+ H_2O		$1.810E^{+13}$	0.0	0.0
11b. CH_2OH Reactions							
CH_2OH + M(1)		⇌ CH_2O	+ H	+ M(1)	$5.000E^{+13}$	0.0	105.0
CH_2OH + H		⇌ CH_2O	+ H_2		$3.000E^{+13}$	0.0	0.0
CH_2OH + O_2		⇌ CH_2O	+ HO_2		$1.570E^{+15}$	-1.0	0.0
CH_2OH + O_2		⇌ CH_2O	+ HO_2		$7.230E^{+13}$	0.0	14.97
CH_2OH + H		⇌ CH_3	+ OH		$1.000E^{+13}$	0.0	0.0
12. CH_3O_2 Reactions							
CH_3 + O_2	+ M(1)	⇌ CH_3O_2	+ M(1)		$7.800E^{+08}$	1.2	0.0
			LOW	$1.650E^{+26}$	-3.300	0.0	
			TROE	0.495	2325.5	10.0	0.0
CH_3O_2 + CH_2O		⇌ CH_3O_2H	+ CHO		$0.130E^{+12}$	0.0	37.7
CH_3O_2 + CH_3		⇌ CH_3O	+ CH_3O		$1.500E^{+13}$	0.0	-5.0
CH_3O_2 + HO_2		⇌ CH_3O_2H	+ O_2		$2.400E^{+11}$	0.0	-6.6
CH_3O_2 + CH_3O_2		→ CH_2O	+ CH_3OH	+ O_2	$2.800E^{+10}$	0.0	-3.3
CH_3O_2 + CH_3O_2		→ CH_3O	+ CH_3O	+ O_2	$2.700E^{+10}$	0.0	-3.3
13. CH_4 Reactions							
CH_4 + H		⇌ H_2	+ CH_3		$1.330E^{+04}$	3.000	33.630
CH_4 + O		⇌ OH	+ CH_3		$6.900E^{+08}$	1.560	35.500
CH_4 + OH		⇌ H_2O	+ CH_3		$1.540E^{+07}$	1.830	11.600
CH_4 + HO_2		⇌ H_2O_2	+ CH_3		$1.000E^{+13}$	0.0	103.100
CH_4 + CH		⇌ C_2H_4	+ H		$3.000E^{+13}$	0.0	-1.700
CH_4 + $3CH_2$		⇌ CH_3	+ CH_3		$4.300E^{+12}$	0.0	42.000
14. CH_3OH Reactions							
CH_3 + OH	+ M(1)	⇌ CH_3OH	+ M(1)		$6.000E^{+13}$	0.000	0.00
			LOW	$4.560E^{+44}$	-8.200	0.00	
			TROE	0.820	20 0.0	1438.0	0.0
CH_3OH + H		⇌ CH_2OH	+ H_2		$3.100E^{+13}$	0.0	25.5
CH_3OH + H		⇌ CH_3O	+ H_2		$0.900E^{+13}$	0.0	25.5
CH_3OH + O		⇌ CH_2OH	+ OH		$3.880E^{+05}$	2.5	12.89
CH_3OH + O		⇌ CH_3O	+ OH		$1.300E^{+05}$	2.5	20.92
CH_3OH + OH		⇌ CH_2OH	+ H_2O		$3.000E^{+04}$	2.65	-3.7
CH_3OH + OH		⇌ CH_3O	+ H_2O		$5.300E^{+03}$	2.65	-3.7
CH_3OH + HO_2		⇌ CH_2OH	+ H_2O_2		$0.620E^{+13}$	0.0	81.1
CH_3OH + CH_3		⇌ CH_4	+ CH_2OH		$3.190E^{+01}$	3.17	30.0
CH_3OH + CH_3		⇌ CH_4	+ CH_3O		$1.410E^{+01}$	3.1	29.0
CH_3O + CH_3OH		⇌ CH_2OH	+ CH_3OH		$1.500E^{+12}$	0.0	29.3
CH_3OH + CH_2O		⇌ CH_3O	+ CH_3O		$0.153E^{+13}$	0.0	333.2
CH_3OH + O_2		⇌ HO_2	+ CH_2OH		$2.050E^{+13}$	0.0	189.1
15. CH_3O_2H Reactions							

CH_3O_2H	$\rightleftharpoons CH_3O$	$+ OH$	$6.000E^{+14}$	0.0	177.1
$OH + CH_3O_2H$	$\rightleftharpoons H_2O$	$+ CH_3O_2$	$7.300E^{+11}$	0.0	-1.0
$O + CH_3O_2H$	$\rightleftharpoons OH$	$+ CH_3O_2$	$1.990E^{+13}$	0.0	19.90
$CH_3O_2 + H_2O_2$	$\rightleftharpoons CH_3O_2H$	$+ HO_2$	$2.400E^{+12}$	0.0	41.80
$CH_3O_2 + CH_4$	$\rightleftharpoons CH_3O_2H$	$+ CH_3$	$1.810E^{+11}$	0.0	77.80
$CH_3O_2 + CH_3OH$	$\rightleftharpoons CH_3O_2H$	$+ CH_2OH$	$1.810E^{+11}$	0.0	57.70
16. C_2H_3 Reactions					
$C_2H_3 + M(1)$	$\rightleftharpoons C_2H_2$	$+ H + M(1)$	$1.900E^{+14}$	0.000	166.3
		LOW	$1.000E^{+42}$	-7.500	190.4
		TROE	0.350 0.0	0.0	0.0
$C_2H_3 + OH$	$\rightleftharpoons C_2H_2$	$+ H_2O$	$5.000E^{+13}$	0.0	0.0
$C_2H_3 + H$	$\rightleftharpoons C_2H_2$	$+ H_2$	$1.200E^{+13}$	0.0	0.0
$C_2H_3 + O_2$	$\rightleftharpoons CH_2O$	$+ CHO$	$2.300E^{+12}$	0.0	-2.34
16. C_2H_4 Reactions					
$C_2H_4 + M(1)$	$\rightleftharpoons C_2H_2$	$+ H_2 + M(1)$	$7.500E^{+17}$	0.0	332.0
$C_2H_4 + M(1)$	$\rightleftharpoons C_2H_3$	$+ H + M(1)$	$0.850E^{+18}$	0.0	404.0
$C_2H_4 + H$	$\rightleftharpoons C_2H_3$	$+ H_2$	$0.540E^{+15}$	0.0	62.9
$C_2H_4 + O$	$\rightleftharpoons CHO$	$+ CH3$	$2.420E^{+06}$	2.08	0.0
$C_2H_4 + OH$	$\rightleftharpoons C_2H_3$	$+ H_2O$	$2.200E^{+13}$	0.0	24.9
17. C_2H_5 Reactions					
$C_2H_4 + H + M(1)$	$\rightarrow C_2H_5$	$+ M(1)$	$3.970E^{+09}$	1.280	5.40
		LOW	$6.980E^{+18}$	0.000	3.20
		TROE	0.760 40.0 1025.0		0.0
$C_2H_5 + M(1)$	$\rightarrow C_2H_4$	$+ H + M(1)$	$8.200E^{+13}$	0.000	166.80
		LOW	$3.400E^{+17}$	0.000	139.60
		TROE	0.750 97.0 1379.0		0.0
$C_2H_5 + H$	$\rightleftharpoons CH_3$	$+ CH_3$	$3.000E^{+13}$	0.0	0.0
$C_2H_5 + O_2$	$\rightleftharpoons C_2H_4$	$+ HO_2$	$1.100E^{+10}$	0.0	-6.3
$C_2H_5 + CH_3$	$\rightleftharpoons C_2H_4$	$+ CH_4$	$1.140E^{+12}$	0.0	0.0
$C_2H_5 + C_2H_5$	$\rightleftharpoons C_2H_4$	$+ C_2H_6$	$1.400E^{+12}$	0.0	0.0
17. C_2H_6 Reactions					
$C_2H_6 + H$	$\rightleftharpoons C_2H_5$	$+ H_2$	$1.400E^{+09}$	1.5	31.1
$C_2H_6 + O$	$\rightleftharpoons C_2H_5$	$+ OH$	$1.000E^{+09}$	1.5	24.4
$C_2H_6 + OH$	$\rightleftharpoons C_2H_5$	$+ H_2O$	$7.200E^{+06}$	2.0	3.6
$C_2H_6 + HO_2$	$\rightleftharpoons C_2H_5$	$+ H_2O_2$	$1.700E^{+13}$	0.0	85.9
$C_2H_6 + O_2$	$\rightleftharpoons C_2H_5$	$+ HO_2$	$6.000E^{+13}$	0.0	217.0
$C_2H_6 + CH_3$	$\rightleftharpoons C_2H_5$	$+ CH_4$	$1.500E^{-07}$	6.0	25.4

Collision Efficiencies:

M(1)	$\rightarrow H_2$	$+ H_2O$	$+ O_2$	$+ CO$	$+ CO_2$	$+ CH_4$	
	1.0	6.5	0.4	0.75	1.5	3.0	
M(2)	$\rightarrow H_2$	$+ H_2O$	$+ O_2$	$+ CO$	$+ CO_2$	$+ CH_4$	
	1.0	6.5	0.4	0.75	1.5	0.66	
M(3)	$\rightarrow H_2$	$+ H_2O$	$+ O_2$	$+ Ar$	$+ CO$	$+ CO_2$	$+ CH_4$
	1.0	6.5	0.4	0.29	0.75	1.5	0.66

Kinetic data: $k = A \cdot T^{\beta} \cdot \exp(-E_A / RT)$, *A [cm, mol, s],* β *[-],* E_A *[kJ mol^{-1}],*

Table 10: CH_4-O_2 Surface-reaction mechanism for lean mixtures on Pt

1. ADSORPTION						**A [cm, mol, s]**	**β**	**E_a [kJ mol^{-1}]**
H_2	+Pt(s)	+Pt(s)	→ H(s)	+ H(s)		$0.046E^{-00}$	0.0	0.0
$Pt(s)						0.0	-1.0	0.0
H	+ Pt(s)		→ H(s)			$1.000E^{-00}$	0.0	0.0
O_2	+ Pt(s)	+ Pt(s)	→ O(s)	+ O(s)		$1.800E^{+21}$	-0.5	0.0
O_2	+ Pt(s)	+ Pt(s)	→ O(s)	+ O(s)		$2.300E^{-02}$	0.0	0.0
CH_4	+ Pt(s)	+ Pt(s)	→ CH_3(s)	+ H(s)		$1.000E^{-02}$	0.0	0.0
$Pt(s)						0.0	0.30	0.0
O	+Pt(s)		→ O(s)			$1.000E^{-00}$	0.0	0.0
H_2O	+Pt(s)		→ H_2O(s)			$0.750E^{+00}$	0.0	0.0
CO	+Pt(s)		→ CO(s)			$8.400E^{-01}$	0.0	0.0
$Pt(s)						0.0	1.0	0.0
2. DESORPTION								
H(s)	+ H(s)		→ Pt(s)	+ Pt(s)	+ H_2	$3.700E^{+21}$	0.0	67.4-6$\Theta_{H(s)}$
O(s)+ O(s)			→ Pt(s)	+ Pt(s)	+ O_2	$3.700E^{+21}$	0.0	213.0-60$\Theta_{O(s)}$
H_2O(s)			→ H_2O	+ Pt(s)		$1.000E^{+13}$	0.0	40.3
OH(s)			→ OH	+ Pt(s)		$1.000E^{+13}$	0.0	192.8
CO(s)			→ CO	+ Pt(s)		$1.000E^{+13}$	0.0	125.5
CO_2(s)			→ CO_2	+ Pt(s)		$1.000E^{+13}$	0.0	20.5
3. SURFACE REACTIONS								
O(s)	+ H(s)		⇌ OH(s)	+ Pt(s)		$3.700E^{+21}$	0.0	11.5
H(s)	+ OH(s)		⇌ H_2O(s)	+ Pt(s)		$3.700E^{+21}$	0.0	17.4
OH(s)	+ OH(s)		⇌ H_2O(s)	+ O(s)		$3.700E^{+21}$	0.0	48.2
CO(s)	+ O(s)		→ CO_2(s)	+ Pt(s)		$3.700E^{+21}$	0.0	105.0
C(s)	+ O(s)		→ CO(s)	+ Pt(s)		$3.700E^{+21}$	0.0	62.8
CO(s)	+ Pt(s)		→ C(s)	+ O(s)		$1.000E^{+18}$	0.0	184.0
CH_3(s)	+ Pt(s)		→ CH_2(s)	+ H(s)		$3.700E^{+21}$	0.0	20.0
CH_2(s)	+ Pt(s)		→ CH(s)	+ H(s)		$3.700E^{+21}$	0.0	20.0
CH(s)	+ Pt(s)		→ C(s)	+ H(s)		$3.700E^{+21}$	0.0	20.0

[a] *sticking coefficient*

Version 1.2, November 1995, O. Deutschmann, IWR, Heidelberg University,[33]

Kinetic data: $k = A \cdot T^{\beta} \cdot \exp\left(\frac{-E_A}{RT}\right)$, *A [cm, mol, s], β[-], E_A [kJ mol^{-1}], Nomenclature given in [35]*

$\Gamma = 2.72 \cdot 10^{-9}$ *mol cm^{-2}*

Table 11: Surface-reaction mechanism of CPO of methane on Rh, based on [15]

1.	ADSORPTION					A [cm, mol, s]	E_a [kJ mol^{-1}]
H_2	+ Rh(s)	+ Rh(s)	→ H(s)	+ H(s)		$1.000 \cdot 10^{-02}$	s.c.[a]
O_2	+ Rh(s)	+ Rh(s)	→ O(s)	+ O(s)		$1.000 \cdot 10^{-02}$	s.c.[a]
CH_4	+ Rh(s)		→ CH_4(s)			$8.000 \cdot 10^{-03}$	s.c.[a]
H_2O	+ Rh(s)		→ H_2O(s)			$1.000 \cdot 10^{-01}$	s.c.[a]
CO_2	+ Rh(s)		→ CO_2(s)			$1.000 \cdot 10^{-05}$	s.c.[a]
CO	+ Rh(s)		→ CO(s)			$5.000 \cdot 10^{-01}$	s.c.[a]
2.	**DESORPTION**						
H(s)	+ H(s)		→ Rh(s)	+ Rh(s)	+H_2	$3.000 \cdot 10^{+21}$	77.8
O(s)	+ O(s)		→ Rh(s)	+ Rh(s)	+O_2	$1.300 \cdot 10^{+22}$	$355.2\text{-}280\Theta_{O(s)}$
H_2O(s)			→ H_2O	+ Rh(s)		$3.000 \cdot 10^{+13}$	45.0
CO(s)			→ CO	+ Rh(s)		$3.500 \cdot 10^{+13}$	$133.4\text{-}15\Theta_{CO(s)}$
CO_2(s)			→ CO_2	+ Rh(s)		$1.000 \cdot 10^{+13}$	21.7
CH_4(s)			→ CH_4	+ Rh(s)		$1.000 \cdot 10^{+13}$	25.1
3.	**SURFACE REACTIONS**						
H(s)	+ O(s)		→ OH(s)	+ Rh(s)		$5.000 \cdot 10^{+22}$	83.7
OH(s)	+ Rh(s)		→ H(s)	+ O(s)		$3.000 \cdot 10^{+20}$	37.7
H(s)	+ OH(s)		→ H_2O(s)	+ Rh(s)		$3.000 \cdot 10^{+20}$	33.5
H_2O(s)	+ Rh(s)		→ H(s)	+ OH(s)		$5.000 \cdot 10^{+22}$	104.7
OH(s)	+ OH(s)		→ H_2O(s)	+ O(s)		$3.000 \cdot 10^{+21}$	100.8
H_2O(s)	+ O(s)		→ OH(s)	+ OH(s)		$3.000 \cdot 10^{+21}$	171.8
C(s)	+ O(s)		→ CO(s)	+ Rh(s)		$3.000 \cdot 10^{+22}$	97.9
CO(s)	+ Rh(s)		→ C(s)	+ O(s)		$2.500 \cdot 10^{+21}$	169.0
CO(s)	+ O(s)		→ CO_2(s)	+Rh(s)		$1.400 \cdot 10^{+20}$	121.6
CO_2(s)	+ Rh(s)		→ CO(s)	+ O(s)		$3.000 \cdot 10^{+21}$	115.3
CH_4(s)	+ Rh(s)		→ CH_3(s)	+ H(s)		$3.700 \cdot 10^{+21}$	61.0
CH_3(s)	+ H(s)		→ CH_4(s)	+ Rh(s)		$3.700 \cdot 10^{+21}$	51.0
CH_3(s)	+ Rh(s)		→ CH_2(s)	+ H(s)		$3.700 \cdot 10^{+24}$	103.0
CH_2(s)	+ H(s)		→ CH_3(s)	+ Rh(s)		$3.700 \cdot 10^{+21}$	44.0
CH_2(s)	+ Rh(s)		→ CH(s)	+ H(s)		$3.700 \cdot 10^{+24}$	100.0
CH(s)	+ H(s)		→ CH_2(s)	+ Rh(s)		$3.700 \cdot 10^{+21}$	68.0
CH(s)	+ Rh(s)		→ C(s)	+ H(s)		$3.700 \cdot 10^{+21}$	21.0
C(s)	+ H(s)		→ CH(s)	+ Rh(s)		$3.700 \cdot 10^{+21}$	172.8
CH_4(s)	+ O(s)		→ CH_3(s)	+ OH(s)		$3.700 \cdot 10^{+24}$	80.3
CH_3(s)	+ OH(s)		→ CH_4(s)	+ O(s)		$3.700 \cdot 10^{+21}$	24.3
CH_3(s)	+ O(s)		→ CH_2(s)	+ OH(s)		$3.700 \cdot 10^{+24}$	120.3
CH_2(s)	+ OH(s)		→ CH_3(s)	+ O(s)		$3.700 \cdot 10^{+21}$	15.1
CH_2(s)	+ O(s)		→ CH(s)	+ OH(s)		$3.700 \cdot 10^{+24}$	158.4
CH(s)	+ OH(s)		→ CH_2(s)	+ O(s)		$3.700 \cdot 10^{+21}$	36.8
CH(s)	+ O(s)		→ C(s)	+ OH(s)		$3.700 \cdot 10^{+21}$	30.1
C(s)	+ OH(s)		→ CH(s)	+ O(s)		$3.700 \cdot 10^{+21}$	145.5

[a] *sticking coefficient,* $\Gamma = 2.72 \cdot 10^{-9}$ *mol cm*$^{-2}$

Kinetic data: $k = A \cdot T^{\beta} \cdot \exp(-E_A / RT)$, *A [cm, mol, s],* $\beta = 0$, E_A *[kJ mol*$^{-1}$*],*

Table 12: Surface-reaction mechanism for methane combustion on Pd/PdO by Dr. Markus Wolf [90]

1.	**ADSORPTION**					**A [cm, mol, s]**	**β**	**E_A [kJ mol^{-1}]**
H_2	+ Pd(s)	+ Pd(s)	→ H(s)	+ H(s)		$7.00 \cdot 10^{-02}$	0.0	0.0
CH_4	+ Pd(s)	+ Pd(s)	→ CH_3(s)	+ H(s)		$3.20 \cdot 10^{-04}$	0.0	42.5
****@Pd(s)	5	→ 4				$1.00 \cdot 10^{-07}$	0.0	41.8
CH_4	+ VAC(B)	+ O(b)	→ CH_3(sp)	+ OH(b)		$1.00 \cdot 10^{-00}$	0.0	73.2
H_2	+ VAC(B)	+ O(b)	→ H(sp)	+ OH(b)		$7.00 \cdot 10^{-02}$	0.0	0.0
OH	+ VAC(B)		→ OH(b)			$1.00 \cdot 10^{-00}$	0.0	0.0
O	+ Pd(s)		→ O(Pd)			$1.00 \cdot 10^{-00}$	0.0	0.0
H	+ Pd(s)		→ H(s)			$1.00 \cdot 10^{-00}$	0.0	0.0
H_2O	+ Pd(s)		→ H_2O(s)			$7.50 \cdot 10^{-01}$	0.0	0.0
H_2O	+ VAC(B)		→ H_2O(b)			$1.00 \cdot 10^{-00}$	0.0	0.0
CH_2O	+ VAC(B)		→ CH_2O(s)			$1.00 \cdot 10^{-00}$	0.0	0.0
CO_2	+ VAC(B)		→ CO_2(b)			$5.00 \cdot 10^{-03}$	0.0	0.0
CO_2	+ Pd(s)		→ CO_2(s)			$5.00 \cdot 10^{-03}$	0.0	0.0
CO	+ Pd(s)		→ CO(s)			$9.60 \cdot 10^{-01}$	-1.4	0.0
2.	**DESORPTION**							
H(s)	+ H(s)		→ H_2	+ Pd(s)	+ Pd(s)	$5.71 \cdot 10^{+21}$	0.0	84.0-15$\Theta_{H(s)}$
CH_3(s)	+ H(s)		→ CH_4	+ Pd(s)	+ Pd(s)	$5.71 \cdot 10^{+21}$	0.0	41.8
CH_3(sp)	+ OH(b)		→ CH_4	+ VAC(B)	+ O(b)	$5.71 \cdot 10^{+21}$	0.0	147.5-230$\Theta_{VAC(B)}$
H(sp)	+ OH(b)		→ H_2	+ VAC(B)	+ O(b)	$5.71 \cdot 10^{+21}$	0.0	158.5-230$\Theta_{VAC(B)}$
O(Pd)			→ O	+ Pd(s)		$1.00 \cdot 10^{+13}$	0.0	364.0-57.5$\Theta_{O(Pd)}$
OH(b)			→ OH	+ VAC(B)		$1.00 \cdot 10^{+13}$	0.0	213.0-230$\Theta_{VAC(B)}$
H(s)			→ H	+ Pd(s)		$6.00 \cdot 10^{+13}$	0.0	259.4-7.5$\Theta_{H(s)}$
CO(s)			→ CO	+ Pd(s)		$1.00 \cdot 10^{+13}$	0.0	142.2
CO_2(b)			→ CO_2	+ VAC(B)		$1.00 \cdot 10^{+13}$	0.0	16.7
CO_2(s)			→ CO_2	+ Pd(s)		$1.00 \cdot 10^{+13}$	0.0	16.7
H_2O(s)			→ H_2O	+ Pd(s)		$1.00 \cdot 10^{+13}$	0.0	60.0
H_2O(b)			→ H_2O	+ VAC(B)		$1.00 \cdot 10^{+13}$	0.0	67.0
CH_2O(s)			→ CH_2O	+ VAC(B)		$1.00 \cdot 10^{+13}$	0.0	50.2
3.	**SURFACE REACTIONS**							
CH_3(s)	+ Pd(s)		→ CH_2(s)	+ H(s)		$5.71 \cdot 10^{+21}$	0.0	91.2
CH_2(s)	+ H(s)		→ CH_3(s)	+ Pd(s)		$5.71 \cdot 10^{+21}$	0.0	37.6
CH_2(s)	+ Pd(s)		→ CH(s)	+ H(s)		$5.71 \cdot 10^{+21}$	0.0	109.1
CH(s)	+ H(s)		→ CH_2(s)	+ Pd(s)		$5.71 \cdot 10^{+21}$	0.0	62.7
CH(s)	+ Pd(s)		→ C(s)	+ H(s)		$5.71 \cdot 10^{+21}$	0.0	20.9
C(s)	+ H(s)		→ CH(s)	+ Pd(s)		$5.71 \cdot 10^{+21}$	0.0	171.5
Oxygen provided only from the PdO phase								
CH_3(sp)	+ O(b)		→ CH_2(s)	+ OH(b)		$5.71 \cdot 10^{+21}$	0.0	56.9
CH_2(s)	+ OH(b)		→ CH_3(sp)	+ O(b)		$5.71 \cdot 10^{+21}$	0.0	20.9
CH_3(sp)	+ OH(b)		→ CH_2(s)	+ H_2O(b)		$5.71 \cdot 10^{+21}$	0.0	38.4
CH_2(s)	+ H_2O(b)		→ CH_3(sp)	+ OH(b)		$5.71 \cdot 10^{+21}$	0.0	20.9-230$\Theta_{VAC(B)}$
CH_3(s)	+ O(b)		→ CH_2(s)	+ OH(b)		$5.71 \cdot 10^{+21}$	0.0	16.7
CH_2(s)	+ OH(b)		→ CH_3(s)	+ O(b)		$5.71 \cdot 10^{+21}$	0.0	38.2-230$\Theta_{VAC(B)}$
CH_2(s)	+ O(b)		→ CH(s)	+ OH(b)		$5.71 \cdot 10^{+21}$	0.0	33.5
CH(s)	+ OH(b)		→ CH_2(s)	+ O(b)		$5.71 \cdot 10^{+21}$	0.0	62.2-230$\Theta_{VAC(B)}$
CH(s)	+ O(b)		→ C(s)	+ OH(b)		$5.71 \cdot 10^{+21}$	0.0	20.9
C(s)	+ OH(b)		→ CH(s)	+ O(b)		$5.71 \cdot 10^{+21}$	0.0	246.1-230$\Theta_{VAC(B)}$
O-, H-, C-Recombinations								
O(b)	+ H(s)		→ OH(b)	+ Pd(s)		$5.71 \cdot 10^{+21}$	0.0	78.7

OH(b)	+ Pd(s)	→ O(b)	+ H(s)	$5.71\cdot10^{+21}$	0.0	$153.2-230\Theta_{VAC(B)}$
H(sp)	+ O(b)	→ OH(b)	+ VAC(B)	$5.71\cdot10^{+21}$	0.0	78.7
OH(b)	+ VAC(B)	→ H(sp)	+ O(b)	$5.71\cdot10^{+21}$	0.0	$153.2-230\Theta_{VAC(B)}$
H chemistry on Pd(s)						
O(Pd)	+ H(s)	→ OH(s)	+ Pd(s)	$5.71\cdot10^{+21}$	0.0	$78.7-57.5\Theta_{O(Pd)}$
OH(s)	+ Pd(s)	→ O(Pd)	+ H(s)	$5.71\cdot10^{+21}$	0.0	95.7
H(s)	+ OH(s)	→ H_2O(s)	+ Pd(s)	$5.71\cdot10^{+21}$	0.0	60.0
H_2O(s)	+ Pd(s)	→ H(s)	+ OH(s)	$5.71\cdot10^{+21}$	0.0	146.0
OH(s)	+ OH(s)	→ H_2O(s)	+ O(Pd)	$5.71\cdot10^{+21}$	0.0	60.0
H_2O(s)	+ O(Pd)	→ OH(s)	+ OH(s)	$5.71\cdot10^{+21}$	0.0	$129.0-57.5\Theta_{O(Pd)}$
OH(b)	+ OH(b)	→ H_2O(b)	+ O(b)	$5.71\cdot10^{+21}$	0.0	60.0
H_2O(b)	+ O(b)	→ OH(b)	+ OH(b)	$5.71\cdot10^{+21}$	0.0	$78.5-230\Theta_{VAC(B)}$
OH(b)	+ OH(s)	→ H_2O(b)	+ O(Pd)	$5.71\cdot10^{+21}$	0.0	60.0
H_2O(b)	+ O(Pd)	→ OH(b)	+ OH(s)	$5.71\cdot10^{+21}$	0.0	$136.0-57.5\Theta_{O(Pd)}$
H(sp)	+ OH(b)	→ H_2O(b)	+ VAC(B)	$5.71\cdot10^{+21}$	0.0	60.0
H_2O(b)	+ VAC(B)	→ H(sp)	+ OH(b)	$5.71\cdot10^{+21}$	0.0	153.0
H(sp)	+ O(Pd)	→ OH(s)	+ VAC(B)	$5.71\cdot10^{+21}$	0.0	78.7
OH(s)	+ VAC(B)	→ H(sp)	+ O(Pd)	$5.71\cdot10^{+21}$	0.0	$95.7+57.5\Theta_{O(Pd)}$
CO(s)	+ O(b)	→ CO_2(b)	+ Pd(s)	$5.71\cdot10^{+21}$	0.0	$100.4-33.0\Theta_{CO(s)}$
CO_2(b)	+ Pd(s)	→ CO(s)	+ O(b)	$5.71\cdot10^{+21}$	0.0	$143.3+94.1\Theta_{O(b)}$
CO(s)	+ O(Pd)	→ CO_2(s)	+ Pd(s)	$5.71\cdot10^{+21}$	0.0	100.4
CO_2(s)	+ Pd(s)	→ CO(s)	+ O(Pd)	$5.71\cdot10^{+21}$	0.0	143.3
C(s)	+ O(b)	→ CO(s)	+ VAC(B)	$5.71\cdot10^{+21}$	0.0	25.1
CO(s)	+ VAC(B)	→ C(s)	+ O(b)	$5.71\cdot10^{+21}$	0.0	205.1
Including C(s) to Pd chemistry						
C(s)	+ O(Pd)	→ CO(s)	+ Pd(s)	$5.71\cdot10^{+21}$	0.0	25.1
CO(s)	+ Pd(s)	→ C(s)	+ O(Pd)	$5.71\cdot10^{+21}$	0.0	$205.1+94.1\Theta_{CO+O(Pd)}$
CH_2(s)	+ O(b)	→ CH_2O(s)	+ Pd(s)	$5.71\cdot10^{+21}$	0.0	25.1
CH_2O(s)	+ Pd(s)	→ CH_2(s)	+ O(b)	$5.71\cdot10^{+21}$	0.0	131.7
CH_2O(s)	+ O(b)	→ HCO(s)	+ OH(b)	$5.71\cdot10^{+21}$	0.0	37.7
HCO(s)	+ OH(b)	→ CH_2O(s)	+ O(b)	$5.71\cdot10^{+21}$	0.0	$136.0-230\Theta_{VAC(B)}$
HCO(s)	+ O(b)	→ CO(s)	+ OH(b)	$5.71\cdot10^{+21}$	0.0	0.0
CO(s)	+ OH(b)	→ HCO(s)	+ O(b)	$5.71\cdot10^{+21}$	0.0	$228.6-230\Theta_{VAC(B)}$
Sticking						
O_2	+ Pd(s) + Pd(s)	→ O(Pd)	+ O(Pd)	$8.00\cdot10^{-01}$	-0.5	0.0
O(Pd)	+ O(Pd)	→ Pd(s)	+ Pd(s) + O_2	$5.71\cdot10^{+21}$	0.0	$230.0-115.0\Theta_{O(Pd)}$
O(Pd)		→ O(b)		$5.00\cdot10^{+11}$	0.0	$80.0-115.0\Theta_{Pd(s)}$
O(b)		→ O(Pd)		$5.00\cdot10^{+11}$	0.0	$80.0+57.5\Theta_{O(Pd)}$
O_2(b)	+ VAC(B)	→ O(b)	+ O(b)	$5.71\cdot10^{+21}$	0.0	0.0
O(b)	+ O(b)	→ VAC(B)	+ O_2(b)	$5.71\cdot10^{+21}$	0.0	$65.0-230\Theta_{VAC(B)}$ $+57.5\Theta_{O2(B)}$
O_2(b)		→ O_2	+ VAC(B)	$1.00\cdot10^{+13}$	0.0	$50.0-57.5\Theta_{O2(s)}$ $-230\Theta_{VAC(B)}$
O_2	+ VAC(B)	→ O_2(b)		$1.00\cdot10^{+00}$	-0.5	0.0
O(b)	+ O(Pd)	→ O_2(b)	+ Pd(s)	$5.71\cdot10^{+21}$	0.0	$182.5-57.5\Theta_{O(Pd)}$ $-115.0\Theta_{Pd(s)}$
O_2(b)	+ Pd(s)	→ O(Pd)	+ O(b)	$5.71\cdot10^{+21}$	0.0	60.0
N_2	+ Pd(s)	→ N_2	+ Pd(s)	$1.00\cdot10^{+13}$	0.0	0.0

Index (s): Species on the surface, index (sp):, Index(b): Species in the bulk, VAC(B): free bulk vacancies
Kinetic data: $k = A \cdot T^{\beta} \cdot \exp(-E_A / RT)$*, A[cm, mol, s], β[-], E_A[kJ mol-1], Γ = $1.75\cdot10^{-9}$ mol cm^{-2}*

Appendix B: List of Symbols

A	specific surface area [m^2]
A_k	pre-exponential factor [cm, mol, s]
a_m	average surface area occupied by metal atom [$m^2\ g^{-1}$]
a_s(BET)	specific surface area [$m^2\ g^{-1}$]
c_i	concentration of species i [mol m^{-3}]
c_p	heat capacity of species i [J $(kg\ K)^{-1}$]
D	metal Dispersion [-]
E_a	activation energy [kJ mol^{-1}]
$F_{cat/geo}$	surface scaling factor (catalytic/geometric) [-]
f_k	coverage dependency function [-]
h_i	specific enthalpy of species i [J kg^{-1}]
h	specific enthalpy of mixture [J kg^{-1}]
I_i	signal intensity of species i [mA]
j_i	diffusive flux including surface flux of species i [kg $m^{-2}\ s^{-1}$]
k_{fk}	reaction rate constant [mol, m, s]
K_s	number of surface reactions [-]
m	mass of the sample for chemisorption measurements [g]
M_i	molar Mass of species i [kg mol^{-1}]
$\overline{M}$	average molar mass [kg]
n_{ads}	amount of adsorbed gas [mol]
n_i	number of molecules of species i [mol]
n_m	amount of adsorbed gas at one monolayer [mol]
N_A	Avogadro's constant $6.022 \cdot 10^{23}$ mol^{-1}
N_g	number of gas-phase species [-]
N_s	number of surface species [-]
p	pressure [Pa]
q	heat source term [W m^{-3}]
R	gas constant 8.314 J $(mol\ K)^{-1}$
r	radial coordinate in space [m]
r_p	radius of model pore [m]
S_i	selectivity of species i [-]
$\dot{s}_i$	reaction rate of species i [mol $m^2\ s^{-1}$]
T	temperature [K]
t	time [s]
t_{ads}	thickness of the multilayer [m]
U_i	conversion of species i [-]
u	axial velocity [m s^{-1}]
v	radial velocity [m s^{-1}]

V_m	molar volume of liquid nitrogen [$cm^3\ g^{-1}$]
ν_{mono}	chemisorbed volume [$cm^3\ g^{-1}$]
wt	metal loading [-]
X_i or $X(i)$	mole fraction of species i [-]
Y_i	mass fraction of species i [-]
Y_s	mass fraction [-]
z	axial spatial coordinate [m]
Γ	surface site density [mol cm^{-2}]
α	thermal diffusity [$m^2\ s^{-1}$]
β_k	temperature exponent [-]
ε_i	coverage dependent activation energy [kJ mol^{-1}]
Θ_i	surface coverage [-]
λ	thermal conductivity [W $(m\ K)^{-1}$]
λ_{ax}	axial thermal conductivity [W $(m\ K)^{-1}$]
λ_{rad}	radial thermal conductivity [W $(m\ K)^{-1}$]
μ	viscosity [kg $m^{-1}\ s^{-1}$]
ν_{ik}	stoichiometric coefficients [-]
ρ	mass density [kg m^{-3}]
σ	channel density [m^{-2}]
σ_i	number of occupied adsorption sites by species i [-]
φ	potential of hyperbolic field of QMS [V]
ω	frequency [s^{-1}]
$\dot{\omega}_i$	gas phase reaction source term [mol $m^3\ s^{-1}$]

Appendix C: Abbreviations

AC	Alternate current
BET	Brunauer-Emmett-Teller
CPO	Catalytic Partial Oxidation
cat.	catalytic
DC	Direct current
e.g.	example gratia
et al.	et alii
exp.	experimental
FID	flame ionisation detector
GC	Gas Chromatography
GHSV	gas hourly space velocity
h	hour
K	Kelvin
kJ	kilo Joule
kPa	kilo Pascal
KrF	Krypton flouride
m	metre
mA	milli Ampere
m/z	mass-to-charge ratio
MFC	mass-flow controller
min	minute
ml	millilitre
mm	millimetre
ms	milliseconds
µm	micrometer
MS	mass spectrometry
Pd	Palladium
PEM	Polymer Electrolyte Membrane / Proton Exchange Membrane
ppi	pores per inch
ppm	parts per million
Pt	Platinum
QMS	quadrupole mass spectrometry
Rh	Rhodium
rps	rounds per second
RT	room temperature
s	second
SEM	secondary electron multiplier, channeltron
SFG	sum-frequency generation

SKE	Steinkohleeinheit
slpm	standard litre per minute
SOFC	solid oxide fuel cell
TCD	thermal conductivity detector
tot.	total
V	Volt
VOC	volatile organic compounds
vol.-%	volume percentage
W	Watt
wt.-%	weight percentage
z.B.	zum Beispiel

References

[1] J. M. Thomas and W. J. Thomas, *Principles and Practice of Heterogeneous Catalysis*. Weinheim: VCH Verlagsgesellschaft mbH, **1997**.

[2] D. A. Hickman and L. D. Schmidt, "Steps in CH_4 Oxidation on Pt and Rh Surfaces: High-Temperature Reactor Simulations", *AIChE J.*, vol. *39*, **1993**, pp. 1164-1176.

[3] O. V. Buyevskaya, D. Wolf, and M. Baerns, "Rhodium - catalyzed partial oxidation of methane to CO and H_2.Transient studies on its mechanism", *Catal. Lett.*, vol. *29*, **1994**, pp. 249-260.

[4] K. Heitnes, S. Lindeberg, O. A. Rokstad, and A. Holmen, "Catalytic partial oxidation of methane to synthesis gas", *Catal. Today*, vol. *24* (3), **1995**, pp. 211-216.

[5] E. P. J. Mallens, J. H. B. Hoebink, and G. B. Marin, "The Reaction Mechanism of the Partial Oxidation of Methane to Synthesis Gas: A Transient Kinetic Study over Rhodium and a Comparison with Platinum", *Journal of Catalalysis*, vol. *167* (1), **1997**, pp. 43-56.

[6] O. Deutschmann, L. D. Schmidt, and J. Warnatz, "Modeling the Partial Oxidation of Methane in a Short Contact Time Reactor", *AIChE J.*, vol. *44* (11), **1998**, pp. 2465-2476.

[7] A. S. Bodke, S. S. Bharadwaj, and L. D. Schmidt, "The Effect of Ceramic Supports on Partial Oxidation of Hydrocarbons over Noble Metal Coated Monoliths", *Journal of Catalalysis*, vol. *179* (1), **1998**, pp. 138-149.

[8] G. Veser and J. Frauhammer, "Modelling steady state and ignition during catalytic methane oxidation in a monolith reactor", *Chem. Eng. Sci.*, vol. *55* (12), **2000**, pp. 2271-2286.

[9] M. Belgued, et al., "Low Temperature Catalytic Homologation of Methane on Platinum, Ruthenium and Cobolt", *Catal. Today*, vol. *13* (2-3), **1992**, pp. 337-445.

[10] V. R. Choudhary, A. M. Rajput, and V. H. Rane, "Low-Temperature Catalytic Selective Partial Oxidation of Methane to CO and H_2 over Ni/Yb_2O_3", *J. Phys. Chem.*, vol. *96* (22), **1992**, pp. 8686-8688.

[11] M. Baerns, "Oxidative Coupling of Methane for Utilization of Natural Gas", in *Chemical Reactor Technology for Environmental Safe Reactors and Products*, H. I. d. L. e. al., Ed.: Kluwer Academic Publishers, **1993**, pp. 283-316.

[12] M. Wolf, O. Deutschmann, F. Behrendt, and J. Warnatz, "Kinetic Model of an Oxygen-free Methane Conversion on a Platinum Catalyst", *Catal. Lett.*, vol. *61* (1-2), **1999**, pp. 15-25.

[13] L. Li, R. W. Borrya, and E. Iglesia, "Reaction-transport simulations of non oxidative methane conversion with continuos hydrogen removal - homogeneous-heterogeneous reaction pathways", *Chem. Eng. Sci.*, vol. *56* (5), **2001**, pp. 1869-1881.

[14] J. R. Rostrup-Nielsen, "Catalytic Steam Reforming", in *Catal. Sci. Technol.*, vol. *5*,

J. R. Anderson and M. Boudart, Eds. New York: Springer-Verlag, **1984**

[15] O. Deutschmann, R. Schwiedernoch, L. Maier, and D. Chatterjee, "Natural Gas Conversion in Monolithic Catalysts: Interaction of Chemical Reactions and Transport Phenomena", *Natural Gas Conversion VI, Studies in Surface Science and Catalysis*, vol. *136*, **2001**, pp. 215-258.

[16] G. P. v. d. Laan and A. A. C. M. Beenackers, "Kinetics and Selectivity of the Fischer-Tropsch Synthesis: a Literature Review", *Catal. Rev. - Sci. Eng.*, vol. *41* (3&4), **1999**, pp. 255-318.

[17] D. N. K. d. W. DNK, "Energie für Deutschland, Fakten, Perspektiven und Positionen im globalen Kontext", Essen **2004**.

[18] Wikipedia, "http://en.wikipedia.org/wiki/Hydrogen", last visit 30 Jan 2005.

[19] R. M. Ormerod, "Solid Oxide Fuel Cells", *Chem. Soc. Rev.*, vol. *32*, **2003**, pp. 17-28.

[20] D. Knight, *Humphry Davy: Science & Power*. Cambridge, MA: Blackwell Publishers, **1992**.

[21] G. B. Kauffman, "Johann Wolfgang Dobereiner's Feuerzeug on the sesquicentennial anniversary of his death." *Platinum Met. Rev.*, vol. *43* (3), **1999**, pp. 122-128.

[22] O. Deutschmann, "Interactions between transport and chemistry in catalytic reactors", Habilitationbsschrift: Ruprecht-Karls-Universität Heidelberg, **2001**, 171.

[23] O. Deutschmann and J. Warnatz, "Diagnostics for Catalytic Combustion", in *Applied Combustion Diagnostics*, vol. Chapter 20, K. Kohse-Hoeinghaus and J. B. Jeffries, Eds.: Taylor and Francis Publ., **2002**, pp. 518-533.

[24] R. A. D. Betta, "Catalytic combustion gas turbine systems: the preferred technology for low emissions electric power production and co-generation", *Catal. Today*, vol. *35* (1-2), **1997**, pp. 129-135.

[25] P. Forzatti and G. Groppi, "Catalytic combustion for the production of energy", *Catal. Today*, vol. *54* (1), **1999**, pp. 165.

[26] G. Groppi, C. Cristiani, and P. Forzatti, "Preparation and Characterization of Hexaaluminate Materials for High-temperature Catalytic Combustion", *Catalysis*, vol. *13*, **1997**, pp. 85-113.

[27] G. Saracco and V. Specchia, "Catalytic filters for the abatement of volatile organic compounds", *Chemical Engineering Science*, vol. *55*, **2000**, pp. 897-908.

[28] R. E. Hayes and S. T. Kolaczkowski, *Introduction to Catalytic Combustion*. Amsterdam: Gordon and Breach Science Publ., **1997**.

[29] L. D. Pfefferle and W. C. Pfefferle, "Catalysis in Combustion", *Catal. Rev. - Sci. Eng.*, vol. *29* (2-3), **1987**, pp. 219-267.

[30] U. Dogwiler, P. Benz, and J. Mantzaras, "Two-dimensional modelling for catalytically stabilized combustion of a lean methane-air mixture with elementary homogeneous and heterogeneous chemical reactions", *Combust. Flame*, vol. *116* (1), **1999**, pp. 243.

[31] J. Mantzaras, C. Appel, and P. Benz, "Catalytic Combustion of Methane/Air Mixtures over Platinum: Homogeneous Ignition Distances in Channel Flow

Configurations", Proc. Combust. Inst., Edingburg, vol. *28*, **2000**, pp. 1349-1358.

[32] O. Deutschmann, et al., "Hydrogen Assisted Catalytic Combustion of Methane on Platinum", *Catal. Today*, vol. *59*, **2000**, pp. 141-150.

[33] O. Deutschmann, R. Schmidt, F. Behrendt, and J. Warnatz, "Numerical Modeling of Catalytic Ignition", Proc. Combust. Inst., Pittsburgh, vol. *26*, **1996**, pp. 1747-1754.

[34] S. Tischer, C. Correa, and O. Deutschmann, "Transient three-dimensional simulation of a catalytic combustion monolith using detailed models for heterogeneous and homogeneous reactions and transport phenomena", *Catal. Today*, vol. *69* (1-4), **2001**, pp. 57-62.

[35] O. Deutschmann, et al., "DETCHEM: Computer package for detailed chemistry models in CFD codes", v. 1.4.2. Heidelberg, **2001**.

[36] O. Deutschmann, et al., "DETCHEM: Computer package for detailed chemistry models in CFD codes", v. 1.5.4: Heidelberg, **2003**.

[37] O. Deutschmann, et al., "DETCHEM: Computer package for detailed chemistry models in CFD codes", v. 2.0 beta: www.detchem.com, Karlsruhe, **2005**.

[38] O. Deutschmann, et al., "http://www.detchem.com/", last visit 27.05.2005.

[39] R. Schwiedernoch, et al., "Experimental and numerical investigation of the ignition of methane combustion in a platinum-coated honeycomb monolith", Proc. Combust. Inst., Saporo, Japan, vol. *29*, **2002**, pp. 1005-1011.

[40] K.-I. Fujimoto, F. H. Ribeiro, M. Avalos-Borja, and E. Iglesia, "Structure and Reactivity of PdO_x/ZrO_2 Catalysts for Methane Oxidation at Low Temperatures", *Journal of Catalysis*, vol. *179* (2), **1998**, pp. 431-442.

[41] R. Schwiedernoch, S. Tischer, C. Correa, and O. Deutschmann, "Experimental and numerical study on the transient behavior of partial oxidation of methane in a catalytic monolith", *Chem. Eng. Sci.*, vol. *58* (3-6), **2003**, pp. 633-642.

[42] R. Schwiedernoch, S. Tischer, H.-R. Volpp, and O. Deutschmann, "Towards a better understanding of transient processes in catalytic oxidation reactors", *Natural Gas Conversion VII, Studies in Surface Science and Catalysis*, vol. *147*, **2004**, pp. 511-516.

[43] R. J. Kee, M. E. Coltrin, and P. Glarborg, *Chemically Reacting Flow : Theory and Practice*. New York: John Wiley & Sons, **2003**.

[44] P. W. Atkins, *Physikalische Chemie*, 2 ed. Weinheim; New York: Wiley-VCH Verlagsgesellschaft mbH, **1996**.

[45] G. Ertl, H. Knözinger, and J. Weitkamp, "Handbook of Heterogeneous Catalysis", vol. *1*. Weinheim: VCH Verlagsgesellschaft mbH, **1997**

[46] J. Hagen, *Industrial Catalysis: A Practical Approach*. Weinheim: Wiley-VCH Verlag GmH, **1999**.

[47] M. Henzler and W. Göpel, *Oberflächenphysik des Festkörpers*, 2 ed. Stuttgart: B.G. Teubner Verlag, **1994**.

[48] M. Baerns, H. Hofmann, and A. Renken, *Chemische Reaktionstechnik*. Stuttgart, New York: Georg Thieme Verlag, **1992**.

[49] R. Kissel-Osterrieder, F. Behrendt, and J. Warnatz, "Dynamic Monte Carlo Simulations of Catalytic Surfac Reactions", Proc. Combust. Inst., Saporo, Japan, vol. *28*, **2002**, pp. 1323-1330.

[50] M. E. Coltrin, R. J. Kee, and F. M. Rupley, "Surface Chemkin: a general formalism and software for analyzing heterogeneous chemical kinetics at a gas-surface interface", *International Journal of Chemical Kinetics*, vol. *23* (12), **1991**, pp. 1111-1128.

[51] R. Schwiedernoch, "Untersuchung zur katalytischen Partialoxidation von Methan an mit Rhodium beladenen Monolithen", Diplomarbeit: Ruprecht-Karls-Universität Heidelberg, **2000**, 76.

[52] M. Oehme, *Praktische Einführung in die GC/MS-Analytik mit Quadrupolen*: Hüthig, **1996**.

[53] K. L. Busch, "Synergistic Developments in MS. A 50-Year Journey From "Art" to Science", *Spectroscopy*, vol. *15*, **2000**, pp. 30-39.

[54] J. H. Gross, *Mass Spectrometry*. Heidelberg: Springer-Verlag Berlin Heidelberg New York, **2004**.

[55] W. Paul, H. P. Reinhard, and O. Zahn, "The electric mass filter as mass spectrometer and isotope separator", *Zeitschrift für Physik*, vol. *152*, **1958**, pp. 143-182.

[56] V. Zumbach, "Nachweis von Gasphasenspezies in der Niederdruckdiamantsynthese durch Laserionisation und Molekularstrahlmassenspektroskopie", Dissertation: Universität Heidelberg, **1996**

[57] W. Paul, "Electromagnetic Traps for Charged and Neutral Particles", in *Nobel Prize Lectures in Physics 1981-1990*. Singapore: World Scientific Publishing, **1993**, pp. 601-622.

[58] M. Campanati, G. Fornasari, and A. Vaccari, "Fundamentals in the preparation of heterogeneous catalysts", *Catal. Today*, vol. *77* (4), **2003**, pp. 299-314.

[59] N. A. Savastenko, M. G. Schweitzer, H.-R. Volpp, and J. Wolfrum, "Abscheidung katalytisch aktiver Edelmetall-Nanopulver mittels gepulster UV-Laserablation", XXXVII. Jahrestreffen Deutscher Katalytiker, Weimar, **2004**.

[60] J. R. Anderson, "Structure of Metallic Catalysts", in. London: Academic Press, **1975**, pp. 295-352.

[61] J. Seifert and G. Emig, "Mikrostrukturuntersuchungen an porösen Feststoffen durch Physisorptionsmessungen." *Chem. Ing. Tech.*, vol. *58* (6), **1987**, pp. 457-484.

[62] G. Leofanti, M. Padovan, G. Tozzola, and B. Venturelli, "Surface area and pore texture of catalysts." *Catal. Today*, vol. *41* (1-3), **1998**, pp. 207-219.

[63] S. Brunauer, P. H. Emmett, and E. Teller, *Journal of American Chemical Society*, vol. *60*, **1938**, pp. 309.

[64] Porotec, *User-Manual: Advanced Data Processing for the SORPTOMATIC 1990*, **1995**.

[65] S. J. Gregg and K. S. W. Sing, *Adsorption, Surface Area and Porosity*, vol. *2nd*. London: Academic Press, **1982**.

[66] S. Tischer, "Simulation katalytischer Monolithreaktoren unter Verwendung detaillierter Modelle für Chemie und Transpor", PhD: Ruprecht-Karls-Universität, **2004**, 132.

[67] R. B. Bird, W. E. Stewart, and E. N. Lightfoot, *Transport Phenomena*, 2 edition (July 25, 2001) ed. New York: John Wiley & Sons, Inc., **2003**.

[68] J. Warnatz, U. Maas, and R. W. Dibble, *Combustion: Physical and Chemical Fundamentals, Modeling and Simulation, Experiments, Pollutant Formation*, 3d ed. Berlin: Springer, **2005**.

[69] L. L. Raja, et al., "A critical evaluation of Navier-Stokes, boundary-layer, and plug-flow models of the flow and chemistry in a catalytic-combustion monolith", *Catal. Today*, vol. *59* (1-2), **2000**, pp. 47-60.

[70] H. Schlichting and K. Gersten, *Boundary-Layer Theory*, 8th ed. Heidelberg: Springer-Verlag, **1999**.

[71] R. Jahn, D. Snita, M. Kubicek, and M. Marek, "3D-modeling of monolith reactors", *Catal. Today*, vol. *38* (1), **1997**, pp. 39-46.

[72] O. Deutschmann, et al., "DETCHEM", v. 1.4.2. Heidelberg, **2001**.

[73] P. Deuflhardt, E. Hairer, and J. Zugk, "One-step and extrapolation methods for differential-algebraic systems", *Numer. Math.*, vol. *51*, **1987**, pp. 501-516.

[74] A. C. Hindmarsh, "Scientific Computing", in. Amsterdam, **1983**, pp. 55-64.

[75] W. C. Pfefferle and L. D. Pfefferle, "Catalytically stabilized combustion", *Prog. Energy Combust. Sci.*, vol. *12* (1), **1986**, pp. 25-41.

[76] D. L. Baulch, et al., "Evaluated Kinetic Data for Combustion Modelling", *J. Phys. Chem. Ref. Data*, vol. *21* (3), **1992**, pp. 411-734.

[77] G. Veser and L. D. Schmidt, "Ignition and Extinction in the Catalytic Oxidaton of Hydrocarbons over Platinum", *AIChE J.*, vol. *42* (4), **1996**, pp. 1077-1087.

[78] O. Deutschmann, "Modellierung von Reaktionen an Oberflächen und deren Kopplung mit chemisch reagierenden Strömungen", Dissertation: Universität Heidelberg, **1996**, 133.

[79] P. Aghalayam, et al., "A C1 mechanism for methane oxidation on platinum", *Journal of Catalysis*, vol. *213* (1), **2003**, pp. 23-38.

[80] F. Behrendt, O. Deutschmann, R. Schmidt, and J. Warnatz, "Ignition and Extinction of Hydrogen-Air and Methane-Air Mixtures over Platinum and Palladium. Chapter 4", in *Heterogeneous Hydrocarbon Oxidation*: ACS Symposium Series, **1996**, pp. 48-57.

[81] T. A. Griffin and L. D. Pfefferle, "Gas Phase and Catalytic Ignition of Methane and Ethane in Air over Platinum", *American Institute of Chemical Engineering Journal*, vol. *36* (6), **1990**, pp. 861-870.

[82] P. Haupt and H. Möllencamp, "http://www.chemieexperimente.de/wasserstoff/6_1.htm", last visit 24.05.2005.

[83] R. Imbihl and G. Ertl, "Oscillatory Kinetics in Heterogeneous Catalysis", *Chemical Reviews*, vol. *95*, **1995**, pp. 697-733.

[84] R. J. Farrauto and C. H. Bartholomew, *Fundamentals of Industrial Catalytic Processes*. London: Blackie, **1997**.

[85] X. Zhang, C. S.-M. Lee, D. M. P. Mingos, and D. O. Hayward, "Oscillatory behaviour during the oxidation of methane over palladium metal catalysts", *Applied Catalysis A: General*, vol. *240* (1-2), **2003**, pp. 183-197.

[86] M. R. Lyubovsky and L. D. Pfefferle, "Complete methane oxidation over Pd catalyst supported on -alumina. Influence of temperature and oxygen pressure on the catalyst activity", *Catalysis Today*, vol. *47* (1-4), **1999**, pp. 29-44.

[87] J. Au-Yeung, A. T. Bell, and E. Iglesia, "The Dynamics of Oxygen Exchange with Zirconia-Supported PdO", *Journal of Catalysis*, vol. *185*, **1999**, pp. 213-218.

[88] D. Ciuparu, F. Bozon-Verduraz, and L. Pfefferle, "Oxygen Exchange between Palladium and Oxide Supports in Combustion Catalysts", *J. Phys. Chem. B*, vol. *106* (13), **2002**, pp. 3434-3442.

[89] C. A. Müller, M. Maciejewski, R. A. Koeppel, and A. Baiker, "Combustion of Methane over Palladium/Zirconia Derived from a Glassy Pd–Zr Alloy: Effect of Pd Particle Size on Catalytic Behavior", *Journal of Catalysis*, vol. *166* (1), **1997**, pp. 36-43.

[90] M. M. Wolf, H. Zhu, W. H. Green, and G. S. Jackson, "Kinetic model for polycrystalline Pd/PdO_x in oxidation/reduction cycles", *Applied Catalysis A: General*, vol. *244* (2), **2003**, pp. 323-340.

[91] K. Rajagopalan and D. Luss, "The influence of surface structure on the oscillations in the rate of hydrogen oxidation over palladium", *Chemical Engineering Science*, vol. *38* (3), **1983**, pp. 473-474.

[92] G. Groppi, et al., "Effect of ceria on palladium supported catalysts for high temperature combustion of CH_4 under lean conditions", *Catalysis Today*, vol. *50* (2), **1999**, pp. 399.

[93] S. C. Su, N. Carstens, and A. T. Bell, "A Study of the Dynamics of Pd Oxidation and PdO Reduction by H_2 and CH_4", *Journal of Catalysis*, vol. *176*, **1998**, pp. 125-135.

[94] M. M. Wolf, H. Zhu, W. H. Green, and G. S. Jackson, "Kinetic model for polycrystaline Pd/PdO_x in oxidation/reduction cycles", *Applied Catalysis A: General*, vol. *244*, **2003**, pp. 323-340.

[95] E. H. Voogt, A. J. M. Mens, O. L. J. Gijzeman, and J. W. Geus, "Adsorption of oxygen and surface oxide formation on Pd(111) and Pd foil studied with ellipsometry, LEED, AES and XPS", *Surf. Sci.*, vol. *373* (2-3), **1997**, pp. 210-220.

[96] I. Barin, *Thermochemical Data of Oure Substances*, vol. *I-II*, third ed. Weinheim: VCH Verlagsgesellschaft mbH, **1995**.

[97] D. R. Lide, *CRC Handbook of Chemistry and Physics*, 75th Ed. ed. Boca Raton: CRC Press, **1994**.

[98] J. G. McCarty, "Kinetics of PdO combustion catalysis", *Catalysis Today*, vol. *26* (3-4), **1995**, pp. 283-293.

[99] J. Au-Yeung, K. Chen, A. T. Bell, and E. Iglesia, "Isotopic Studies of Methane Oxidation Pathways on PdO Catalysts", *Journal of Catalysis*, vol. *188* (1), **1999**

[100] M. Huff and L. D. Schmidt, "Oxidative Dehydrogenation of Isobutane over Monoliths at Short Contact Times", *Journal of Catalalysis*, vol. *155* (1), **1995**, pp. 82-94.

[101] D. K. Zerkle, M. D. Allendorf, M. Wolf, and O. Deutschmann, "Understanding Homogeneous and Heterogeneous Contributions to the Platinum-Catalyzed Partial Oxidation of Ethane in a Short Contact Time Reactor", *Journal of Catalalysis*, vol. *196* (1), **2000**, pp. 18-39.

[102] C. R. H. d. Smet, et al., "An experimental reactor to study the intrinsic kinetics of catalytic partial oxidation of methane in the presence of heat-transport limitations", *App. Catal. A*, vol. *187* (1), **1999**, pp. 33-48.

[103] FLUENT, "4.4. New Hampshire: Fluent Inc. Lebanon, **1997**.

[104] S. Tummala, "Staged Catalysts for Millisecond Contact Time Reactors", Dissertation: University of Minnesota, **2000**, 121.

[105] K. S. Suslick, "Sonocatalysis", in *Handbook of Heterogeneous Catalysis*, vol. 3, G. Ertl, H. Knözinger, and J. Weitkamp, Eds. Weinheim: VCH Verlagsgesellschaft mbH, **1997**, pp. 1350-1357.

[106] T. Pery, et al., "Sum-Frequency Generation In Situ Study of CO Adsorption and Catalytic CO Oxidation on Rhodium at Elevated Pressures", Proc. Combust. Inst., Saporo, Japan, vol. *29*, **2002**.

[107] M. G. Schweitzer, "Laserspektroskopische Untersuchungen zur Adsorption und Reaktion von CO auf katalytisch aktiven Oberflächen", Dissertation: Ruprecht-Karls-Universität Heidelberg, **2003**, 197.

[108] J. H. Lee and D. L. Trimm, "Catalytic combustion of methane", *Fuel Proc. Technol.*, vol. *42* (2-3), **1995**, pp. 339-359.

[109] S. Wang and G. Q. M. Lu, "CO_2 reforming of methane on Ni catalysts: Effects of the support phase and preparation technique", *App. Catal. B*, vol. *16*, **1998**, pp. 269-277.

[110] D. Papadias, L. Edsberg, and P. H. Björnbom, "Simplified method of effectiveness factor calculations for irregular geometries of washcoats. A general case in a 3D concentration field", *Catal. Today*, vol. *60* (1-2), **2000**, pp. 11-20.

[111] J. Braun, et al., "Influence of Physical and Chemical Parameters on the Conversion Rate of a Catalytic Converter: A Numerical Simulation Study", *SAE Technical Paper*, vol., **2000**, pp. 2000-2001-0211.

[112] J. Braun, et al., "Three-Dimensional Simulation of the Transient Behavior of a Three-Way Catalytic Converter", *SAE Technical Paper*, vol. *2002-01-0065*, **2002**

[113] C. A. Mirkin, "The Beginning of a Small Revolution", *Small*, vol. *1* (1), **2005**, pp. 14-16.

[114] S. Walheim, E. Schäffer, J. Mlynek, and U. Steiner, "Nanophase-Separated Polymer Films as High-Performance Antirefection Coatings", *Science*, vol. *283*, **1999**, pp. 520-522.

[115] A. L. Efros and M. Rosen, "The Electronic Structure of Semiconductor Nanocrystals", *Annual Reviews of Materials Science*, vol. *30*, **2000**, pp. 475-521.

[116] W. J. Parak, et al., *Nanoparticles — From Theory to Application*. Weinheim: Wiley-VCH, **2003**.

[117] D. L. Klein, et al., "Asingle-electron transistor madefromacadmiumselenide nanocrystal", *Nature*, vol. *389*, **1997**, pp. 699-701.

[118] T. Pellegrino, et al., "On the Development of Colloidal Nanoparticles towards Multifunctional Structures and their Possible Use for Biological Applications", *Small*, vol. *1* (1), **2005**, pp. 48-61.

[119] S. Ravindran, et al., "Quantum dots as bio-labels for the localization of a small plant adhesion protein", *Nanotechnology*, vol. *16*, **2005**, pp. 1-4.

[120] G. B. Sergeev, "Nanochemistry of metals", *Russian Chemical Reviews*, vol. *70* (10), **2001**, pp. 809-825.

[121] I. Langmuir, *Trans. Faraday Soc.*, vol. *17*, **1922**, pp. 621.

[122] H. H. Rotermund, "Imaging of dynamic processes on surfaces by light", *Surface Science Reports*, vol. *29* (7-8), **1997**, pp. 267-364.

[123] H. H. Rotermund, W. Engel, M. Kordesch, and G. Ertl, "Imaging of spatio-temporal pattern evolution during carbon monoxide oxidation on platinum", *Nature (London)*, vol. *343*, **1990**, pp. 355-357.

[124] G. Ertl, "Oscillatory catalytic reactions at single-crystal surfaces", *Advances in Catalysis*, vol. *37*, **1990**, pp. 213-277.

[125] U. Metka, "Untersuchung von Teilschritten der heterogenen Reaktion von CO mit NO an Platin mittels Summenfrequenz-Spektroskopie", Dissertation: Ruprecht-Karls-Universität Heidelberg, **2000**, 155.

[126] H.-R. Volpp and J. Wolfrum, "Sum-Frequency Generation (SFG) Vibrational Spectroscopy as a Means for the Investigation of Catalytic Combustion", in *Applied Combustion Diagnostics*, vol. Chapter 12, K. Kohse-Hoeinghaus and J. B. Jeffries, Eds.: Taylor and Francis Publ., **2002**, pp. 336-358.

[127] N. N. Greenwood and A. Earnshaw, *Chemie der Elemente*, 1 ed. Weinheim: VCH Verlagsgesellschaft mbH, **1990**.

[128] S. M. Davis, F. Zaera, and G. A. Somorjai, "The Reactivity and Composition of Strongly Adsorbed Carbonaceous Deposits on Pt. Model of the Working Hydrocarbon Conversion Catalyst", *J. Catal.*, vol. *77*, **1982**, pp. 439-459.

[129] M. Wolf, "Simulation der katalytischen Methangaskonversion an Platin", Dissertation: Ruprecht-Karls-Universität Heidelberg, **2000**, 132.

[130] A. F. Holleman and E. Wiberg, *Lehrbuch der Anorganischen Chemie*, 33 ed. New York: Walter de Gruyter, **1985**.

[131] R. Quiceno, O. Deutschmann, and J. Warnatz, "Evaluation of a Deatiled Reaction Mechanism for Partial and Total Oxidation of Light C_4 Alkanes", European Combustion Meeting "ECM2005", Louvain-la-Neuve, Belgium, **April 3-6, 2005**.

Danksagung

An dieser Stelle möchte ich mich bei allen bedanken, die zum Gelingen dieser Arbeit beigetragen haben.

Mein besonderer Dank gilt:

Den Herren Professoren Olaf Deutschmann, Jürgen Warnatz und Jürgen Wolfrum, die mir die Durchführung dieser interessanten und vielseitigen wissenschaftlichen Aufgabe ermöglicht haben und für ihr unermüdliches Interesse an dieser Arbeit.

Ganz besonders möchte ich Herrn Priv. Doz. Dr. Hans-Robert Volpp für seine kompetente Betreuung danken, der mir nicht nur das Labor und Geräte zur Verfügung stellte, sondern auch zu jeder Zeit mit Hilfestellungen und Diskussionen bereit stand.

Allen Mitgliedern der Arbeitsgruppen von Dr. Volpp und Prof. Deutschmann danke ich für ihre Hilfsbereitschaft, die ständige Diskussionsbereitschaft und guter Arbeitsatmosphäre. Ganz besonders danke ich Herrn Dr. Uwe Metka Dr. Michael Schweitzer, Dipl. Chem Benjamin T. Schädel und Ms. Eng. Tran Thanh Nam, die mich bei meinen Experimenten unterstützten. Ebenso danke ich MS Eng. Vinod Janharandananm Dr. Lubow Maier und Dr. Steffen Tischer, die mir bei den zahllosen Fragen zur Simulation zur Verfügung standen. Herrn Dr. Schoch, Herrn Dr. Norinaga und Herrn Dr. Carstensen danke ich für zahllose Ideen und Diskussionen zur Katalyse.

Herrn Dr. Markus Wolf für die Bereitstellung eines von ihm entwickelten detaillierten Reaktionsmechanismusses für das oszillierende Verhalten von Pd/PdO.

Des Weiteren danke ich Jochen Schütz, Katrin Notar und Daniel Zimmermann, für ihre Unterstützung bei der praktischen Arbeit und Katalysatorpräparation.

Frau Ochs danke ich für die BET- und Chemisorptionsmessungen.

Ganz besonders möchte ich mich bei Frau Cariboni, Frau Helwig, Herrn Lichtenberg und Herrn Herberger für ihre Unterstützung in jeder Hinsicht bedanken.

Frau H. Buck danke ich für ihre Unterstützung bei allen sicherheitstechnischen Fragen und für ihre Art, das Mittagessen und Kaffeetrinken humorvoll zu gestalten.

Ich danke den Damen und Herren der Verwaltung und der verschiedenen Werkstätten. Besonders möchte ich mich bei Herrn Weis, Herrn Siegel und Herrn Ehrhardt bedanken, ohne deren Sachkenntnis und handwerkliches Geschick der Umbau und die Reparaturen der

Apparatur nicht gelungen wäre, und bei Frau Lemcke und Frau Huck für ihre unbürokratische Hilfsbereitschaft.

Der Firma CONDEA Sasol sei Dank für die Bereitstellung von Katalysatormaterial.

Allen Korrekturleserinnen und –lesern möchte ich für die kritische Durchsicht meiner Arbeit danken.

Ganz besonders möchte ich mich bei meiner Mutter undmeiner Stiefmutter bedanken für die Unterstützung meines Studiums und bei meinen Freunden, ohne die diese Arbeit nicht möglich gewesen wäre.

Erklärung:

Ich versichere hiermit, dass ich die vorliegende Dissertation selbst verfasst habe und mich keiner anderen als der von mir ausdrücklich bezeichneten Quellen und Hilfsmittel bedient habe.

Heidelberg, den 30.05.2005

(Renate Schwiedernoch)